

STRUCTURAL CHARACTERISTICS OF  $\text{LiCoO}_2$  PREPARED  
BY CO-PRECIPITATION



A Thesis Submitted in Partial Fulfillment of the Requirements for the

Degree of Doctor of Philosophy in Applied Physics

Suranaree University of Technology

Academic Year 2021

ลักษณะเฉพาะทางโครงสร้างของลิเทียมโคบอลต์ออกไซด์ที่เตรียมโดย  
วิธีตกตะกอนร่วม



วิทยานิพนธ์นี้เป็นส่วนหนึ่งของการศึกษาตามหลักสูตรปริญญาวิทยาศาสตรดุษฎีบัณฑิต  
สาขาวิชาฟิสิกส์ประยุกต์  
มหาวิทยาลัยเทคโนโลยีสุรนารี  
ปีการศึกษา 2564

STRUCTURAL CHARACTERISTICS OF  $\text{LiCoO}_2$  PREPARED  
BY CO-PRECIPITATION

Suranaree University of Technology has approved this thesis submitted in partial fulfillment of the requirements for the Degree of Doctor of Philosophy.

Thesis Examining Committee

Rattikorn Yimnirun

(Prof. Dr. Rattikorn Yimnirun)

Chairperson

Prayoon Songsiriritthigul

(Assoc. Prof. Dr. Prayoon Songsiriritthigul)

Member (Thesis Advisor)

Narong Chanlek

(Dr. Narong Chanlek)

Member (Thesis Co-Advisor)

Saroj Rujirawat

(Assoc. Prof. Dr. Saroj Rujirawat)

Member

Usa Sukkha

(Dr. Usa Sukkha)

Member

Chatchai Jothityangkoon

(Assoc. Prof. Dr. Chatchai Jothityangkoon)

Vice Rector for Academic Affairs

and Quality Assurance

Santi Maensiri

(Prof. Dr. Santi Maensiri)

Dean of Institute of Science

อวตล เขจรรักษ์ : ลักษณะเฉพาะทางโครงสร้างของลิเทียมโคบอลต์ออกไซด์ที่เตรียมโดย วิธี  
ตกตะกอนร่วม (STRUCTURAL CHARACTERISTICS OF  $\text{LiCoO}_2$  PREPARED BY CO-  
PRECIPITATION) อาจารย์ที่ปรึกษา : รองศาสตราจารย์ ดร.ประยูร ส่งสิริฤทธิกุล, 114 หน้า

คำสำคัญ : ลิเทียมโคบอลต์ออกไซด์/ วิธีตกตะกอนร่วม/ เทคนิคการดูดกลืนรังสีเอกซ์/ เทคนิค  
สเปกโทรสโกปีของอนุภาคอิเล็กทรอนิกส์ที่ถูกปลดปล่อยด้วยรังสีเอกซ์ / เทคนิครามานสเปกโทรสโกปี/  
เทคนิคการเลี้ยวเบนของรังสีเอกซ์

วิทยานิพนธ์ฉบับนี้ศึกษาผลของอุณหภูมิในการเผาหลังจากการเตรียมต่อลักษณะเฉพาะทาง  
โครงสร้างของ  $\text{LiCoO}_2$  ที่เตรียมโดยวิธีการตกตะกอนร่วมอย่างละเอียด โครงสร้างของ  $\text{LiCoO}_2$   
ที่เตรียมได้ถูกตรวจสอบอย่างเป็นระบบโดยใช้เทคนิคการเลี้ยวเบนของรังสีเอกซ์ โดยแสงซินโครตรอน  
(synchrotron X-ray diffraction) เทคนิคการดูดกลืนรังสีเอกซ์ (X-ray absorption spectroscopy)  
ซึ่งประกอบไปด้วย X-ray absorption near edge structure และ extended X-ray absorption  
fine structure และเทคนิครามานสเปกโทรสโกปี (Raman spectroscopy) สัณฐานวิทยาของ  
พื้นผิวและองค์ประกอบทางเคมีของ  $\text{LiCoO}_2$  ถูกวิเคราะห์ด้วยเทคนิคกล้องจุลทรรศน์อิเล็กตรอน  
แบบส่องกราด (field-emission electron microscopy) และเทคนิคสเปกโทรสโกปีของอนุภาค  
อิเล็กทรอนิกส์ที่ถูกปลดปล่อยด้วยรังสีเอกซ์ (X-ray photoelectron spectroscopy) ผลการศึกษา  
แสดงให้เห็นการเปลี่ยนแปลงเฟสของผลึกของ  $\text{LiCoO}_2$  กับอุณหภูมิที่ใช้ในการเผา การก่อตัว  
บางส่วนโครงสร้างผลึกแบบ HT- $\text{LiCoO}_2$  ในตัวอย่าง  $\text{LiCoO}_2$  ถูกพบที่อุณหภูมิ 300 องศา  
เซลเซียส และก่อตัวสมบูรณ์ที่อุณหภูมิต่ำที่สุดที่ 600 องศาเซลเซียส นอกจากนี้พบว่าบรรยากาศที่ใช้  
ในการเผาส่งผลต่อการจัดเรียงตัวของแนวแกน c (c-axis orientation) ในโครงสร้าง โดย  $\text{LiCoO}_2$   
ที่เผาภายใต้การไหลของก๊าซไนโตรเจนให้ความเป็นระเบียบแนวแกน c ในโครงสร้างที่สูงกว่าการเผา  
ภายใต้การไหลของแก๊สผสมระหว่างออกซิเจนและก๊าซไนโตรเจน

สาขาวิชาฟิสิกส์  
ปีการศึกษา 2564

ลายมือชื่อนักศึกษา อวตล เขจรรักษ์  
ลายมือชื่ออาจารย์ที่ปรึกษา ประยูร ส่งสิริฤทธิกุล  
ลายมือชื่ออาจารย์ที่ปรึกษาร่วม Worany Qualek

AWADOL KHEJONRAK : STRUCTURAL CHARACTERISTICS OF  $\text{LiCoO}_2$  PREPARED BY CO-PRECIPITATION. THESIS ADVISOR : ASSOC. PROF. PRAYOON SONGSIRIRITTHIGUL, Ph.D. 114 PP.

Keyword:  $\text{LiCoO}_2$  / Co-precipitation method / XAS / XPS / Raman spectroscopy / XRD

This thesis thoroughly studied on the effect of post annealing temperature on the structural characteristics of  $\text{LiCoO}_2$  powder prepared by co-precipitation method. The structure of the prepared  $\text{LiCoO}_2$  powder was systematically investigated by the synchrotron X-ray diffraction, X-ray absorption spectroscopy technique, including X-ray absorption near edge structure and extended X-ray absorption fine structure, and dispersive Raman spectroscopy techniques. The surface morphologies and chemical compositions of the prepared  $\text{LiCoO}_2$  powders were also characterized by field emission scanning electron microscopy (FE-SEM) and X-ray photoelectron spectroscopy techniques. The results demonstrated the phase evolution of  $\text{LiCoO}_2$  powders with the annealing temperature. The formation of HT- $\text{LiCoO}_2$  structure was partly observed at 300 °C and it was complete at the minimum annealing temperature of 600 °C. The annealing ambient also influenced the degree of c-axis orientation structure. The annealing under the flow of  $\text{N}_2$  yielded a higher degree of the c-axis orientation than that of mixture of  $\text{N}_2$  and  $\text{O}_2$ .

School of Physics

Academic Year 2021

Student's signature อภินันท์ วัฒนวิจิตร

Advisor's signature ประยูร อ.

Co-advisor's signature นารายณ์ ชวนเลิศ

## ACKNOWLEDGEMENT

The following are people, to whom I would like to express my sincere words of kindly acknowledge for thesis.

Firstly, Prof. Dr. Rattikorn Yimnirun, my supervisor, is deserving of my sincere gratitude for his invaluable support. He consistently gave me excellent advice at every stage of my Ph.D. student's life, inspiring and providing me with understanding patience, fresh ideas, and strong motivation. He not only provided academic knowledge, but he also shared his life experience, which facilitated my optimization. Secondly, Assoc. Prof. Dr. Saroj Rujirawat, my co-advisor, is also deserving my thanks. Whenever I encountered any issue, he often gave a solution. He also introduced me to the synchrotron techniques, which are very beneficial to my research. Thirdly, I would like to thank Assoc. Prof. Dr. Prayoon Songsiriritthigul, my Ph.D. program adviser who provided me the procedure for working on my subject and taught me how to succeed in the philosophy program. I also would like to thank Dr. Narong Chanlek, my co-advisor. He consistently gave me the opportunities for new collaborations, which resulted in outstanding contributions. Whenever I was perplexed, he directed a solid one-detection strategy for resolving the issue. I would like to thank Dr. Usa Sukkha for teaching me how to prepare the  $\text{LiCoO}_2$  by the co-precipitation method. She guided me in the right direction whenever I was feeling confused and helped me consider a solution to the situation. In addition to that, she assisted me with the revising of the manuscript.

I would like to thank the whole faculty at the school of Physics for giving me the lectures, document processes, and idea via seminars. In addition, I would like to thank all the students at the institute of science for their constant friendship. In conclusion, I would want to thank my parents, who have always been in the background for every step.

Awadol Khejonrak

# CONTENTS

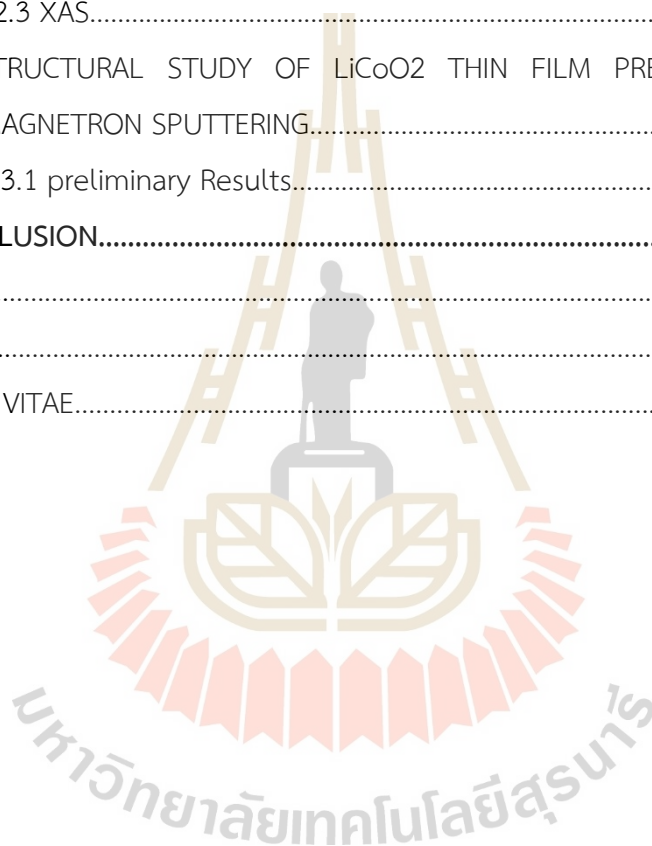
|   | Page     |
|---|----------|
| ABSTRACT IN THAI.....   | I        |
| ABSTRACT IN ENGLISH.....                                      | II       |
| ACKNOWLEDGEMENT.....  | III      |
| CONTENTS.....   | IV       |
| LIST OF TABLES.....   | VII      |
| LIST OF FIGURES.....  | IX       |
| <b>CHAPTER</b>  |          |
| <b>I INTRODUCTION.....</b>                                    | <b>1</b> |
| 1.1 BACKGROUND AND MOTIVATION .....                           | 1        |
| 1.2 THESIS OBJECTIVES.....                                    | 6        |
| 1.3 SCOPE OF THESIS.....                                      | 6        |
| 1.4 OUTLINE OF THESIS.....                                    | 6        |
| <b>II LITERATURE REVIEW AND CHARACTERIZATION.....</b>         | <b>7</b> |
| 2.1 LITHIUM-ION BATTERIES.....                                | 7        |
| 2.1.1 Cathode materials.....                                  | 9        |
| 2.1.2 Electrolyte.....  | 10       |
| 2.2 STRUCTURE OF $\text{LiCoO}_2$ .....                       | 13       |
| 2.3 PREPARATION METHODS FOR $\text{LiCoO}_2$ POWDER.....      | 19       |
| 2.3.1 Solid-state synthesis.....                              | 19       |
| 2.3.2 Sol-Gel Method.....                                     | 19       |
| 2.3.3 Coprecipitation Method.....                             | 20       |
| 2.3.4 Hydrothermal Method.....                                | 20       |
| 2.4 THIN FILM SOLID STATE LITHIUM BATTERIES.....              | 21       |
| 2.4.1 Preparation methods for $\text{LiCoO}_2$ thin film..... | 22       |

## CONTENTS (Continued)

|            |   | Page      |
|------------|---|-----------|
|            | 2.5 ADVANCED CHARACTERIZATION TECHNIQUES.....   | 27        |
|            | 2.5.1 X-ray absorption spectroscopy (XAS).....  | 27        |
|            | 2.5.2 X-ray Absorption Near Edge Structure (XANES).....   | 31        |
|            | 2.5.3 Extended X-ray Absorption Fine Structure (EXAFS).....   | 33        |
|            | 2.5.4 X-ray diffraction (XRD).....  | 36        |
|            | 2.5.5 X-ray photoelectron spectroscopy.....   | 39        |
|            | 2.5.6 Raman Spectroscopy.....   | 42        |
| <b>III</b> | <b>RESEARCH PROCEDURE.....</b>  | <b>44</b> |
|            | 3.1 PREPARATION OF LiCoO <sub>2</sub> POWDER .....  | 44        |
|            | 3.1.1 Effect of thermal annealing temperature.....  | 44        |
|            | 3.1.2 Phosphate glass synthesis.....  | 45        |
|            | 3.2 PREPARATION OF LiCoO <sub>2</sub> THIN FILMS.....   | 45        |
|            | 3.3 Measurements.....   | 46        |
|            | 3.3.1 Syn-XRD.....  | 46        |
|            | 3.3.2 XRD.....  | 47        |
|            | 3.3.3 XPS.....  | 47        |
|            | 3.3.4 XAS.....  | 48        |
|            | 3.3.5 Raman spectroscopy.....   | 49        |
|            | 3.3.6 SEM.....  | 49        |
| <b>IV</b>  | <b>RESULT AND DISCUSSION.....</b>   | <b>50</b> |
|            | 4.1 EFFECT OF THERMAL ANNEALING ON THE STRUCTURE OF LiCoO <sub>2</sub><br>POWDERS PREPARED BY CO-PRECIPIATION METHOD..... | 50        |
|            | 4.1.1 XRD.....  | 50        |
|            | 4.1.2 XAS.....  | 53        |
|            | 4.1.3 Raman.....  | 57        |
|            | 4.1.4 XPS.....  | 59        |
|            | 4.1.5 SEM.....  | 65        |

## CONTENTS (Continued)

|  | Page      |
|--|-----------|
| 4.2 INFLUENCE OF ANNEALING AMBIENT ON THE STRUCTURE OF $\text{LiCoO}_2$ ....                   | 67        |
| 4.2.1 XRD.....   | 67        |
| 4.2.2 SEM.....   | 70        |
| 4.2.3 XAS.....   | 71        |
| 4.3 STRUCTURAL STUDY OF $\text{LiCoO}_2$ THIN FILM PREPARED BY RF<br>MAGNETRON SPUTTERING..... | 74        |
| 4.3.1 preliminary Results.....   | 74        |
| <b>V CONCLUSION.....</b>   | <b>78</b> |
| REFERENCES.....  | 79        |
| APPENDIX.....  | 90        |
| CURRICULUM VITAE.....  | 100       |

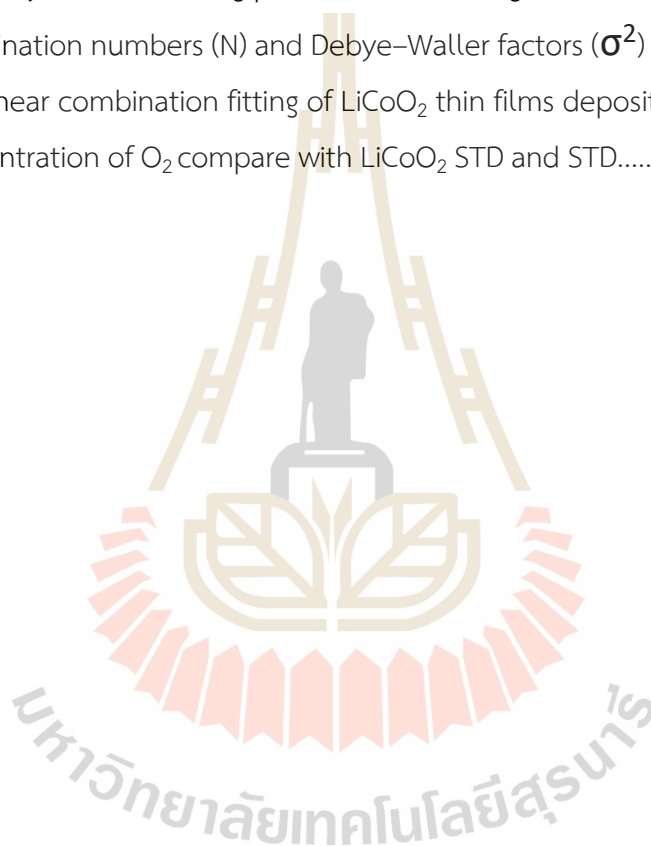


## LIST OF TABLES

| Table |   | Page |
|-------|---|------|
| 1.1   | Comparison of LIB technologies with other battery technologies (Masaki Yoshio et al., 2009) .....   | 2    |
| 1.2   | Comparison of the performances of LIBs with different types of cathode materials (I. Buchmann, 2019) .....  | 3    |
| 2.1   | Preparation methods, synthesis temperature and time, phase composition, and morphological properties of LT-LiCoO <sub>2</sub> .....   | 16   |
| 2.2   | Preparation methods and synthesis temperature and time, phase composition and morphological characteristics of HT-LiCoO <sub>2</sub> , ordered with decreasing synthesis temperature..... | 17   |
| 2.3   | Experimental conditions for the preparation of LiCoO <sub>2</sub> thin films deposited by the rf-sputtering technique (Christian M. Julien et al., 2019) .....                            | 26   |
| 4.1   | The lattice parameters of the LiCoO <sub>2</sub> powders annealed at different temperatures.....  | 53   |
| 4.2   | Summary of EXAFS fitting parameters including interatomic distances (R), coordination numbers (N) and Debye–Waller factors ( $\sigma^2$ ) .....   | 56   |
| 4.3   | The relative atomic concentrations of different elements in LiCoO <sub>2</sub> samples.....   | 61   |
| 4.4   | Summary of chemical compositions and oxidation states of Co from the LiCoO <sub>2</sub> powders annealed at different temperatures as estimated by XPS.....                               | 63   |
| 4.5   | Li/Co ratio of the LiCoO <sub>2</sub> powders annealed at different temperatures before washing and after washing with deionized water.....   | 64   |
| 4.6   | The intensity ratios of the (003) peak to the (104) peak (I003/I104) .....  | 67   |

## LIST OF TABLES (Continued)

| Table |   | Page |
|-------|---|------|
| 4.7   | The crystallite sizes of the LiCoO <sub>2</sub> powders annealed at different temperatures for 10 h under the flow of O <sub>2</sub> (20 sccm) and N <sub>2</sub> (80 sccm) mixture and N <sub>2</sub> (100 sccm) ..... | 69   |
| 4.8   | Summary of EXAFS fitting parameters including interatomic distances (R), coordination numbers (N) and Debye–Waller factors ( $\sigma^2$ ) .....   | 73   |
| 4.9   | The linear combination fitting of LiCoO <sub>2</sub> thin films deposited with various concentration of O <sub>2</sub> compare with LiCoO <sub>2</sub> STD and STD.....   | 76   |



## LIST OF FIGURES

| Figure   | Page |
|--|------|
| 2.1 A schematic diagram of a typical LIB (Liu et al., 2011) .....  | 8    |
| 2.2 (a) Layered crystalline structure of the rhombohedral $\text{LiCoO}_2$ ; (b) representation of the octahedral $\text{CoO}_6$ structure; (c) stacking arrangement of the layers (ABCABC) (Bruno G. A. Freitas et al., 2017) ..... | 14   |
| 2.3 Cationic positions and unit cell constants indicated for the hexagonal, spinel and rocksalt lattice structure (M. Antaya et al., 1994) .....   | 18   |
| 2.4 A schematic representation of a planar all-solid-state microbattery.....   | 22   |
| 2.5 Schematic diagram illustrating the basic components of a magnetron sputtering system.....  | 24   |
| 2.6 Schematic diagram showing the preferred textures for sputtered $\text{LiCoO}_2$ films.....   | 25   |
| 2.7 Schematic of incident and transmitted X-ray beam.....  | 27   |
| 2.8 Diagram of the electron transition in inner shells (Thompson et al., 2001)...  | 28   |
| 2.9 Mechanism of the x-ray absorption (a) X-ray absorption (b) Fluorescent X-ray emission and (c) Auger emission (Klysubun, 2006) .....  | 29   |
| 2.10 Theoretical and algorithm for XANES and EXAFS spectra (Larsen et al., 2014) .....   | 30   |
| 2.11 The muffin-tin potential consist of non-overlapping spherical regions (Kodre, 2002) .....   | 32   |
| 2.12 Interference of outgoing and backscattered photoelectron wave.....  | 33   |
| 2.13 A schematic of XRD pattern and information obtainable ( <a href="https://nptel.ac.in/courses/115103030/3">https://nptel.ac.in/courses/115103030/3</a> ) .....   | 37   |
| 2.14 A schematic diagram of typical XPS experiment.....  | 40   |
| 2.15 XPS spectrum of lead showing the schematic of an electronic structure of $\text{LiCoO}_2$ .....   | 41   |
| 2.16 Basics principle of state diagram of scattering pattern.....  | 43   |

## LIST OF FIGURES (Continued)

| Figure  | Page |
|---|------|
| 3.1 View of the entire sputter system (on the left) and rack control (on the right).....  | 45   |
| 3.2 A photograph of powder X-ray diffraction (PXRD) end-station of BL1.1W, SLRI.....  | 47   |
| 3.3 A photograph of XPS of BL5.3, SLRI.....   | 48   |
| 4.1 Syn-XRD patterns of the prepared $\text{LiCoO}_2$ powders annealed at different temperatures for 10 h.....  | 51   |
| 4.2 XANES spectra of Co K-edge of the $\text{LiCoO}_2$ samples annealed at different temperatures for 10 h.....   | 54   |
| 4.3 Fourier transform EXAFS spectra at the Co K-edge and k-space(insets) of the $\text{LiCoO}_2$ powders annealed at different temperatures for 10 h.....   | 55   |
| 4.4 Raman spectra of $\text{LiCoO}_2$ powders annealed at different temperatures (a) before washing and (b) after washing with deionized water.....   | 58   |
| 4.5 Wide scan XPS spectra of the $\text{LiCoO}_2$ annealed at different temperatures (a) before washing (b) after washing with DI water.....  | 60   |
| 4.6 High resolution XPS spectra of Co 2p of the $\text{LiCoO}_2$ annealed at different temperatures for 10 h.....   | 62   |
| 4.7 XPS spectra Li 1s of $\text{LiCoO}_2$ samples at different temperatures (a) before washing and (b) after washing with deionized water.....  | 65   |
| 4.8 FE-SEM images of the $\text{LiCoO}_2$ powders annealed at different temperatures for 10h.....   | 66   |
| 4.9 XRD patterns of the prepared $\text{LiCoO}_2$ powders annealed at different temperatures for 10h a) under the flow mixture of $\text{O}_2$ and $\text{N}_2$ (20 and 80 sccm, respectively) and b) $\text{N}_2$ (100 sccm) ..... | 68   |
| 4.10 FE-SEM images of the $\text{LiCoO}_2$ powders annealed at different temperatures for 10 h under the flow mixture of $\text{O}_2$ and $\text{N}_2$ (20 and 80 sccm, respectively) and $\text{N}_2$ (100 sccm) .....             | 70   |

## LIST OF FIGURES (Continued)

| Figure   | Page |
|--|------|
| 4.11 XANES of Co K-edge of the LiCoO <sub>2</sub> powders annealed under the flow mixture of O <sub>2</sub> 20 sccm and N <sub>2</sub> 80 sccm (l-LCO) and N <sub>2</sub> 100 sccm (h-LCO) at 600 °C and 700 °C.....           | 71   |
| 4.12 Fourier transform EXAFS spectra of Co K-edge of the LiCoO <sub>2</sub> powders annealed under the flow mixture of O <sub>2</sub> 20 sccm and N <sub>2</sub> 80 sccm and N <sub>2</sub> 100 sccm at 600 °C and 700 °C..... | 72   |
| 4.13 XRD patterns of the LiCoO <sub>2</sub> films deposited with different time.....   | 74   |
| 4.14 XRD patterns of the LiCoO <sub>2</sub> thin films deposited with different O <sub>2</sub> flow rate.....  | 75   |
| 4.15 XANES and Fourier transform EXAFS spectra of Co K-edge of the LiCoO <sub>2</sub> thin film was sputtered with 20 sccm of pure Ar and 1 to 7 sccm of different O <sub>2</sub> forms in an Ar/O <sub>2</sub> mixture.....   | 77   |

# CHAPTER I

## INTRODUCTION

### 1.1 BACKGROUND AND MOTIVATION

Energy storage devices have received much attention in recent years due to their great potential in a variety of applications, including the integration of renewable energy sources, electric vehicles (EVs), portable electronics, microgrids, and backup power systems. Batteries are one of the energy storage options that offer a number of advantages, such as portability, efficiency, high energy density, quick response time, scalability, environmental friendliness, long lifespan and safety improvements. Many different battery technologies have been developed, such as lead-acid and nickel-cadmium. Among these technologies, lithium-ion batteries (LIBs) are the battery technology of choice and currently the leaders in the market due to their high energy density, lightweight, low maintenance, long service life, and high efficiency. Many portable electronics, such as digital cameras, mobile phones, and laptops, are now powered by rechargeable LIBs, which are developing quickly. In addition, it is the most promising candidate for next-generation energy storage devices for hybrid or electrical vehicles (HEVs and EVs), which are expected to replace certain conventional cars and aid in reducing air pollution and preventing climate change. (M. Balkanski, 2000 and N. Terada et al., 2001) The comparison of LIB technologies with other battery technologies is shown in Table 1.1.

The LIBs are an electrochemical cell which consists of two electrodes, anode, and cathode. These electrodes have distinct chemical potentials that are separated by a solid separator and are filled with an ionic conductive electrolyte (C. Daniel et al., 2015). The anode is typically made of graphite, while the cathode is lithium-based layered metal oxides ( $\text{LiMO}_2$ , where M is a transition metal ion such as Co, Mn, or Ni). The battery performance is strongly dependent on the cathode materials. The performances of the LIBs with different types of cathode materials are listed in Table 1.2. Among the cathode materials,  $\text{LiCoO}_2$  exhibits many distinctive advantages,

including high  $\text{Li}^+$ /electron conductivity, high compacted density ( $4.2 \text{ g cm}^{-3}$ ), and excellent cycle life and reliability [Adv. Energy Mater. 2020, 2000982]. This cathode material was first introduced as a lithium-ion intercalation material by Prof. John B. Goodenough in 1980 and was firstly commercialized by Sony in 1991 (Y. Nishi, 2001).

**Table 1.1** Comparison of LIB technologies with other battery technologies (Masaki Yoshio et al, 2009).

|  | Lithium ion | Nickel Metal<br>Hydride | Nickel<br>Cadmium | Lead acid |
|--|-------------|-------------------------|-------------------|-----------|
| Working Voltage (v)                          | 3.7         | 1.2                     | 1.2               | 2         |
| Gravimetric Energy Density (Wh/Kg)           | 130~200     | 60~90                   | 40~60             | 30~40     |
| Volumetric Energy Density (Wh/L)             | 340~400     | 200~250                 | 160~200           | 130~180   |
| Volumetric Energy Density (Wh/L)             | 500         | 400                     | 400               | 300       |
| Self-discharge rate (% per month)            | 5           | 35                      | 30                | 10        |
| Energy Efficiency (discharge /charge)        | 99%         | 70%                     | 70%               | 75%       |
| Weight of the material for the same capacity | 1           | 2                       | 2.5               | 4         |
| Memory Effect                                | None        | 40%                     | None              | None      |
| Reliability                                  | High        | Low                     | Average           | High      |

**Table 1.2** Comparison of the performances of LIBs with different types of cathode materials (I. Buchmann, 2019).

| Type of cathode                  | LiCoO <sub>2</sub>                       | (Li(Ni,Mn,Co)O <sub>2</sub> )             | LiMn <sub>2</sub> O <sub>4</sub>                   | LiFePO <sub>4</sub>  |
|----------------------------------|--|---|--|--|
| Operating voltage range(V)       | 2.5-4.2                                  | 2.5-4.2                                   | 2.5-4.2  | 2.0-3.6  |
| Nominal cell voltage(V)          | 3.6-3.7                                  | 3.6-3.7                                   | 3.7-3.8  | 3.3  |
| Energy density by Weight (Wh/kg) | 175-240                                  | 100-240                                   | 100-150  | 60-110   |
| Energy density by volume(Wh/L)   | 400-640                                  | 250-640                                   | 250-350  | 125-250  |
| Continuous discharge rate(C2)    | 2-3                                      | 2-3                                       | >30  | 10-125   |
| Cycle life                       | 500+                                     | 500+                                      | 500+   | 1000+  |
| Temperature range of charge      | 0-45                                     | 0-45                                      | 0-45   | 0-45   |
| Temperature range of discharge   | -20-60                                   | -20-60                                    | -30-60   | -30-60   |
| Applications                     | Mobile phones, tablets, laptops, cameras | E-bikes, medical devices, EVs, industrial | Power tools, medical devices, electric powertrains | Portable and stationary needing high load currents and endurance |

LiCoO<sub>2</sub> structure consists of layers of lithium (Li<sup>+</sup>) that are stacked between the slabs of octahedral formed by cobalt (Co<sup>3+</sup>) and oxygen (O<sup>2-</sup>) atoms. It has two crystallographic structures, depending on the synthesis temperature. A cubic spinel structure is obtained at low temperatures (LT-LiCoO<sub>2</sub>), which transforms to a hexagonal-NaFeO<sub>2</sub> structure at high temperatures (HT-LiCoO<sub>2</sub>). The crystal structure of LiCoO<sub>2</sub> strongly influences the performances of the LIBs. The HT-LiCoO<sub>2</sub> has been reported to have better electrochemical performances compared to the LT-LiCoO<sub>2</sub> (Wang et al., 2015). In order to obtain the desirable structure with high electrochemical performances, many synthesis methods of LiCoO<sub>2</sub> have been studied and developed, such as sol-gel, co-precipitation, hydrothermal emulsion, sonochemical and combustion (Minki Jo et al., 2009). Many aspects of this technology are still being researched, such as reducing costs, extending cycling life, and reduce the temperature of the synthesis process. (M. S. Whittingham, 2008) A conventional solid-state reaction method can be used to synthesize HT-LiCoO<sub>2</sub> with calcination temperature as high as 850–900 °C for several hours. This technique is highly potential for mass production, but, it is difficult to control the impurities and morphology/particle size of the LiCoO<sub>2</sub> powder (Antolini, 2004, Gim et al., 2020). The HT-LiCoO<sub>2</sub> formation can be also prepared at the lower annealing temperatures when the different synthesis methods, especially wet techniques, are proceeded. Co-precipitation technique is another attractive technique for LiCoO<sub>2</sub> synthesis. This wet chemical technique has been, generally, used to prepare nano powder of ceramics under ambient atmosphere and temperature (Chang et al., 2010; Dong and Koenig, 2020; Kim et al., 1999; Lala et al., 2003). It is simple, cost-effective, rapid, scalable and particle morphology controllable. However, the synthesized powder by this method yet needs to be calcined at high temperature after the preparation for the amorphous to crystalline structures transformation. Kim et al. synthesized the LiCoO<sub>2</sub> by the co-precipitation method based on acetate solutions, lithium hydroxide and lithium peroxide solutions. The HT-LiCoO<sub>2</sub> was observed after annealing at 900 °C for 3 days, yielding the highest capacity of, approximately, 150 mAh/g in the range between 4.3–3.3 V (Kim et al., 1999). Chen et al. prepared the LiCoO<sub>2</sub> nanoparticles by the co-precipitation method in ethanol solution with lithium and cobalt salts. It was reported that the annealed sample at

600°C for 10 h showed the HT-LiCoO<sub>2</sub> structure with the best electrochemical properties (Chen et al., 2002).

This thesis performed a fundamental study on structural characteristics of LiCoO<sub>2</sub> powder which was prepared by co-precipitation method. Since, there were scant reports of the investigations with this preparation method. The LiCoO<sub>2</sub> properties prepared via co-precipitation method were systematically studied by using Synchrotron-based X-ray techniques. The effect of thermal annealing on the structure of the LiCoO<sub>2</sub> was also investigated by the synchrotron X-ray diffraction (Syn-XRD), X-ray absorption spectroscopy (XAS) and Dispersive Raman spectroscopy (Raman) techniques. Syn-XRD with intense X-ray beam can provide a greater signal to noise ratio than the conventional X-ray diffraction (XRD) and it can avoid background fluorescence by wavelength adjustment. Therefore, the structural investigation by using Syn-XRD should reveal more precise and accurate information of LiCoO<sub>2</sub> structures leading to better understanding. It should be noted that besides its advantages, Syn-XRD technique still produces average structural information from the crystalline phases with only long-range order. In addition, the investigations by the Synchrotron X-ray techniques in this study included the X-ray absorption near-edge structure (XANES) and the extended X-ray absorption fine structure (EXAFS). While XANES reflected the oxidation state, electronic configuration and site symmetry of the absorbing atom, the EXAFS gave structural quantitative information of short-range-order parameters such as species and numbers of neighboring atoms, the interatomic distances and Debye-Waller factor (Lin et al., 2017). The surface morphologies and chemical compositions of the LiCoO<sub>2</sub> powders were also characterized by field-emission scanning electron microscope (FE-SEM) and X-ray photoelectron spectroscopy (XPS) techniques.

In addition to the LiCoO<sub>2</sub> powder prepared by co-precipitation method, this thesis also performed the preliminary study on the preparation and structural study of LiCoO<sub>2</sub> thin films fabricated by radio-frequency (RF) magnetron sputtering technique. The LiCoO<sub>2</sub> thin films have become more attractive for use as cathode material for thin film solid state lithium batteries. These batteries have advantages of low volume, high energy density and good integration with micro-devices and micro-systems, such

as micro-sensors, smart cards, and micro-electromechanical system (MEMS) (Y. Wang et al., 2015). Similar to typical LIBs, the electrochemical performances of the thin film solid state lithium batteries are particularly sensitive to the  $\text{LiCoO}_2$  structure, which in turn dependent on the fabrication conditions.

## 1.2 THESIS OBJECTIVES

The objectives of this thesis are listed below.

1. To study the preparation of  $\text{LiCoO}_2$  powder via a coprecipitation method.
2. To study the structure of  $\text{LiCoO}_2$  powders prepared by coprecipitation method and the effect of annealing temperature on their structure by using synchrotron radiation techniques, such as, XAS and Syn-XRD.
3. To study the preparation and structure of  $\text{LiCoO}_2$  thin film via an RF magnetron sputtering technique.

## 1.3 SCOPE OF THESIS

1. The  $\text{LiCoO}_2$  powder is prepared by co-precipitation method.
2. The structure of the prepared  $\text{LiCoO}_2$  powders is investigated by XAS and Syn-XRD technique.
3. The  $\text{LiCoO}_2$  thin films are prepared by RF magnetron sputtering technique.

## 1.4 OUTLINE OF THESIS

This thesis is divided into 5 chapters. Chapter 1 provides an introduction, background information and motivation of the thesis. Chapter 2 gives a brief review of lithium-ion batteries, and the properties, structure, and preparation of  $\text{LiCoO}_2$  powder. Relevant research and literatures are also provided in this chapter. Chapter 3 gives the details on experimental methodology and experiments. It includes the preparation processes and characterization techniques used in this thesis. Chapter 4 presents the obtained results and discussion. Chapter 5 summarizes and concludes the study in this thesis. The recommendation for future work is also outlined.

## CHAPTER II

### LITERATURE REVIEW AND CHARACTERIZATION

This chapter provides a brief overview of the LIBs, physical properties, and structure of  $\text{LiCoO}_2$ . It also reviews the previous works on the structural study and preparation processes of  $\text{LiCoO}_2$ . The principle of advanced characterization techniques used in this thesis are also briefly described.

#### 2.1 LITHIUM-ION BATTERIES

An LIB is a type of rechargeable battery commonly used in portable electronic devices, electric vehicles, and renewable energy systems. It demonstrates many merits, such as high energy density, long cycle life, and low self-discharge rate. The LIBs typically consist of two electrodes which have different chemical potentials as shown in Figure 2.1. The electrodes are separated by a solid separator and filled with an ionic conductive electrolyte. (C. Daniel et al., 2015). The positive electrode or cathode is made of lithium-based layered metal oxide (e.g.,  $\text{LiMO}_2$ , where M is a transition metal ion such as Co, Mn, or Ni), while the negative electrode or anode is commonly made of graphite or carbon materials. Current collectors are used for facilitating efficient electron transfer between the electrode and the external circuit while also offering mechanical support to the active layer of the electrode (Beguin and Elzbieta, 2009). The anode and cathode's current collectors are usually copper and aluminum, respectively.

The operation of LIBs involves the movement of lithium ions, which is facilitated by the electrolyte consisting of lithium salts dissolved in organic carbonates. The reactions occur during charging and discharging by following equations 2.1 (Linden et al., 2002).

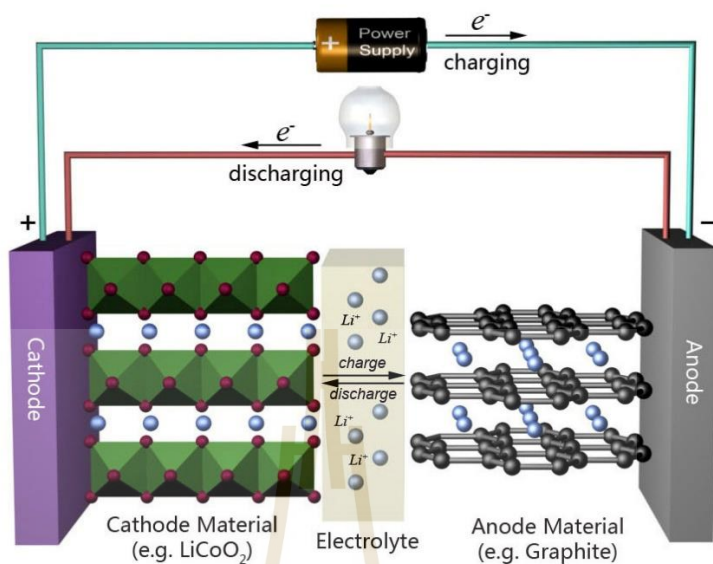
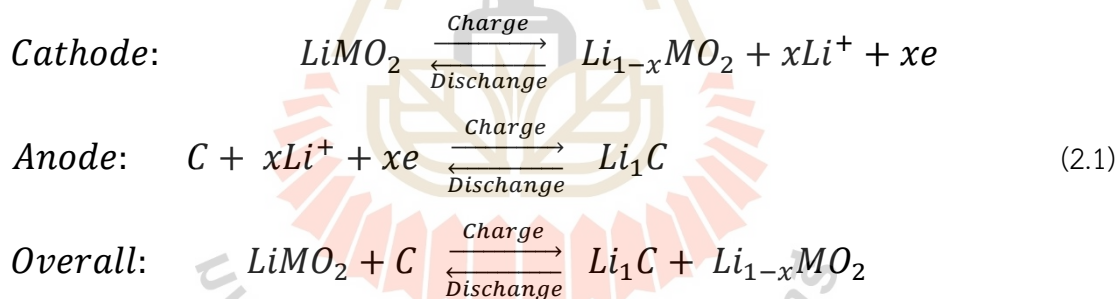


Figure 2.1 A schematic diagram of a typical LIB (Liu et al., 2011).



, where  $\text{LiMO}_2$  is transitional metal oxide.

When it is charged by an external source of current, Li ions from the  $\text{LiMO}_2$  cathode diffuse through the electrolyte to the anode. This makes the cathode of  $\text{LiMO}_2$  lithium-deficient while the anode is lithium-rich. As lithium is extracted from the cathode, this process is also called delithiation. During the discharge process, Li ions migrate through the electrolyte to the  $\text{LiMO}_2$  cathode. As a result, electrons will flow from the negatively charged electrode to the positively charged electrode. This process is called lithiation because the cathode obtains Li ions.

## 2.1.1 Cathode materials

**2.1.1.1 Lithium Cobalt Oxide (LiCoO<sub>2</sub>)– (LCO)** LiCoO<sub>2</sub> was first introduced by Prof. John B. Goodenough in 1980. It is in the family of transition metal oxides which is widely employed in rechargeable batteries. LiCoO<sub>2</sub> has a stoichiometric ratio represented as Li<sub>1-x</sub>CoO<sub>2</sub>, where x denotes lithium deficiency in the crystal structure. Its crystal structure adopts the alpha-NaFeO<sub>2</sub> structure, characterized by layered arrangements of lithium and transition metal ions separated by oxygen layers, facilitating lithium-ion intercalation and deintercalation during charge and discharge. The operating voltage range of LiCoO<sub>2</sub> cathodes is typically 3.7 to 4.2 volts (vs. the standard hydrogen electrode, SHE), enabling high energy density in lithium-ion batteries. While the theoretical capacity is around 274 milliampere-hours per gram (mAh/g), practical applications may exhibit slightly lower capacities[A8]. However, it has limitations including limited load capacity, low thermal stability, and a relatively short lifespan of 500-1000 cycles (Tarascon et al., 2001).

**2.1.1.2 Lithium Manganese Oxide (LiMn<sub>2</sub>O<sub>4</sub>) (LMO)** LiMn<sub>2</sub>O<sub>4</sub> has a spinel structure which enables the material to be discharged at high rates. LMO-based batteries are ideal for use in high-rate applications. The lithium-ion cell using LMO as the cathode material was first commercialized by Moli Energy in 1996. The three-dimensional spinel structure of LMO can enhance the ion flow on the electrode, resulting in decreased internal resistance and enhanced current handling. Their spinel structure also provides additional advantages, such as high thermal stability and increased safety. However, the cycles and calendar life of LMO based batteries are both limited. Low internal cell resistance permits fast charging and discharging with high current. LMO based batteries can be discharged at the currents between 20 and 30 A in an 18650 package with moderate heat generation. They are also feasible to apply up to 50A load pulses for up to one second. A continuous high load at this current would generate heat, and the temperature of the cell cannot exceed 80 ° C. LMO based batteries are used in power tools, medical equipment, hybrid and electric automobiles, and other applications (Buchmann, 2022).

### 2.1.1.3 Lithium Nickel Manganese Cobalt Oxide (LiNiMnCoO<sub>2</sub>) (NMC)

LiNiMnCoO<sub>2</sub>, commonly referred to as NMC, is a composite material consisting of nickel, manganese, and cobalt oxides. The composition of NMC can be adjusted to achieve a desired balance of energy density, power density, and stability. NMC cathodes have a high energy density, which allows for the storage of a significant amount of energy in a compact volume. Therefore, they are ideal for use in applications that require high energy density, such as electric vehicles and grid energy storage systems. NMC cathodes also have relatively good thermal stability, which helps to mitigate the risk of thermal runaway and enhance battery safety. However, NMC cathodes have certain drawbacks, including high cost and a susceptibility to capacity fading, a phenomenon that leads to a decline in battery capacity over time with repeated use. Furthermore, NMC cathodes can be susceptible to "cobalt bloating," a condition in which cobalt migrates from the cathode to the separator, leading to a reduction in overall battery performance (Buchmann, 2022).

### 2.1.1.4 Lithium Iron Phosphate (LiFePO<sub>4</sub>) (LFP)

LiFePO<sub>4</sub>, also known as LFP, is a widely used cathode material in LIBS. The material is characterized by a layered oxide structure, where lithium ions (Li<sup>+</sup>) intercalate between iron phosphate (FePO<sub>4</sub>) layers, thereby facilitating efficient flow of electrical charge during charging and discharging. LFP exhibits exceptional thermal stability, which minimizes the risk of thermal runaway and enhances battery safety. Moreover, the material has a low tendency for capacity fading, ensuring that the battery's capacity does not significantly decrease with repeated use. Furthermore, LFP is a cost-effective alternative to other cathode materials, making it a favorable choice for applications that prioritize cost. However, the energy density of LFP is relatively low compared to other cathode materials, which limits its capacity to store energy within a given volume (Buchmann, 2022).

## 2.1.2 Electrolyte

The proper operation of the Li-ion cell system, which involves facilitating the high transport of Li<sup>+</sup>-ions between the two electrodes, imposes specific requirements on the properties of the solvent and salt used. These requirements

encompass factors, such as optimal conductivity, stability, compatibility, and ability to mitigate side reactions, ultimately ensuring the reliable and efficient functioning of the system.

**2.1.2.1 Solvents** The selection of a suitable solvent for utilization in an LIB cell necessitates the presence of specific properties. These properties include the ability to dissolve the lithium salt, which corresponds to a high dielectric constant, as well as ensuring efficient ionic transport through a low viscosity. Furthermore, the solvent must exhibit both chemical and electrochemical stability, maintaining a liquid state across a wide temperature range. Lastly, it should be economically viable, safe, and nontoxic, taking into consideration the overall practicality and environmental impact (Sun et al., 2022). Differences in dielectric constant and viscosity are observed between cyclic and acyclic esters, rendering them distinct compounds. Cyclic esters tend to possess high dielectric constants and exhibit high viscosity, whereas linear esters generally exhibit low dielectric constants and maintain a more fluid state. In the context of Li-ion battery cells, the solvents most commonly employed are organic carbonates, including ethylene carbonate (EC), propylene carbonate (PC), dimethyl carbonate (DMC), diethylene carbonate (DEC), and ethyl methyl carbonate (EMC). These solvents have been extensively utilized due to their established suitability for the desired application (Xu Kang, 2004).

The operation of current LIBs relies on maintaining kinetic stability through the formation of a solid electrolyte interface (SEI) at the anode. During the initial cycles, a small amount of electrolyte undergoes sacrificial decomposition, leading to the formation of a protective film on the electrode surface. The composition of the SEI is influenced by both the electrolyte and the substrate, as highlighted in the work conducted by Peled et al. (Peled et al., 2004). Their experimental investigations revealed notable variations in the composition and morphology of the SEI formed on the basal and edge planes of graphite. Specifically, the film on the basal planes exhibited higher enrichment of organic compounds, albeit with a thinner morphology, while the film on the edge planes predominantly consisted of salt-reduction products. Functionally, the SEI acts as an ionic conductor and electronic insulator, facilitating the

continuous intercalation and deintercalation of Li<sup>+</sup>-ions while effectively preventing further electrolyte decomposition (Scrosati et al., 2010). The intercalation reaction in LIBs is solvent-dependent, with ethylene carbonate (EC) forming a protective SEI layer on the electrode surface, while PC fails to do so due to co-intercalation of PC molecules, resulting in graphene structure destruction known as exfoliation. As LIBs operate outside the stability range of organic solvents, SEI formation is crucial for stable operation, establishing EC as the preferred solvent. Despite EC exhibiting a slightly higher dielectric constant than PC, it has a relatively high melting temperature (~36°C) and high viscosity. To address these limitations in EC-based electrolytes, the addition of linear carbonates is crucial to expand the liquid range and reduce viscosity. This combination of linear solvents and EC represents the current state-of-the-art Li-ion battery electrolyte composition (Xu Kang, 2004).

**2.1.2.2 Salt** The salt used must meet specific requirements to ensure the proper operation of Li-ion cells. It should readily dissolve and dissociate completely in the solvents employed, allowing for efficient ion transport. The solvated ions derived from the salt should exhibit high mobility to facilitate effective ionic conduction. Moreover, the anions present in the salt should remain stable and not undergo oxidative decomposition at the cathode. Additionally, the chosen salt should be nontoxic and demonstrate chemical and thermal stability. Among the various options, lithium hexafluorophosphate (LiPF<sub>6</sub>) has emerged as the preferred salt for commercial Li-ion cells due to its well-balanced properties. However, it is crucial to note that LiPF<sub>6</sub> is highly sensitive to moisture, leading to the formation of hydrofluoric acid (HF) upon exposure. This moisture sensitivity and subsequent generation of HF can potentially contribute to cell degradation over time (Aravindan et al., 2011).

While LiPF<sub>6</sub> is the preferred salt, alternative lithium salts such as lithium hexafluoroarsenate (LiAsF<sub>6</sub>), lithium bis(trifluoromethanesulfonyl)imide (LiTFSI), and lithium bis(oxalato)borate (LiBOB) have been investigated for their suitability in Li-ion cells. Nevertheless, LiPF<sub>6</sub> retains its prominence due to its well-established balance of properties. Researchers are actively exploring methods to mitigate the moisture

sensitivity associated with LiPF<sub>6</sub> and are also exploring novel salt compositions as part of ongoing efforts to further enhance the performance of Li-ion cells (Xu Kang, 2004).

## 2.2 STRUCTURE OF LiCoO<sub>2</sub>

LiCoO<sub>2</sub> has a cubic close-packed structure, where Co<sup>3+</sup> and Li<sup>+</sup> ions occupy the octahedral sites between oxide ion layers in alternating positions. Co<sup>3+</sup> adopts a low spin configuration (t<sub>2g</sub><sup>6</sup>e<sub>g</sub><sup>0</sup>) within an octahedral oxygen environment. The t<sub>2g</sub> orbitals of Co<sup>3+</sup> and the oxygen 2p orbitals of π symmetry strongly overlap. If the t<sub>2g</sub>π\* orbitals, which are energetically separated from the e<sub>g</sub>σ\* orbitals, are fully occupied, then LiCoO<sub>2</sub> exhibits semiconductor behavior. When lithium is extracted from LiCoO<sub>2</sub>, the a-axis contracts and the Co-Co distance decreases from 2.83 Å in LiCoO<sub>2</sub> to 2.81 Å in Li<sub>0.9</sub>CoO<sub>2</sub>. The direct t<sub>2g</sub>-t<sub>2g</sub> Co-Co interaction across a shared octahedral edge becomes critical at a distance of 2.82 Å, leading to a narrow d-band. This electronic configuration change is consistent with the observed transformation from insulator to metallic behavior upon removing a small amount (10%) of lithium from LiCoO<sub>2</sub> (P.G. Bruce et al., 1997).

Two crystallographic structures of LiCoO<sub>2</sub> have been reported, depending on the temperature of synthesis. At low temperatures around 350 °C (LT-LiCoO<sub>2</sub>), a cubic spinel structure is formed, which transforms into a layered trigonal (also called hexagonal) structure at approximately 750 °C (HT-LiCoO<sub>2</sub>), (M.T. Czyzyk et al., 1992). The hexagonal and cubic structures have the same oxygen sub-lattice and are distinguished by the spatial arrangement of cations as shown in Figure 2.2. The HT-LiCoO<sub>2</sub> shows better electrochemical performance compared to that with the LT-LiCoO<sub>2</sub> (C. Daniel et al., 2015).

Gummow et al. use the neutron diffraction data to demonstrate that the structure of LT-LiCoO<sub>2</sub> is not perfectly layered. Furthermore, 6 percent of the cobalt ions are found to dwell in the octahedral (8a) sites of the lithium layers. It is believed that LT-LiCoO<sub>2</sub> has a spinel-related structure (space group Fd3m), which is based on a cubic closed-packed oxygen network with alternating cation layers composed of 0.75 Co, 0.25 Li, and 0.75 Li, 0.25 Co, which run perpendicular to each of the four cubic

[111] directions (Rossen et al., 1993). The spinel has an aspect ratio that is very similar to that of the ideal cubic close packed oxygen array ( $c/a = 4.899$ ), which may be found in the region of 4.900–4.914. (Gummow et al., 1992). Efforts to obtain the ideal  $\text{Li}_2[\text{Co}_2]\text{O}_4$  Spinel structure with a  $c/a$  ratio are not successful. It is referred to as a quasi-spinel phase because the cation distribution in this compound is intermediate between the layered and spinel structure (Gummow et al., 1992 and Rossen et al., 1993).

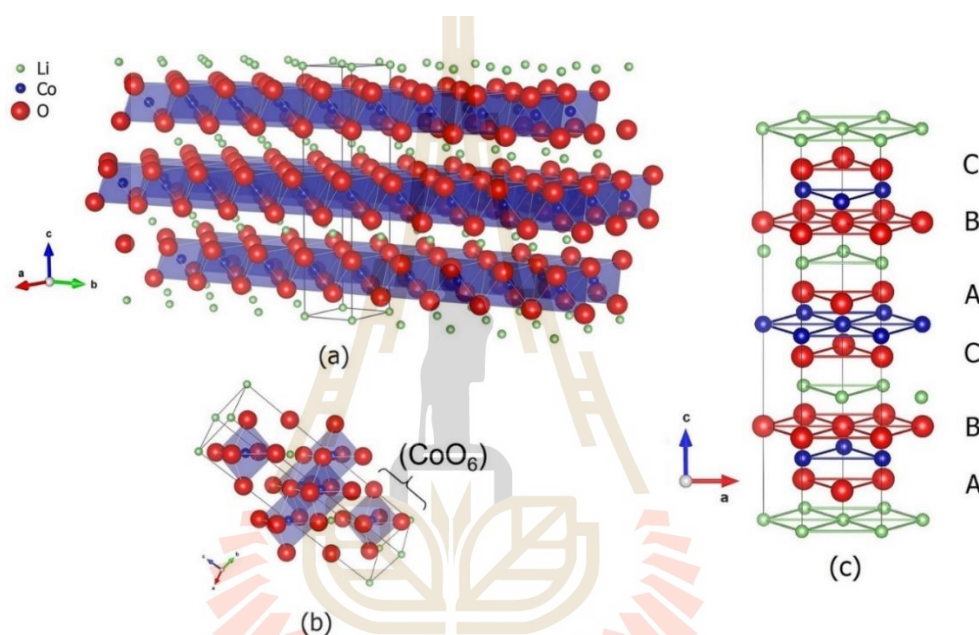


**Figure 2.2** (a) Layered crystalline structure of the rhombohedral  $\text{LiCoO}_2$ ; (b) representation of the octahedral  $\text{CoO}_6$  structure; (c) stacking arrangement of the layers (ABCABC) (Bruno G. A. Freitas et al., 2017).

In the most of LT- $\text{LiCoO}_2$  studies, the described product also contained HT phase and unreacted,  $\text{Li}_2\text{CO}_3$ , or  $\text{LiNO}_3$ , depending on the starting materials and synthesis process. The HT- $\text{LiCoO}_2$  has a trigonal structure (space group  $R\bar{3}m$ ,  $O_3$  phase) with the  $\text{NaFeO}_2$  layered structure, where Co and Li planes alternate in the ABCABC oxygen stacking (H.J. Orman et al., 1984). The cell parameters reported for the a-value (intralayer metal–metal distance) are in the range 2.815–2.816 Å, and those for the c-value are in the range 14.05–14.08 Å (interslab distance). The  $c/a$  ratio has a value in the range 4.98–5.00, which is significantly greater than that of a perfect cubic closed-

packed lattice ( $c/a = 4.899$ ). At first,  $\text{LiCoO}_2$  was prepared by solid state reaction. In solid state synthesis, the precursor is simply crushed and mixed together before being calcined at temperatures ranging 850–900 °C. This method of producing ceramic powder is both simple and cost-effective (Ermete Antolini, 2004). The preparation methods and the phase composition and morphological characteristics of LT- $\text{LiCoO}_2$  and HT- $\text{LiCoO}_2$  are reported in

Table 2.22 and

Table 2.2, respectively.

The HT- $\text{LiCoO}_2$  formation is also seen in the lower annealing temperatures when the different synthesis methods, especially wet techniques, are proceeded. Co-precipitation technique, hence, is another attractive technique for  $\text{LiCoO}_2$  synthesis. This wet chemical technique has been, generally, used to prepare nano powder of ceramics under ambient atmosphere and temperature (Chang et al., 2010; Dong and Koenig, 2020; Kim et al., 1999; Lala et al., 2003). It is simple, cost-effective, rapid, scalable and particle morphology controllable. However, the synthesized powder by this method yet needs to be calcined at high temperature after the preparation for the amorphous to crystalline structures transformation. Kim et al. synthesized the  $\text{LiCoO}_2$  by the co-precipitation method based on acetate solutions, lithium hydroxide and lithium peroxide solutions. The HT- $\text{LiCoO}_2$  was observed after annealing at 900 °C for 3 days, yielding the highest capacity of, approximately, 150 mAh/g in the range between 4.3–3.3 V (Kim et al., 1999). Chen et al. prepared the  $\text{LiCoO}_2$  nanoparticles by the co-precipitation method in ethanol solution with lithium and cobalt salts. It was reported that the annealed sample at 600 °C for 10 h showed the HT- $\text{LiCoO}_2$  structure with the best electrochemical properties (Chen et al., 2002). In addition, Ekwongsa et al. recently reported the structural investigations of  $\text{LiCoO}_2$  powder which prepared by the co-precipitation method from lithium and cobalt nitrate in ethanol solution (Ekwongsa et al., 2020). They studied the structural transformation of the  $\text{LiCoO}_2$  powder by conventional XRD and in-situ XAS techniques. The HT- $\text{LiCoO}_2$  structure was observed at 700 °C in their investigations. However, the nitrate by-products were not removed from their powders after preparations, and they actually needed to be

eliminated by deionized water. The washing process could deviate the investigation results.

**Table 2.1** Preparation methods, synthesis temperature and time, phase composition, and morphological properties of LT-LiCoO<sub>2</sub>.

| Reagents   | Preparation method and synthesis temperature and time    | Phase composition and morphological characteristics   | Ref.                       |
|--|--|---|----------------------------|
| LiCl–Li <sub>2</sub> CO <sub>3</sub> ,<br>CoCl <sub>2</sub>          | Molten salt synthesis<br>550 °C, 600 °C, 1 h             | Mixed LT- and HT-LiCoO <sub>2</sub><br>53% at 550 °C, 26% at 600 °C, particle size 10.95µm at 600 °C                            | (C.-H. Han et al., 2001)   |
| Li and Co nitrates   | Sol–gel with maleic acid, 500 °C, 1 h                    | Polycrystalline LT-LiCoO <sub>2</sub> , ultrafine particle size 0.03µm  | (I.H. Oh, et al., 1993)    |
| Li <sub>2</sub> CO <sub>3</sub> , Co (NO <sub>3</sub> ) <sub>2</sub> | Citrate sol–gel method 400 °C, 120 h                     | Mixed LT- and HT-LiCoO <sub>2</sub> , particle size < 1µm   | (S.G. Kang et al., 1999)   |
| LiOH, CoCO <sub>3</sub>  | Solid state synthesis<br>400 °C, 90 h                    | Mixed LT- and HT-LiCoO <sub>2</sub>   | (E. Rossen et al., 1993)   |
| LiOH, CoOOH  | Mechanical activation<br>400 °C, 4 h                     | LT-LiCoO <sub>2</sub>   | (N.V. Kosova et al., 2002) |
| Li <sub>2</sub> CO <sub>3</sub> , Co <sub>3</sub> O <sub>4</sub>     | Citric acid in the solid state reaction<br>300 °C, 100 h | Single phase LT-Li <sub>1+x</sub> CoO <sub>2</sub> (x=0.2, 0.0, 0.2, 0.4)<br>BET surface area 19 m <sup>2</sup> g <sup>-1</sup> | (K. Adhikary et al., 1998) |

**Table 2.2** Preparation methods and synthesis temperature and time, phase composition and morphological characteristics of HT-LiCoO<sub>2</sub>, ordered with decreasing synthesis temperature.

| Reagents   | Preparation method and synthesis temperature and time  | Phase composition and morphological characteristics                                  | Ref.                         |
|--|--|--|------------------------------|
| LiOH, Co(NO <sub>3</sub> ) <sub>2</sub>  | Cobalt-organic acid complexes route, 900 °C, 20 h  | Well-crystallized HT-LiCoO <sub>2</sub>  | (M. Yoshio et al., 1992)     |
| Li <sub>2</sub> CO <sub>3</sub> , Co <sub>3</sub> O <sub>4</sub> , Li/Co 1.00–1.05 | Hydrothermally precipitated Co <sub>3</sub> O <sub>4</sub> , followed by solid state synthesis, 800–900 °C, 10 h | Monodispersed HT-LiCoO <sub>2</sub> , particle size 3 μm (Li/Co 1.00) to 8 μm (1.05) | (T. Nakamura et al., 1999)   |
| Li and Co acetates   | Freeze drying synthesis 850 °C, 24 h   | Single phase HT-LiCoO <sub>2</sub>   | (O.A. Brylev et al. 2003)    |
| Li and Co nitrates   | Polyacrylic acid sol-gel method, 750 °C, 10 h  | Monodispersed rectangular HT-LiCoO <sub>2</sub> , particle size 0.5 μm               | (Y.K. Sun, 1999)             |
| Li and Co nitrates   | Combustion synthesis with urea 600, 700 °C, 12 h   | Single phase HT-LiCoO <sub>2</sub> , particle size 0.15 μm                           | (E.I. Santiago et al., 2003) |
| Li and Co nitrates   | Sol-gel method with polyacrylic acid 550 °C, 1 h   | Ultrafine uniformly sized HT-LiCoO <sub>2</sub> , particle size 0.03–0.05 μm         | (Y.K. Sun et al., 1996)      |
| Li <sub>2</sub> CO <sub>3</sub> , Co(NO <sub>3</sub> ) <sub>2</sub>                | Thermal pyrolysis of Co/Li citrate compositions, 400 °C  | HT-LiCoO <sub>2</sub> , particle size 0.07–12 μm                                     | (E. Zhecheva)                |
| LiOH and Co(NO <sub>3</sub> ) <sub>2</sub>   | Precipitation process in aqueous solution, 800 °C, 2 h   | Layered HT-LiCoO <sub>2</sub>  | (B. Garcia et al., 1995)     |

The presence of the hexagonal distortion leads to slight differences, most noticeable in the splitting of the spinel (222) diffraction peak into the hexagonal (006) and (012) peaks and also in the splitting of the cubic (440) peak into the hexagonal ((018) and the (110) peaks. In each case the sum of the hexagonal peak intensities in the HT-LiCoO<sub>2</sub> gives the same total intensity as the single cubic peak in LT-LiCoO<sub>2</sub>. The spinel (111), (331), (511) and (442) diffraction peaks are reflections of the superlattice structure of the slightly disordered cation arrangement, with a 2×2×2 super structure as shown in Figure 2.3. The spinel (222), (400), (440), (622) and (444) are independent of cationic ordering. Hence, solely the latter are observed for a rocksalt structure with random cationic occupation (M. Antaya et al., 1994).

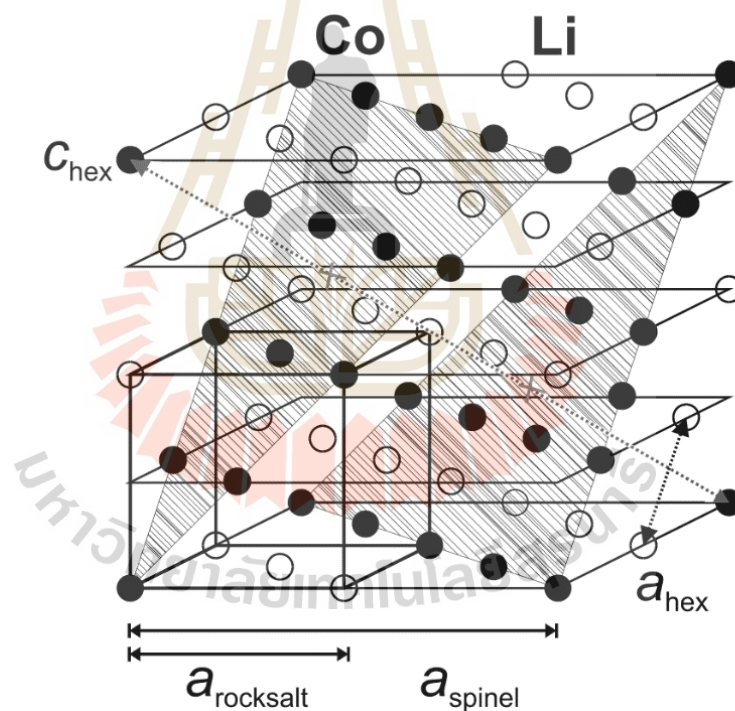


**Figure 2.3** Cationic positions and unit cell constants indicated for the hexagonal, spinel and rocksalt lattice structure (M. Antaya et al., 1994).

The behavior of electrochemical lithium insertion and removal in layered LiCoO<sub>2</sub> is strongly dependent on the orientations of the crystal structure. The crystallization of LiCoO<sub>2</sub> is more appropriate with the c-axis orientation due to the (003)

plane having the highest atomic density and the lowest surface energy of all planes. The c-axis oriented  $\text{LiCoO}_2$  crystals were determined to be preferentially dominated by (003) planes, and it was explained that a stronger (003) intensity led to a lower degree of cation disorder. Therefore, it is important to investigate effect of c-axis orientation on electrochemical performance of  $\text{LiCoO}_2$ . However, the effect of the air-controlled calcination process on the degree of c-axis orientation in  $\text{LiCoO}_2$  has not been investigated yet.

## 2.3 PREPARATION METHODS FOR $\text{LiCoO}_2$ POWDER

There are several methods that can be used to prepare the  $\text{LiCoO}_2$  powder, including solid-state synthesis, sol-gel synthesis, and precipitation method. These methods are discussed in more detail.

### 2.3.1 Solid-state synthesis

In this method, the oxide powders prepared by the mixture of carbonate or nitrate precursor and heated in a furnace at high temperature for long times (>10h) to produce  $\text{LiCoO}_2$ . The temperature and duration of heating can be adjusted to control the particle size and crystal structure of the  $\text{LiCoO}_2$  produced. Currently, this method has gained significant interested in synthesizing sodium-based oxides, notably  $\text{Na}_x\text{CoO}_2$  (Carrier et al., 2001), followed by an ion exchange in a hot lithium electrolyte solution to obtain lithium-substituted oxides with meta-stable crystal structures.

### 2.3.2 Sol-Gel Method

The sol-gel method is employed to produce  $\text{LiCoO}_2$  in a gel-like solution. This involves dissolving precursor materials, such as lithium nitrate and cobalt nitrate, in a solvent, such as ethylene glycol or propylene glycol. Subsequently, the solution is dried, typically through evaporation, resulting in the formation of a gel. To remove the solvent and any other volatile components and achieve the desired  $\text{LiCoO}_2$  structure, the gel undergoes calcination at elevated temperatures. The sol-gel process, known for its effectiveness in producing powders and coatings (Serebrennikova and Birss, 1997), offers various advantages for oxide synthesis.

One notable advantage of this method is the high porosity exhibited by the resulting oxides, which enhances their intercalation capacity. For instance,  $V_2O_5$  xerogels synthesized using the sol-gel method can accommodate 3.3  $Li/V_2O_5$  instead of the typical 1.5  $Li/V_2O_5$ . This increased intercalation capacity is likely attributed to the "open contact" established between the oxide and the electrolyte solution. Unlike solid-state reactions, the sol-gel process does not necessitate strict stoichiometric quantities, making it particularly advantageous for preparing transition metal oxides with cationic substitution. Amine et al. successfully synthesized  $Li_{1+x}Mn_{2-y}MyO_4$  systems (where  $M=Ni, Fe$  and  $0 \leq y \leq 0.5$ ) using the sol-gel method. In contrast, solid-state processing had resulted in the presence of NiO-phase impurities (Amine et al., 1996).

### 2.3.3 Coprecipitation Method

In the coprecipitation method, the precursor materials are precipitated out of solution by adding a suitable precipitating agent, such as sodium hydroxide. The resulting precipitate is then calcined to form the desired  $LiCoO_2$ . This method is often used to produce  $LiCoO_2$  with a well-defined crystalline structure and high purity. In a recent study by Ekwongsa et al. (2020), structural investigations were conducted on  $LiCoO_2$  powder prepared using the co-precipitation method from lithium and cobalt nitrate dissolved in an ethanol solution. The study revealed that the high-temperature HT- $LiCoO_2$  structure was observed at 700 °C.

### 2.3.4 Hydrothermal Method

In the hydrothermal method, the precursor materials are dissolved in a solvent and subjected to high-pressure, high-temperature conditions in a pressure vessel. The high pressure and temperature conditions cause the precursors to react and form the desired  $LiCoO_2$ . The  $LiCoO_2$  is then precipitated out of the solution. This method is often used to produce high-quality  $LiCoO_2$  with a well-defined crystalline structure and high purity. Tarascon et al. successfully synthesized electrochemically active  $LiCoO_2$  and  $LiNiO_2$  through the reaction of  $LiOH$  and  $H_xMO_2$  phases. The reaction was carried out at a temperature of 160°C (or even 100°C) and a pressure of 60 bar for a duration of two days. It was observed that longer reaction times resulted in powders

with higher surface areas, leading to larger irreversible capacities during cycling. For the improvement of electrochemical performance, annealing temperatures of approximately 250 °C were found to be sufficient in removing carbonate impurities and hydrolytic species. These annealing steps were crucial in enhancing the electrochemical properties of the synthesized materials. However, it is worth noting that ball-milling of the hydrothermally prepared  $\text{LiCoO}_2$  powder was found to have a detrimental effect on the reversible intercalation capacity. This milling process significantly increased polarization, impacting the overall performance of the material (Bouwman, 2002).

#### 2.4 THIN FILM SOLID STATE LITHIUM BATTERIES

Conventional rechargeable batteries use liquid electrolytes which have several limitations due to the presence of separators and liquid electrolytes, such as limited safety, lower energy density, and restricted size design. Therefore, there has been an attempt to develop all-solid-state micro-batteries, which can be conveniently compacted and provide greater flexibility for the design of stand-alone microelectronic devices. The working mechanism of the lithium solid state batteries is not significantly different from that of other LIBs. A schematic diagram of a planar all-solid-state microbattery is shown in figure 2.4. Similar to other typical LIBs, lithium microbatteries consist of two current collectors, two electrodes, and an electrolyte in between. The main difference between traditional lithium microbatteries and batteries is that the liquid electrolytes are replaced by solid electrolyte (Y. Wang et al., 2015 and J.Oudenhoven et al., 2011). Several families of solid electrolytes have been extensively studied and proposed for various applications. These include oxide-based electrolytes exemplified by garnet-type lithium lanthanum zirconium oxide (LLZO), which exhibit high ionic conductivity and exceptional stability, rendering them suitable for high-performance energy storage devices. Sulfide-based electrolytes, such as lithium thiophosphate ( $\text{Li}_3\text{PS}_4$ ) and lithium garnet sulfide ( $\text{Li}_7\text{La}_3\text{Zr}_2\text{S}_{12}$ ), have garnered significant attention due to their impressive ionic conductivity and compatibility with lithium

metal anodes. Polymer-based electrolytes, such as lithium-doped polyethylene oxide (PEO) and polyacrylonitrile (PAN), offer favorable mechanical flexibility and processability, making them viable for applications in flexible and thin-film batteries. Garnet-type electrolytes encompass materials such as NASICON and  $\text{Li}_{6.4}\text{La}_3\text{Zr}_{1.4}\text{Ta}_{0.6}\text{O}_{12}$ , exhibiting high ionic conductivity and finding utility in various battery chemistries. Furthermore, perovskite-based electrolytes, including strontium titanate ( $\text{SrTiO}_3$ ) and barium cerate ( $\text{BaCeO}_3$ ), hold promise with their good ionic conductivity and tunability through doping or composition modifications. Organic compounds, such as ionic liquids and gel electrolytes, have been explored as solid electrolytes, offering distinct advantages such as wide electrochemical stability windows and the potential for high ion transport. Additionally, research focuses on composite and hybrid solid electrolytes, combining diverse materials such as inorganic-organic hybrids and composite structures to enhance overall performance by capitalizing on the benefits of high conductivity and mechanical robustness from different constituents (Zheng et al., 2018).

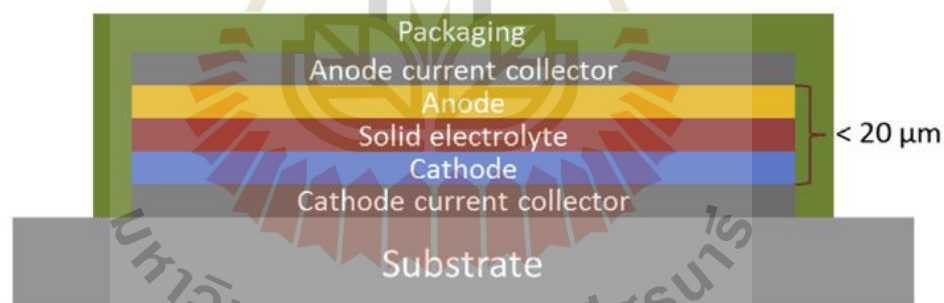


**Figure 2.5** A schematic representation of a planar all-solid-state microbattery.

#### 2.4.1 Preparation methods for $\text{LiCoO}_2$ thin film

For lithium microbatteries, the  $\text{LiCoO}_2$  thin films are usually employed as cathode materials (Wang et al., 2015). Preparation of the  $\text{LiCoO}_2$  thin films has therefore been the subject of numerous ongoing studies. Various deposition techniques can be applied to fabricate the  $\text{LiCoO}_2$  thin films for micro-battery, such as, radio frequency (RF) magnetron sputtering, spray pyrolysis, pulsed-laser deposition

(PLD), physical vapor deposition (PVD), etc. Each of these techniques is described in further detail below.

**2.4.1.1 Spray Pyrolysis** Spray pyrolysis involves spraying a precursor material solution over a heated substrate. The solvent evaporates, leaving behind a thin coating of the desired substance. The process is repeated until the desired film thickness is achieved. Spray pyrolysis is relatively simple and low-cost compared to other techniques, but it has lower deposition rates and film uniformity (P. Fragnaud et al., 1996).

**2.4.1.2 Pulsed-Laser Deposition (PLD)** PLD is a technique where a high-power laser is used to ablate the target material, which then condenses on a substrate to form a thin film. It has advantageous ability to achieve precise control of the film composition and thickness. It is particularly useful for depositing films with high structural integrity (C.Julien et al., 2001).

**2.4.1.3 Radio Frequency (RF) Magnetron Sputtering** RF magnetron sputtering is the most used technique for preparing  $\text{LiCoO}_2$  thin films. This technique can control the crystalline structure and surface roughness of materials with a similar chemical composition to the target material. A schematic diagram illustrating the basic components of a RF magnetron sputtering system is shown in Figure 2.7. In this technique, the surface of the material (target) is bombarded by high energy ions such as Argon ( $\text{Ar}^+$ ). Particles and atoms exchange energy and momentum, and the collision of these ions onto the target results in the removal of target atoms. The released atoms are ionic, traveling in an electric field, and they condense on the substrate as a thin film with a composition similar to the target material. Magnetron sputtering systems generate a strong magnetic field close to the target region, hence increasing the ion concentration by increasing the charged particle travel distance. The Lorentz force induces traveling electrons to spiral along magnetic flux lines near the target, which affects the chance of this charged particle colliding with more valuable particles, resulting in an adequate number of ions in the system. Moreover, with R.F. magnetron sputtering systems, the generated electrons travel a longer range, which increases the efficiency of the sputtering process. Although the basic concepts of operation are

simple, the sputtering process mechanism is complex. Currently, the RF magnetron sputtering is the method that is shown to be the most efficient for the deposition of a diverse selection of thin film materials. In many cases, magnetron sputtered films superior deposition compared with other techniques (B. Wanga et al.,1996).

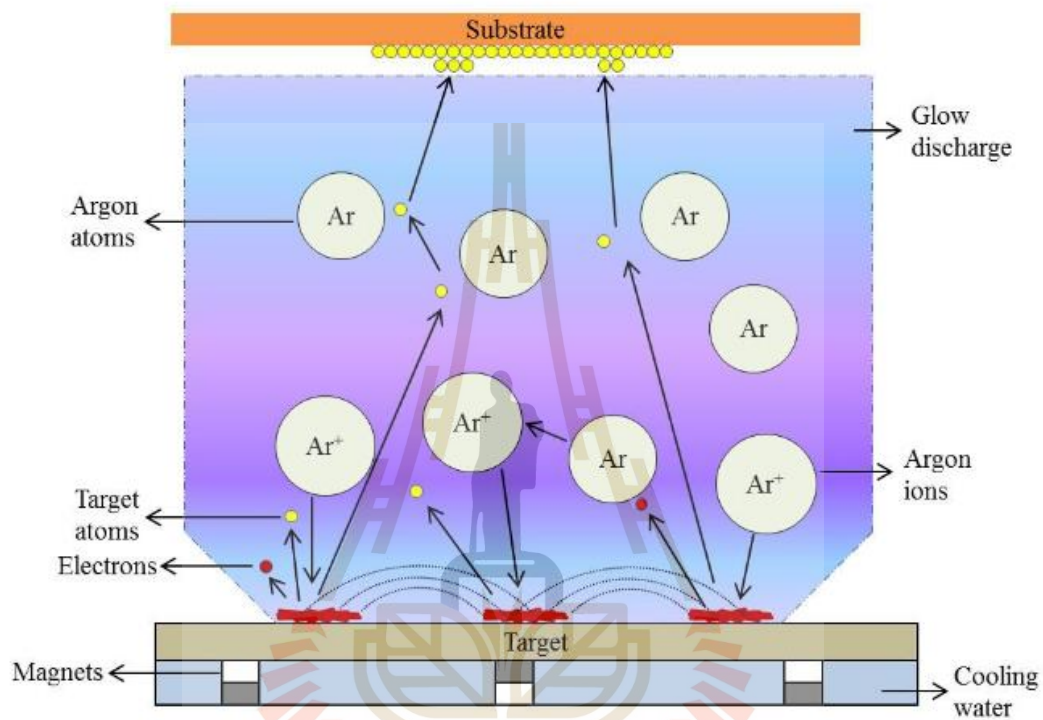


**Figure 2.6** Schematic diagram illustrating the basic components of a magnetron sputtering system.

Electrochemical properties of  $\text{LiCoO}_2$  thin film strongly depend on the sputtering conditions, such as gas flow rate, pressure, nature of the substrate, substrate temperature, deposition rate and annealing temperature. The preferential orientations of the  $\text{LiCoO}_2$  thin film also relate to the lithium diffusion at the electrode–electrolyte interface. There are three types of structural configurations (003), (101), and (104) as shown in Figure 2.7.

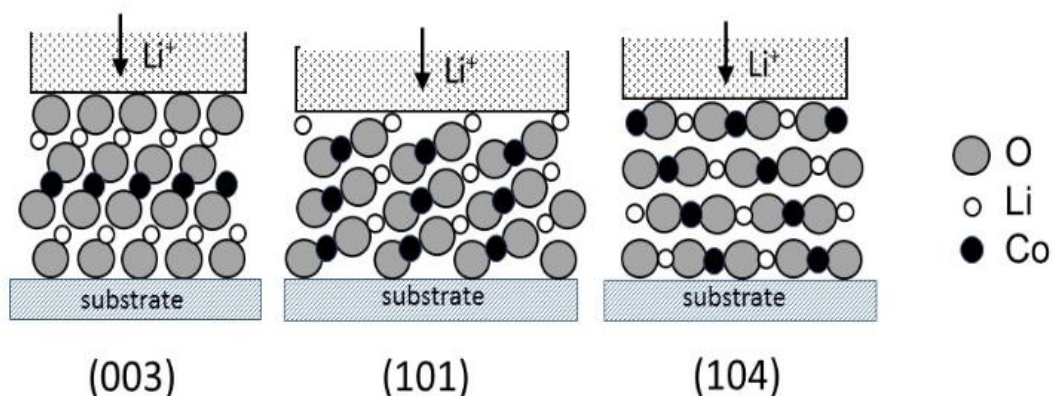


**Figure 2.7** Schematic diagram showing the preferred textures for sputtered  $\text{LiCoO}_2$  films.

Grain orientation in the (104) and (101) direction favors the  $\text{Li}^+$  ion transport, leading to high discharge capacity, because of  $\text{Li}^+$  ions can easily pass through the grain boundaries. Trask et al. studied the structural configurations dependent on various mixture  $\text{O}_2$  and Ar gas of the deposition process. Grain orientation in the (003) was not observed at 4%  $\text{O}_2$  in Ar after annealing at  $800^\circ\text{C}$  for 1 h, resulting in high capacity retention (Trask et al., 2017). Yoon et al. prepared  $\text{LiCoO}_2$  thin films on  $\text{Li}_2\text{O}/\text{Al}/\text{Si}$  substrates. The  $\text{LiCoO}_2$  thin films were deposited by RF-sputtering at various substrate temperatures to control the lattice orientations in order to maximize lithium-ion diffusivity in film textures. The reduction of (003) peak intensity was observed when the deposition substrate temperature was increased. The deposited substrate temperature at  $400^\circ\text{C}$  showed no detectable (003) peak of the as deposited and after annealing at  $500^\circ\text{C}$  for 2 h in air (Yoon et al., 2013). The reviews on experimental conditions for the preparation of  $\text{LiCoO}_2$  thin films by the rf-sputtering technique are reported in Table 2.3.

**Table 2.3** Experimental conditions for the preparation of LiCoO<sub>2</sub> thin films deposited by the rf-sputtering technique (Christian M. Julien et al., 2019).

| At<br>mosphere <sup>a)</sup> | Power(W)/<br>Deposition-<br>Rate (nm s <sup>-1</sup> ) | Substrate/<br>Temperature                       | Structural/Electrochemical Properties <sup>c)</sup>  | Ref.                                |
|------------------------------|--|---|--|-------------------------------------|
| 9:3/12/5                     | 100/-  | Si/SiO <sub>2</sub> /Ti/Pt/<br>250°C            | T <sub>a</sub> = 700°C, Q <sub>d</sub> = 61 μAh cm <sup>-2</sup> μm <sup>-1</sup> ; R <sub>c</sub> = 74%<br>after 50 cycles                            | (Liao and<br>Fung.,<br>2004)        |
| 3:1/40/0.5                   | 80/1.6   | Si/Ti/MgO/Pt/<br>10°C                           | T <sub>a</sub> = 800°C, Q <sub>d</sub> = 70 μAh cm <sup>-2</sup> μm <sup>-1</sup> @ 5 μA<br>cm <sup>-2</sup> ; R <sub>c</sub> = 30% over 40 cycles     | (Woo-<br>Seong<br>Kim.,2004)        |
| 96:4/50/0.5                  | 2.75 <sup>b)</sup> /0.3                                | Al <sub>2</sub> O <sub>3</sub> /Ti/Au/<br>110°C | T <sub>a</sub> = 800°C, Q <sub>d</sub> = 60 μAh cm <sup>-2</sup> μm <sup>-1</sup> @ C/10;<br>R <sub>c</sub> = 95% over 100 cycles                      | (Trask et<br>al., 2017)             |
| 9:1/-/0.5                    | 4.4 <sup>b)</sup> /-                                   | Al foil/200°C                                   | T <sub>a</sub> = 700°C, Q <sub>d</sub> = 52 μAh cm <sup>-2</sup> μm <sup>-1</sup> @ 50 μA  | (H. Hakan<br>Yudar et<br>al., 2018) |
| 5:1/150/0.2                  | 130/0.03   | Si/Au/Li <sub>2</sub> O/<br>65°C                | Q <sub>d</sub> = 46 μAh cm <sup>-2</sup> μm <sup>-1</sup><br>@ 5 μA cm <sup>-2</sup> ; R <sub>c</sub> = 78% over 100 cycles                            | (Jung pil<br>Noh et al.,<br>2012)   |
| 9:1/-/0.5                    | 150/0.1  | Stainless steel/<br>25°C                        | (101)-oriented; Q <sub>d</sub> = 40 μAh cm <sup>-2</sup> μm <sup>-1</sup><br>@ 20 μA cm <sup>-2</sup> ; R <sub>c</sub> = 78% @ 640 μA cm <sup>-2</sup> | (Yoon et<br>al., 2013)              |
| 4:1/150/0.27                 | 130/0.05   | Al foil/25°C                                    | Q <sub>d</sub> = 44 μAh cm <sup>-2</sup> μm <sup>-1</sup> @ 10 μA cm <sup>-2</sup> ; R <sub>c</sub> =<br>66% after 30 cycles                           | (Ki-Taek<br>Jung et al.,<br>2013)   |
| 3:1/53/2.2                   | 500/-  | Au/25°C   | T <sub>a</sub> = 500°C, Q <sub>d</sub> = 50 μAh cm <sup>-2</sup> μm <sup>-1</sup> @ 10 μA<br>cm <sup>-2</sup> ; R <sub>c</sub> = 80% after 800 cycles  | (S. Tintigna<br>et al., 2014)       |
| 3:1/12/2                     | 100/-  | Si/Pt/25-600°C                                  | T <sub>s</sub> = 250°C, T <sub>a</sub> = 600°C, Q <sub>d</sub> = 50 μAh<br>cm <sup>-2</sup> μm <sup>-1</sup> @ 10 μA cm <sup>-2</sup>                  | (C.L. Liao et<br>al., 2006)         |
| 9:1/-/0.5                    | 50/0.8   | Sapphire/SiO <sub>2</sub> /Al<br>/25°C          | T <sub>a</sub> = 500°C, thermal conductivity 3.7 W<br>m <sup>-1</sup> K <sup>-1</sup> for Li <sub>0.6</sub> CoO <sub>2</sub>                           | (Jiung Cho<br>et al., 2014)         |
| 9:3/12/0.5                   | 50/0.02  | Si/SiO <sub>2</sub> /Pt/<br>25°C                | T <sub>a</sub> = 800°C, Q <sub>d</sub> = 27 μAh cm <sup>-2</sup> μm <sup>-1</sup> @ 50 μA<br>cm <sup>-2</sup> after 150 cycles                         | (Jong-Ki<br>Lee et al.,<br>1999)    |

a) Composition of the Ar:O<sub>2</sub> gas mixture/flow rate sccm/chamber pressure in P<sub>a</sub>; b) Specific sputtering power in W cm<sup>-2</sup>; c) T<sub>a</sub> = optimum annealing temperature; Q<sub>d</sub> = specific discharge capacity; R<sub>c</sub> = capacity retention.

## 2.5 ADVANCED CHARACTERIZATION TECHNIQUES

### 2.5.1 X-ray absorption spectroscopy (XAS)

XAS is the powerful technique to investigate atomic local structure and electronic states. When X-rays of intensity  $I_0$  are incident on a sample, as shown in Figure 2.7, electrons bonded within an atom interact with the oscillating electric field of electromagnetic radiation. These electrons will either scatter the radiation or absorb it and excite the electrons.

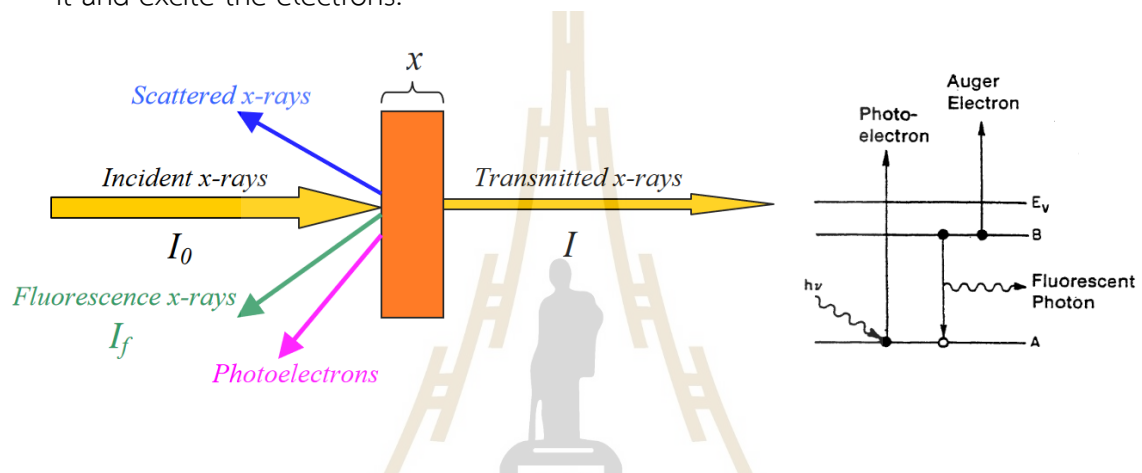


Figure 2.7 Schematic of incident and transmitted X-ray beam.

The electron X-ray absorptions can be explaining by following equations:

$$\mu x = \ln(I_0/I_1) \quad (2.2)$$

A monochromatic x-ray beam of intensity  $I_0$  pass through the sample,  $I_1$  is transmitted light intensity,  $x$  is thickness of the sample and  $\mu$  is transmission coefficient, which depends on the types of atoms. At certain energies where absorption rises dramatically, an absorption edge is created.

When X-ray energy is incident upon a material, surpassing the binding energy of a core shell, it initiates a sudden and significant enhancement in the absorption cross-section, resulting in the formation of an absorption edge. Each of these edges corresponds to a distinct core-electron binding energy and is designated by the principle quantum number. The symbol used to label the X-ray absorption edges is given in Figure 2.8.

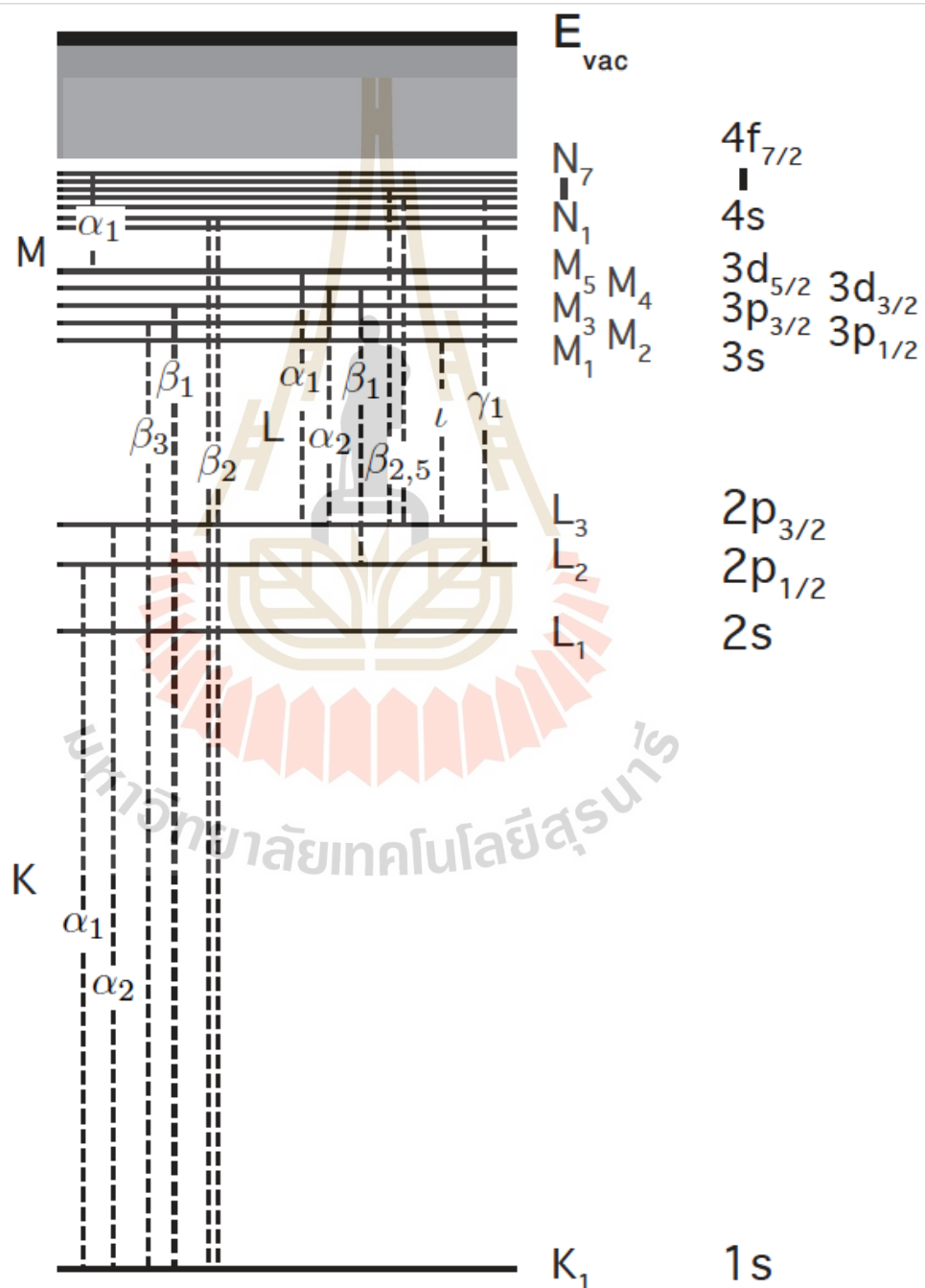


Figure 2.8 Diagram of the electron transition in inner shells (Thompson et al.,2001).

For example, the K edge represents the  $n=1$  shell, the L edge corresponds to the  $n=2$  shell, the M edge signifies the  $n=3$  shell, and so forth. Throughout the process of X-ray absorption, the incident photon energy is absorbed by the atom, leading to the excitation of electrons within the inner shells, specifically the K, L, or M shells, which undergo a transition to unoccupied valence bands situated above the Fermi level. However, due to the instability exhibited by the excited electron energy states, a subsequent transition occurs, whereby an electron from the subsequent energy state replaces the initially excited electron, giving rise to the emission of fluorescence, as illustrated in Figure 2.12. It is worth noting that while the core energy state tends to stabilize, the subsequent state remains inherently unstable. Consequently, another electron from the subsequent state undergoes a transition to the conduction band, commonly denoted as an "Auger electron."

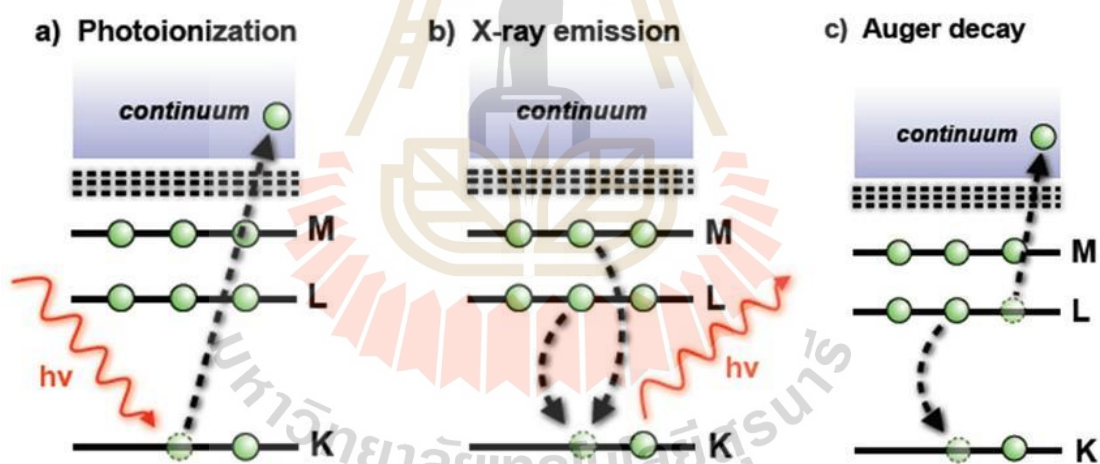


Figure 2.9 Mechanism of the x-ray absorption (a) X-ray absorption (b) Fluorescent X-ray emission and (c) Auger emission (Klysubun, 2006).

For instance, the Fe K-edge pertains to a transition where an electron is excited from the  $1s$  orbital to the  $3d$  orbital. However, this transition is typically forbidden according to the selection rule. Nevertheless, in the case of the compound FeO, the bonding between Fe and O influences the splitting of the  $d$ -orbitals into  $t_{2g}$  and  $e_g$  states. Subsequently, a mixing of  $d$ - $p$  orbitals occurs due to the ligand field theory. As

a result, the mixing of ligand p-character partially permits the previously forbidden transition. Conversely, the initial peak on the main edge originates from an allowed transition between the 1s and 4p bound states. On the other hand, the post-edge region corresponds to unoccupied states in the conduction band and involves the complete multiple scattering of spherical wave electrons with neighboring atoms. Additionally, X-ray Absorption Spectroscopy (XAS) can be categorized into X-ray Absorption Near Edge Structure (XANES), which concludes approximately 80-100 eV above the edge, and Extended X-ray Absorption Fine Structure (EXAFS), which begins approximately 50 eV above the edge, as depicted in Figure 2.10.

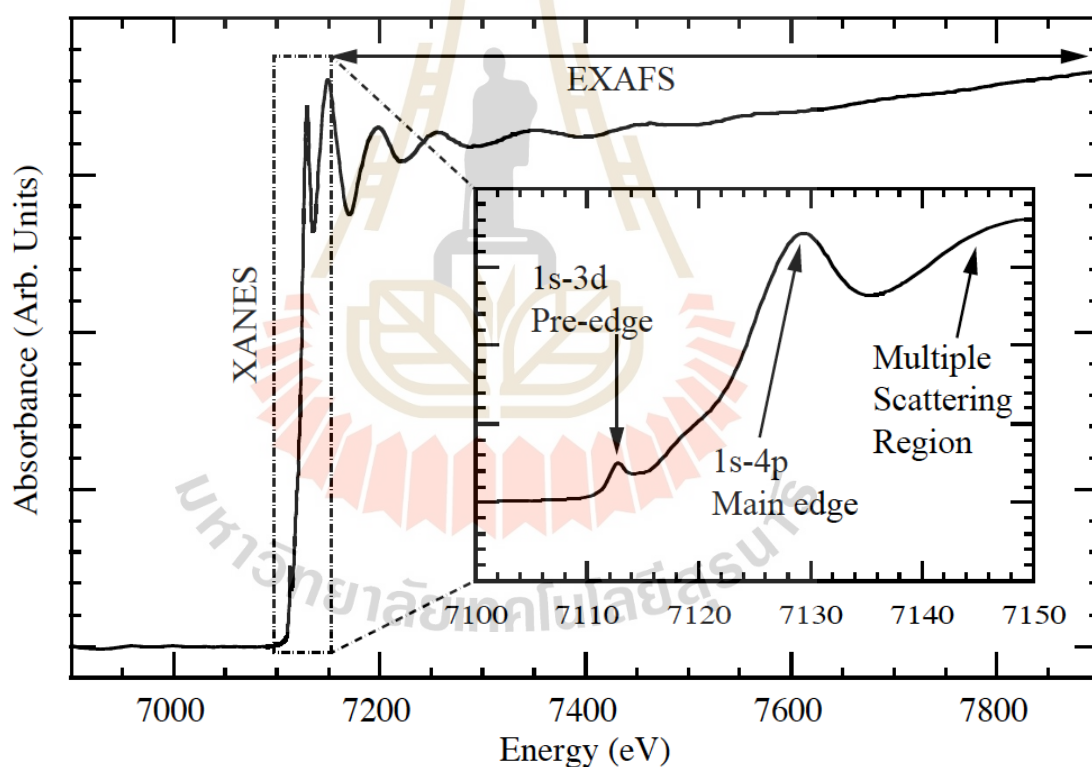


Figure 2.10 Theoretical and algorithm for XANES and EXAFS spectra (Natoli et al., 2014).

### 2.5.2 X-ray Absorption Near Edge Structure (XANES)

The X-ray absorption cross section, which can be expressed through the absorption coefficient using equation (2.3), can be derived by applying Fermi's Golden rule within the framework of the one-electron approximation (Sakurai, 1967; Ankoudinov, 1996).

$$\sigma(\omega) = \frac{2\pi}{\hbar\Phi_0} \sum_j |f \langle \vec{r} \cdot \hat{\epsilon} e^{i\vec{k}\cdot\vec{r}} | i \rangle|^2 \delta(E_i - E_f + \hbar\omega) \quad (2.3)$$

where  $|i\rangle$ ,  $|f\rangle$ ,  $E_i$  and  $E_f$  represent the initial and final states and their corresponding energies, respectively. The wave vector  $\vec{k}$ , x-ray photon flux  $\Phi_0$ , x-ray photon energy  $\hbar\omega$ , x-ray polarization vector  $\hat{\epsilon}$ , and Dirac delta function  $\delta(E)$  are also defined as per standard notation.

According to equation (2.xx), the absorption coefficient can be expressed in terms of the Dipole operator (D) as.

$$\mu(E) \propto \sum_j |f \langle \vec{D} | i \rangle|^2 \delta(E_i - E_f + \hbar\omega) \quad (2.4)$$

The relationship between the absorption coefficient and the transition rate of photoelectrons from state  $|i\rangle$  to the subsequent state  $|f\rangle$ , corresponding to the incident photon energy described by the Dirac delta function, is easily comprehensible. Additionally, the amplitude is connected to the dipole transition in the inner atom. However, in the XANES region, the absorption spectrum is predominantly influenced by the multiple scattering of low kinetic energy photoelectrons. The photoelectron's

associated wave propagates from the absorbing atom as a spherical wave, and this oscillation extends several hundred eV above the edge due to the back scattering of the outgoing spherical wave by neighboring atoms.

The photoelectron's scattering process can be characterized by employing the spherical potential approximation, commonly referred to as the muffin-tin approximation (Rehr and Albers, 2000; Kodre, 2002). Within this theoretical framework, the photoelectron experiences a potential denoted as  $V$ , which arises from individual contributions within distinct non-overlapping spherical regions of finite radius.

$$V = \sum_j v_n(\vec{r}) \quad (2.5)$$

The term  $v_n(\vec{r})$  represents the individual atom's contribution to the muffin-tin potential. Consequently, the muffin-tin potential comprises distinct, non-overlapping spherical areas. A visual representation of this potential can be observed in Figure 2.11. Outside these spherical regions, known as interstitial regions, the potential is set to zero. The determination of scattering amplitude and phase shift parameters is conducted independently for each scatterer, making them intrinsic to atomic properties.

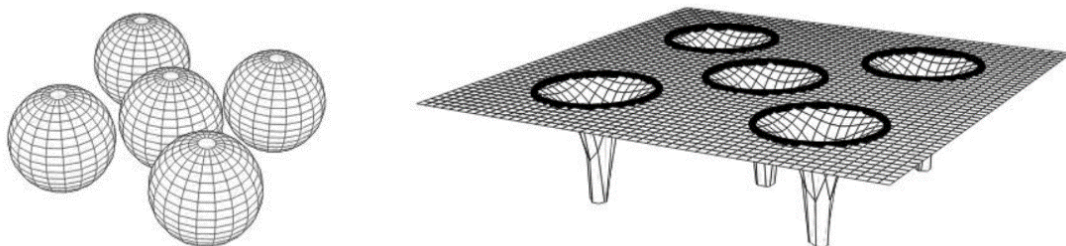


**Figure 2.11** The muffin-tin potential consist of non-overlapping spherical regions (Kodre, 2002).

### 2.5.3 Extended X-ray Absorption Fine Structure (EXAFS)

The extended X-ray absorption fine structure (EXAFS) refers to a noticeable pattern of oscillations observed in the x-ray absorption spectrum. These oscillations begin around 80 electron volts (eV) above the absorption edge and continue up to an energy range of approximately 1,000 eV. After the absorption edge, the incident X-ray photons transfer their energy to excite an electron, and any remaining energy becomes the kinetic energy of the resulting photoelectron.

The photoelectron can be described as spherical waves originating from the absorber atoms. When neighboring atoms are close to the absorber atoms, the photoelectron undergoes scattering, which causes it to return to the absorber atoms and significantly contributes to the overall EXAFS signal. This interaction between the incident and scattered waves is illustrated in Figure 2.12. It's worth noting that atoms located at the same distance from the absorber atom collectively contribute to a specific part of the EXAFS signal, forming what is commonly known as a "shell." (Groot et al., 1994; Hench and West, 1990). It is important to understand that the phase of the EXAFS signal changes depending on the wavelength of the photoelectron, which is closely related to the exact distance between the absorber and backscattering atoms. Additionally, the changes in backscattering intensity, observed as the energy of the photoelectron varies, are directly linked to the specific types of atoms involved in the backscattering process. Therefore, studying EXAFS comprehensively offers valuable insights into the intricate atomic surroundings of the central atom.

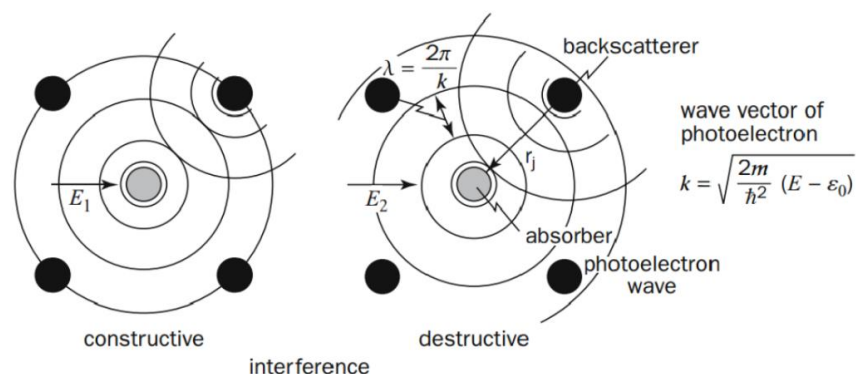


Figure 2.12 Interference of outgoing and backscattered photoelectron wave.

The EXAFS measurement focuses on analyzing the oscillatory component of the x-ray absorption spectrum beyond a specific absorption threshold. As a result, an EXAFS function can be defined by responsible for XAFS oscillation.  $E = \hbar\omega$  is the incoming photon energy (Hippert et al., 20060).

$$\chi(E) = \frac{[\mu(E) - \mu_0(E)]}{\Delta\mu_0(E)} \quad (2.6)$$

where  $\mu_0$  is the background absorption coefficient.  $\Delta\mu_0(E)$  is the absorption edge jump. The EXAFS function is typically described using the photoelectron wave number ( $k$ ) instead of the energy of the incoming X-ray photon. The simple relation between the two quantities is given by:

$$k = \sqrt{\frac{2m_e(E - E_0)}{\hbar^2}} \quad (2.7)$$

where  $E_0$  is the edge energy. It is defined as the energy corresponding to the first maximum of the derivative of the measured X-ray absorption spectrum (G. Bunker, 2010). By converting the EXAFS function from  $\chi(E)$  to  $\chi(k)$  it becomes applicable for general purposes.

The  $\chi(k)$  in the EXAFS equation can be understood in terms of the contributions from all scattering paths of the photoelectron (Stern and Heald, 1983). In real systems, there are typically multiple types of neighboring atoms surrounding a particular absorbing atom. The XAFS formalism easily accommodates this by summing the contributions from each scattering atom type, also known as the coordination shell or scattering path. The measured XAFS is a sum of these contributions. In general, the EXAFS equation expresses this summation of all paths (Stern and Heald, 1983s:

$$\chi(k) = \sum_j \frac{S_0^2 N_j}{kR_j^2} |f_j(k, \pi)| \sin [2kR_j + \varphi_j(k)] e^{-2\sigma_j^2 k^2} e^{-2R_j/\lambda(k)} \quad (2.8)$$

Each of the terms in the EXAFS equation is described below.

$S_0^2 N_j$  : These terms exert an influence on the amplitude of the EXAFS signal. The subscript  $j$  denotes that this parameter can vary for each path of the photoelectron. In the case of single scattering,  $N_j$  corresponds to the number of coordinating atoms within a specific shell. However, for multiple scattering,  $N_j$  represents the count of identical paths.  $S_0^2(k)$  is the term responsible for amplitude reduction, attributed to the many-body effect, and typically falls within the range of 0.7 to 1.0 (Li et al., 1995). Moreover,  $S_0^2(k)$  varies among different elements, although its value is generally transferable among different species of the same element and at the same edge.

$f_j(k, \pi)$  : This parameter represents the effective scattering amplitude within the context of the EXAFS analysis. In the case of a single scattering path, it corresponds to the atomic scattering factor. However, for multiple scattering events,  $f_j(k, \pi)$  denotes the effective scattering amplitude expressed using the single scattering formalism. Notably, this term characterizes the element sensitivity inherent in EXAFS measurements.

$1/R_j^2$  : This expression signifies the contribution arising from a group of atoms situated at a distance that diminishes as the distance from the absorber increases.

$\sin[2kR_j + \varphi_j(k)]$  ; This term explains the oscillations observed in the EXAFS signal, with the phase being determined by  $2kR_j + \varphi_j(k)$ . The path followed by the photoelectron is represented by  $2R_j$  (indicating the distance to the neighboring atom and back to the absorber atom), and this value is then multiplied by the photoelectron wave number  $k$  to derive the phase. Additionally,  $\varphi_j(k)$  represents a phase shift experienced by the photoelectron due to its interaction with the nuclei of the absorber atom and the nuclei of the coordinating atoms along its path.

$e^{-2\sigma_j^2 k^2}$  : Since not all coordinating atoms within a shell are consistently positioned at a distance  $R_j$  from the central absorber atom, the parameter  $\sigma^2$  quantifies the interatomic distance disorder. Specifically, it represents the mean-square displacement of the bond length between the absorber atom and the coordinating atoms within the shell. This term encompasses contributions arising from both dynamic (thermal) disorder and static disorder (structural heterogeneity).

$e^{-2R_j/\lambda(k)}$  : his exponential factor relies on  $\lambda(k)$ , which signifies the mean free path of the photoelectron, denoting the average distance the photoelectron traverses following its excitation.

Consequently, investigations of the EXAFS spectrum yield valuable insights into the quantity, identity, and inter-atomic distances of neighboring atoms relative to the absorbing atom. Nonetheless, within the EXAFS analysis, the parameter  $\chi(k)$  can be represented as a Fourier transform (FT) in R-space and expressed as follows:

$$\chi(R) = \frac{1}{2\pi} \int_0^{\infty} k^2 \chi(k) W(k) e^{i2kR} dk \quad (2.9)$$

To analyze and improve the EXAFS with the high  $k$  region, the plot  $\chi(k) \times k^2$  is taken into consideration and subjected to windowing through the application of a Hanning window  $W(k)$ .

#### 2.5.4 X-ray diffraction (XRD)

XRD is an analytical technique which is widely used for identifying the phase of crystalline materials and providing information on unit cell dimensions. XRD based on the constructive interference between monochromatic X-rays and a crystalline material. These X-rays are collimated and concentrated on the sample that cause the X-ray waves to be scattered from lattice planes, which causes constructive interference from a separated of waves at an interplanar distance of  $d$ . The detector

which travels in a circle around the sample records the number of X-rays that are observed at each angle  $2\theta$ . when conditions satisfy Bragg's Law equation is

$$n\lambda = 2d \sin \theta \quad (2.10)$$

where  $\theta$  is the scattering angle,  $n$  is a positive integer and  $\lambda$  is the wavelength of the incident wave. Bragg's law relates the wavelength of electromagnetic radiation to the diffraction angle and the lattice spacing in a crystalline sample.

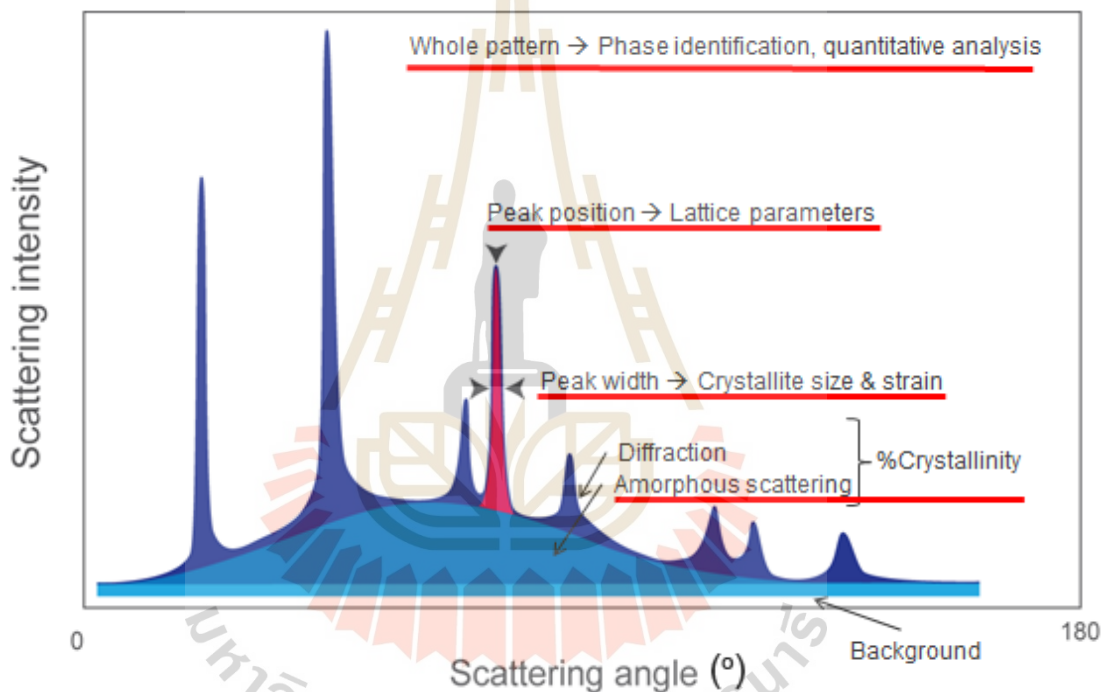


**Figure 2.13** A schematic of XRD pattern and information obtainable (<https://nptel.ac.in/courses/115103030/3>).

The characteristic x-ray diffraction pattern produced by a typical XRD examination provides a "fingerprint" of the crystals present in the sample. This fingerprint identifies the crystalline structure when correctly understood by comparison with conventional reference patterns and measurements. The determination of crystallite size and unit cell parameters can be calculated by Rietveld refinement. This method employs a least squares approach to iteratively adjust a theoretical line profile

until it closely aligns with the measured profile. The fundamental concept underlying the Rietveld method revolves around minimizing the sum  $S$  of squared differences between the intensity values of each point  $i$  in the pattern ( $y_{i0}$ ) and the corresponding values in the calculated profile ( $y_{ic}$ ) as:

$$S = \sum_i w_i (y_{i0} - y_{ic})^2 \quad (2.11)$$

where  $w_i$  is the statistical weight quality which is equal to  $1/y_{i0}$  and  $y_{ic}$  is the net intensity at point  $i$ .

The characterization of individual peak profiles in this study relies on common peak shape functions, predominantly the pseudo-Voigt or Pearson-VII functions. The pseudo-Voigt function is a linear combination of Lorentzian and Gaussian components (McCusker et al., 1999). To optimize the model function, the Rietveld algorithm minimizes the weighted sum of squared differences between observed and calculated intensity values, represented as the  $S$  value. The best fit between the raw and calculated diffraction patterns is evenly attributed both above and below the zero-difference line. For the structural model, the crystallographic information file (CIF) is commonly employed. The quality of the structural refinement can be assessed using various residual functions, such as the profile factor ( $R_p$ ), Weighted profile residual ( $R_{wp}$ ), Expected R-value ( $R_{exp}$ ), and Goodness of fit (GOF) (Toby, 2006).

$$R_p = \frac{\sum_{i=1,n} |y_{i0} - y_{ic}|}{\sum_{i=1,n} |y_{i0}|} \quad (2.12)$$

$$R_{wp} = \left[ \frac{\sum_{i=1,n} w_i (y_{i0} - y_{ic})^2}{\sum_{i=1,n} w_i y_{i0}^2} \right]^{\frac{1}{2}} \quad (2.13)$$

$$R_{exp} = \left[ \frac{N-P}{\sum_i w_i y_{i0}^2} \right]^{\frac{1}{2}} \quad (2.14)$$

$$GOF = \left[ \frac{R_{wp}}{R_{exp}} \right]^2 \quad (2.15)$$

The GOF is the ratio between  $R_{wp}$  and  $R_{exp}$  should be not lower than 1, which the good refinement should be give GOF values lower than 2.

In addition, the structural information, the determination of crystallite size can be calculated from the broadening of peak in a diffraction pattern by using the following Scherrer's equation.

$$D = \frac{K\lambda}{FWHM \cos \theta} \quad (2.16)$$

The value of K in the equation is influenced by the morphology of the particles. For instance, K equals 0.89 when dealing with spherical-shaped grains, whereas it is 0.94 for cubic-shaped ones. The symbols  $\lambda$ ,  $\theta$ , and FWHM represent the wavelength of X-ray radiation, the diffraction angle, and the full width at half maximum of the X-ray diffraction (XRD) peak, respectively.

### 2.5.5 X-ray photoelectron spectroscopy

XPS is an surface analysis technique that can provide information on the chemical composition of a material. In this technique, a sample of interest is irradiated with a monoenergetic soft X-ray, such as Mg  $K\alpha$  (1253.6 eV) and Al  $K\alpha$  (1486.6 eV). This results in the emission of free electrons, which is called photoelectron, due to the photoelectric effect. These photoemitted electrons are then collected and their kinetic energies are measured by a detector as shown in Figure 2.14.

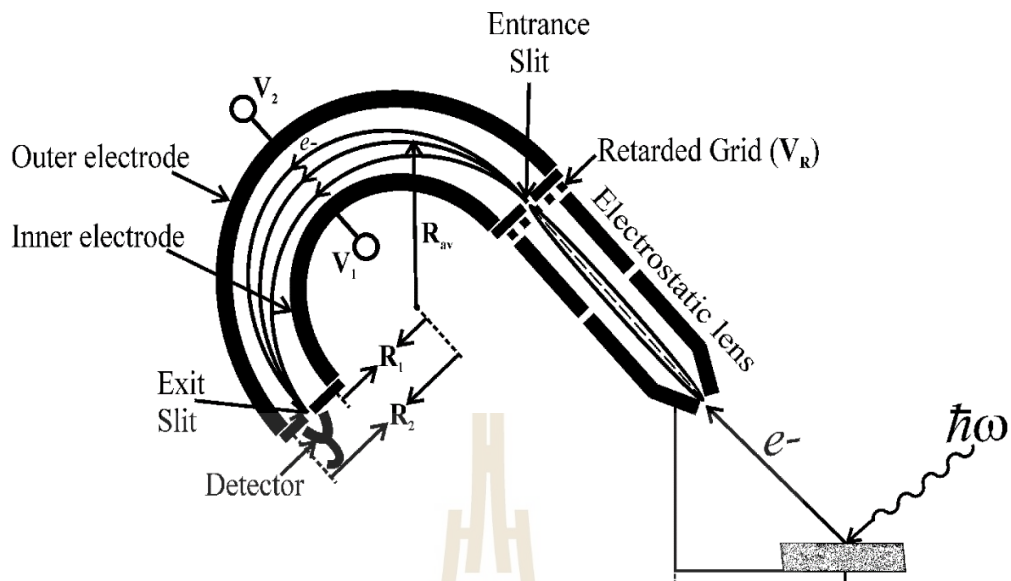


Figure 2.14 A schematic diagram of typical XPS experiment.

The kinetic energy of the photoemitted electrons,  $E_k$ , is related to the binding energy of electrons,  $E_B$ , in the following equation:

$$E_k = h\nu - E_B - \Phi \quad (2.17)$$

Where:  $h\nu$  is photon source energy.

$\Phi$  is work functions of probing element.

As the energy of the X-ray photons and the spectrometer work function are known, the binding energy of the emitted electrons can be simply calculated. The XPS spectrum is a plot of the number of photoelectrons as a function of their binding energy as shown in Figure 2.15, These provisions relating information on the distribution of electron energy in a material. Each element generates a characteristic peak of binding energy values which correlate to the electron configurations of the atom's electrons, such as 1s, 2s, 2p, etc. The peak shape and precise position provide chemical state information since the binding energy is dependent on the chemical environment.

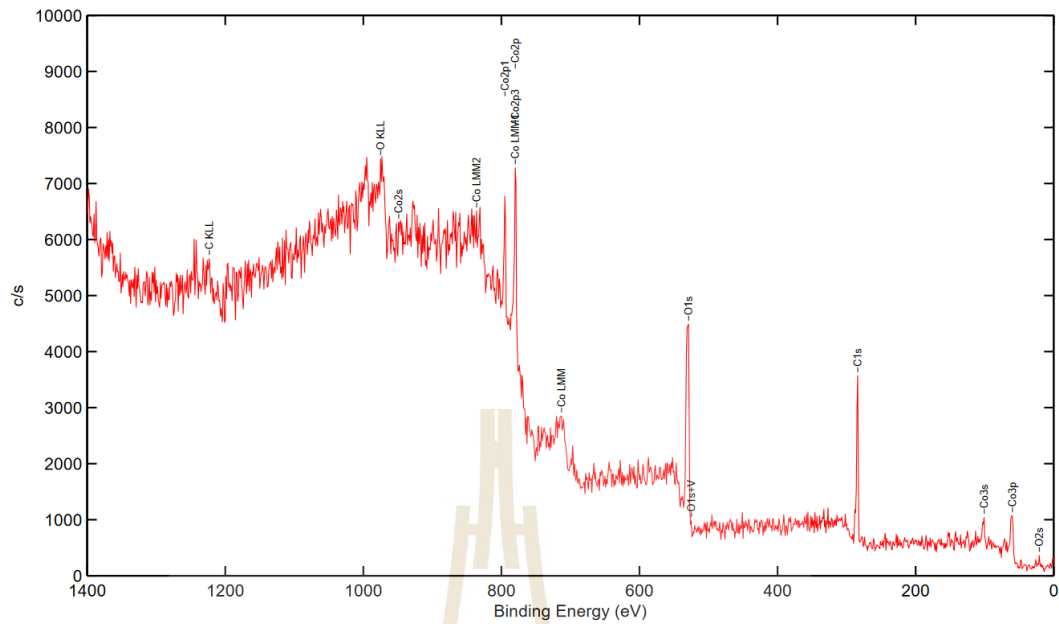


**Figure 2.15** XPS spectrum of lead showing the schematic of an electronic structure of  $\text{LiCoO}_2$ .

The peak areas can be used, with appropriate sensitivity factors, to determine the relative amount of the element represented by that peak present in the sample. The number of atoms per area  $N$  can be estimated by the following equation:

$$I_j = N\sigma_j\lambda_jK \quad (2.18)$$

Where The peak area ( $I_j$ ) of the peak  $j$  is expressed by:

$\sigma_j$  = Photoelectron cross-section (Scofield factor)  
as expressed by peak  $j$

$\lambda_j$  = Inelastic mean free path of a photoelectron  
as expressed by peak  $j$

$K$  = All other factors related to quantitative  
detection of a signal (assumed to remain  
constant during experiment)

From the Equation (2.19), the Relative atomic concentration of element  $i$  is expressed by

$$n_i = \frac{N_i}{\sum N_i} = \frac{I_i / \sigma_{ij} \lambda_{ij}}{\sum I_i / \sigma_{ij} \lambda_{ij}} \quad (2.19)$$

### 2.5.6 Raman Spectroscopy

Raman spectroscopy is a scattering and interference method used to examine rotational, vibrational, and other low-frequency modes in a system. It is extensively used in chemistry to generate a fingerprint spectrum that may be used to identify compounds. It is based on the inelastic scattering, or Raman scattering, of monochromatic light, often from a near-infrared, visible, or near-ultraviolet laser. As laser light interacts with molecular vibrations, phonons, or other excitations in the system, the energy of the laser photons is pushed upwards or downwards. The energy shift offers information on the vibrational modes of the system.

Typically, Raman system is mainly divided into two parts, input system and output system. The input system mainly consists of excitation laser source ( $h\nu_1$ ), and output system consists of scattered radiations ( $h\nu_2$ ). Figure 16 represent the principle of atomic vibration by transition state. The major elastic scattering is represented by the Rayleigh pattern. While scattering can occur from atoms or molecules, scattering between molecules can be inelastic due to a change in the molecule's rotational energy which was called Raman scattering. This inelastic pattern can arise for two mains type which are Stoke Raman scattering (higher own state) and anti-Stoke Raman scattering (lower own state). The interaction can be explained by using the following equations which are typically reported in wavenumbers:

$$\frac{1}{\lambda_{Raman}} = \frac{1}{\lambda_{incident}} - \Delta\bar{\nu} \quad (2.20)$$

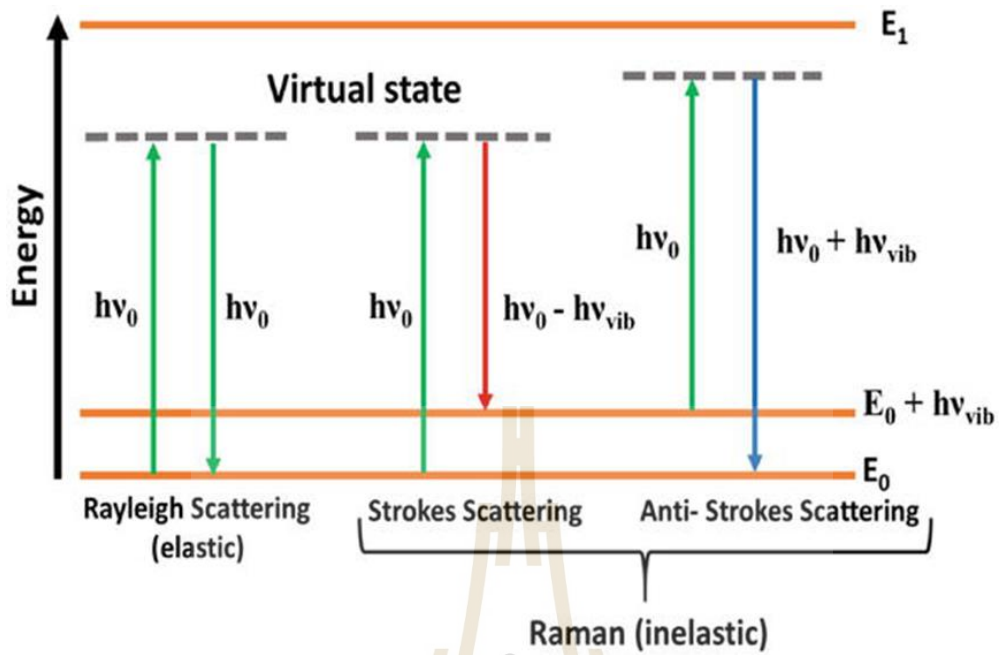


Figure 2.16 Basics principle of state diagram of scattering pattern.

Stoke Raman scattering  $\bar{\nu}_S = \bar{\nu}_I - \Delta\bar{\nu}$

Anti-Stoke Raman scattering  $\bar{\nu}_S = \bar{\nu}_I + \Delta\bar{\nu}$

Where:  $\bar{\nu}_S$  = Frequency of scattered photon ( $\text{cm}^{-1}$ )

$\bar{\nu}_I$  = Frequency of incident photon ( $\text{cm}^{-1}$ )

$\Delta\bar{\nu}$  = Frequency of Raman shift ( $\text{cm}^{-1}$ )

## CHAPTER III

### EXPERIMENTAL METHOD

This chapter provides information on the experiments conducted for this thesis. The details on materials, chemicals, and preparation of  $\text{LiCoO}_2$  powder and  $\text{LiCoO}_2$  thin film are given. The materials characterization with various techniques consisting of XRD, XAS, XPS, RAMAN and SEM are also described in this chapter.

#### 3.1 PREPARATION OF $\text{LiCoO}_2$ POWDER

In this work, the  $\text{LiCoO}_2$  powders were prepared by the co-precipitation method in ethanol solution and reacting with KOH solution. Briefly, 1.1 of  $\text{LiNO}_3 \cdot 6\text{H}_2\text{O}$  and 1M of  $\text{Co}(\text{NO}_3)_2 \cdot 6\text{H}_2\text{O}$  were dissolved in 100mL ethanol, and the mixture was stirred at room temperature for 1 h. 100mL of the mixture solution was precipitated in 3 M of KOH (dissolved in 500 mL ethanol) by rate value of 1 drop per second, and the mixture was stirred at room temperature for 1 h to promote  $\text{LiCoO}_2$  precursor solution. The precursor solution was separated by centrifuge at 7000 rpm for 10 min, then washed powders with ethanol until free from hydroxide ions and dried at 50 °C.

##### 3.1.1 Effect of thermal annealing temperature

The effect of thermal annealing on the structural properties of the prepared  $\text{LiCoO}_2$  powder was studied. The prepared  $\text{LiCoO}_2$  precursor was calcined at 300 °C, 400 °C, 500 °C, 600 °C, and 700 °C in air for 10 hours to obtain the  $\text{LiCoO}_2$  crystal. The obtained powders were washed with deionized water to remove potassium and nitrate and then dried at 100 °C. The structure of the annealed  $\text{LiCoO}_2$  powders were systematically studied by Syn-XRD, XAS, and dispersive Raman spectroscopy techniques. The Syn-XRD experiments were carried out at BL1.1W, SLRI, Thailand, while the XAS measurements were performed at BL5.2: SUT-NANOTEC-SLRI XAS, SLRI, Thailand. The surface morphologies and chemical compositions of the  $\text{LiCoO}_2$  powders were also characterized by FE-SEM and XPS techniques.

### 3.1.2 Influence of thermal annealing ambient

To study the influence of thermal annealing ambient, the dried  $\text{LiCoO}_2$  precursor was thermally annealed at 400, 500, 600, and 700 °C for 10 h under the flow of  $\text{N}_2$  (100 sccm) and the mixture of  $\text{O}_2$  and  $\text{N}_2$  (20 and 80 sccm, respectively). The final products were washed with deionized water until free from potassium nitrate ( $\text{KNO}_3$ ), and subsequently dried at 100 °C. The annealed  $\text{LiCoO}_2$  powders were characterized by XAS, XRD and SEM.

## 3.2 PREPARATION OF $\text{LiCoO}_2$ THIN FILMS

In this work, the  $\text{LiCoO}_2$  thin films were prepared by RF magnetron sputtering technique on the in-house system as shown in Figure 3.1. The system consists of turbomolecular and roughing pumps, compact full-range gauge (Pfeiffer Vacuum PKR 251), placed sputtering magnetron gun with a ceramic target, movable deposition stage, a cooling system for the magnetron gun, and a set of power supplies connected with a matching box.

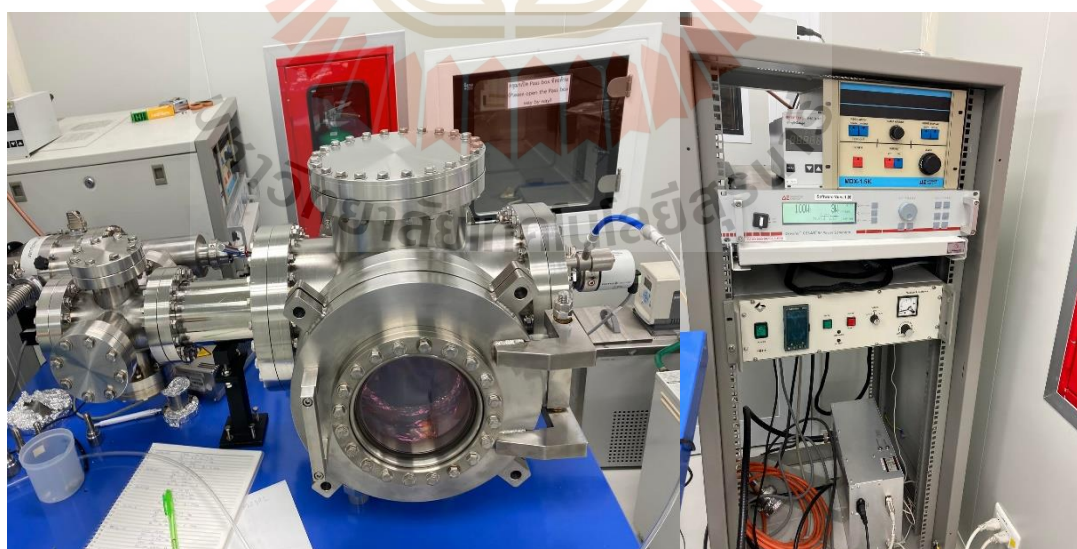


Figure 3.1 Photograph of the in-house sputtering system used in this thesis.

In the deposition, a 3-inch commercial target of  $\text{LiCoO}_2$  (Kurt J. Lesker, 99.9 % purity) bonded to copper plates was used. The  $\text{LiCoO}_2$  films were deposited onto glass slide substrates. Prior the deposition, the glass substrates were cleaned with ethanol and DI water and completely dried at 80 °C. The targets were pre-sputtered for at least 30 minutes to remove surface contaminations. The depositions were carried out under a working pressure of 2.6 Pa, which is required in order to ignite plasma. The distance between the substrate and the target was 5 cm and the RF power employed was fixed at 100 W. The mixture of argon (Ar) and oxygen ( $\text{O}_2$ ) was used as the process gas. The flow rate of pure Ar was fixed at 20 sccm, while that of  $\text{O}_2$  was varied between 1 to 7 sccm to study the influence of the process gas, and the deposition rate of  $\text{LiCoO}_2$  thin films is approximately about 6.7 nm/min, yielding the deposited thickness of approximately 800 nm for 120 minutes. No substrate heating was used in any of the experiments. The as-deposited  $\text{LiCoO}_2$  thin films were annealed at 500°C. The obtained films were preliminary characterized by XRD.

### 3.3 CHARACTERIZATIONS

#### 3.3.1 Syn-XRD

The Syn-XRD measurements were performed at BL1.1W: Multiple X-ray techniques at the Synchrotron Light Research Institute (SLRI), Thailand. This beamline utilizes the monochromatic synchrotron X-ray radiation energy of 12 keV and converted wavelength of 1.5409 Å. The photograph of the powder X-ray diffraction end-station of BL1.1W is shown in Figure 3.2. The prepared  $\text{LiCoO}_2$  powders were packed in Kapton capillary (diameter = 0.3 mm). The Syn-XRD data were collected in the  $2\theta$  scan range of 20–80° at room temperature and the capillaries were spun at 200 rpm during the measurements. The obtained patterns were refined by using the Jana2006 program.

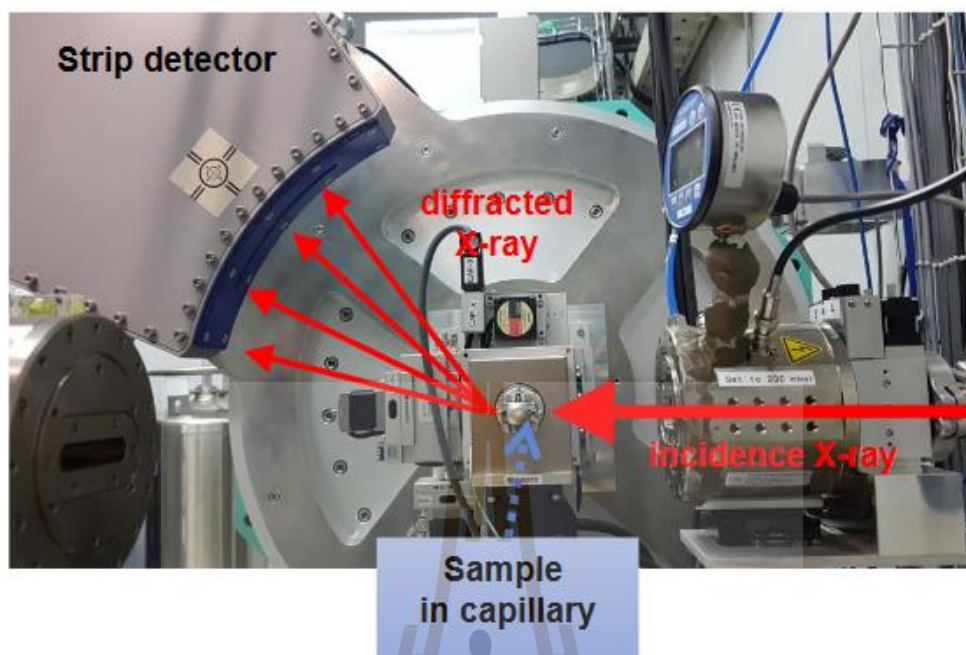


**Figure 3.1** A photograph of powder X-ray diffraction (PXRD) end-station of BL1.1W, SLRI.

### 3.3.2 XRD

The XRD experiments were performed using a Bruker D2 Advance diffractometer with Cu-K $\alpha$  radiation at scanning rate of 0.02°/min in the  $2\theta$  range from 10° to 80°. A freely available JANA2006 program was used for the structural refinement. The crystallographic orientation of cathode thin films was characterized by X-ray diffraction using a Rigaku Ultima IV with Cu-K $\alpha$  radiation. Data were collected in the  $2\theta$  scan range of 20–80° at room temperature.

### 3.3.3 XPS

The XPS spectra were collected by using a PHI5000 Versa probe II (ULVAC-PHI, Japan) equipped with a hemispherical electron energy analyzer, at the SUT-NANOTEC-SLRI joint research facility, SLRI, Thailand, as shown in Figure 3.3.A. A monochromatic X-ray (Al K $\alpha$ ) with an energy of 1486.6 eV was used for excitation.



Figure 3.3 A photograph of XPS of BL5.3, SLRI.

The XPS survey scans were collected between 0 and 1400 eV using a pass energy of 117.40 eV and an energy step of 1.0 eV. The high-resolution XPS spectra of elements of interest were collected with a pass energy of 46.95 eV and an energy step of 0.05 eV. The XPS spectra were analyzed by PHI Multipak XPS software. All XPS spectra were calibrated using the C1s peak at 284.8 eV as the binding energy standard. For peak deconvolution, the Shirley background subtraction and combinations of Gaussian-Lorentzian line shape were used.

### 3.3.4 XAS

In this thesis, the XAS experiments were carried out at two beamlines.

**BL5.2: SUT-NANOTEC-SLRI XAS** The XAS experiments, including XANES and EXAFS, were performed. The measurements at the Co K-edge were collected in transmission mode XAS. The intensities of the incident x-ray photon beam ( $I_0$ ) and the transmitted x-ray photon beam ( $I$ ) were measured using ionization chambers. These measurements were taken after modulating the energy of the incoming X-ray photons using an X-ray double-crystal monochromator. The monochromator employed Ge(220) crystal pairs at room temperature

**BL1.1W:** The measurements at the Co K-edge were made in FL mode using double crystal monochromator (DCM) at room temperature.

The EXAFS spectra were converted from k space to real space by applying a  $k^3$ -weighting factor and a Hanning window in the Fourier transformation process. In this study, the spectra obtained from XANES and EXAFS experiments were analyzed and compared with calculated spectra. Two software programs within the package were utilized for this purpose: 1) ATHENA, a tool designed for fundamental analysis of XAS spectra, and 2) ATHEMIS, a program specifically developed for the analysis of EXAFS data, including fitting experimental spectra with theoretical models provided by FEFF.

### 3.3.5 Raman spectroscopy

The Raman spectra was collected using an area-scan dispersive Raman microscope (SENTERRA, Bruker). The Raman scattering was captured from 25 points on a sample, with an excitation wavelength of 532 nm, power of 25 mW, and  $25 \mu\text{m} \times 1000 \mu\text{m}$  slit. The spectra were collected in a range of  $50\text{--}1520 \text{ cm}^{-1}$  with Raman shift resolution of  $0.5 \text{ cm}^{-1}$ .

### 3.3.6 SEM

In this work, the SEM images were taken by using FE-SEM (Carl Zeiss-AURIGA) to investigate the morphology including shape and size of the samples.

## CHAPTER IV

### RESULTS AND DISCUSSION

#### 4.1 EFFECT OF THERMAL ANNEALING ON THE STRUCTURE OF $\text{LiCoO}_2$ POWDERS PREPARED BY CO-PRECIPIATION METHOD

In this section, a fundamental study on structural characteristics of  $\text{LiCoO}_2$  powder prepared by co-precipitation method were performed. The effect of thermal annealing on the structure as well as the effect of washing process with deionized water on its chemical compositions of the  $\text{LiCoO}_2$  was investigated by Syn-XRD XAS, Dispersive Raman spectroscopy, FE-SEM, and XPS techniques.

##### 4.1.1 XRD

The Syn-XRD patterns of the prepared  $\text{LiCoO}_2$  powders after washing with deionized water were shown in Figure 4.1. The patterns of the prepared  $\text{LiCoO}_2$  powders matched well with the hexagonal- $\text{NaFeO}_2$  structure, COD-1550397 (space group R-3m). The second phases of  $\text{Co}_3\text{O}_4$  and chemical residuals, such as,  $\text{KNO}_3$ , were not detected in the patterns. Hence, the HT- $\text{LiCoO}_2$  phase acquisition was affirmed throughout the annealed temperature range. However, the splitting doublets of the  $(0\ 0\ 6)/(1\ 0\ 2)$  and  $(1\ 0\ 8)/(1\ 1\ 0)$  peaks which were at around  $37^\circ$  and  $67^\circ$ , respectively, were hardly observed at  $300^\circ\text{C}$ . Those doublets were used to identify the HT- $\text{LiCoO}_2$  structure. The broadening of diffraction peaks was due to the crystallite size effect which will be discussed later. The two doublets started to be distinguishable with the annealing temperatures of  $400^\circ\text{C}$  which clearly indicated the existence of HT- $\text{LiCoO}_2$  phase at the annealing temperature as such. The observation of HT- $\text{LiCoO}_2$  phase with this annealing temperature was in good agreement with Chen, et al. and Akimoto, et al., (Akimoto et al., 1998; Chen et al., 2002). The observation was also lower than the reports by Kim et al. ( $900^\circ\text{C}$ ), Chen et al. ( $600^\circ\text{C}$ ) and Ekwongsa et al. ( $700^\circ\text{C}$ ) (Kim et al., 1999; Chen et al., 2007; Ekwongsa et al., 2020).

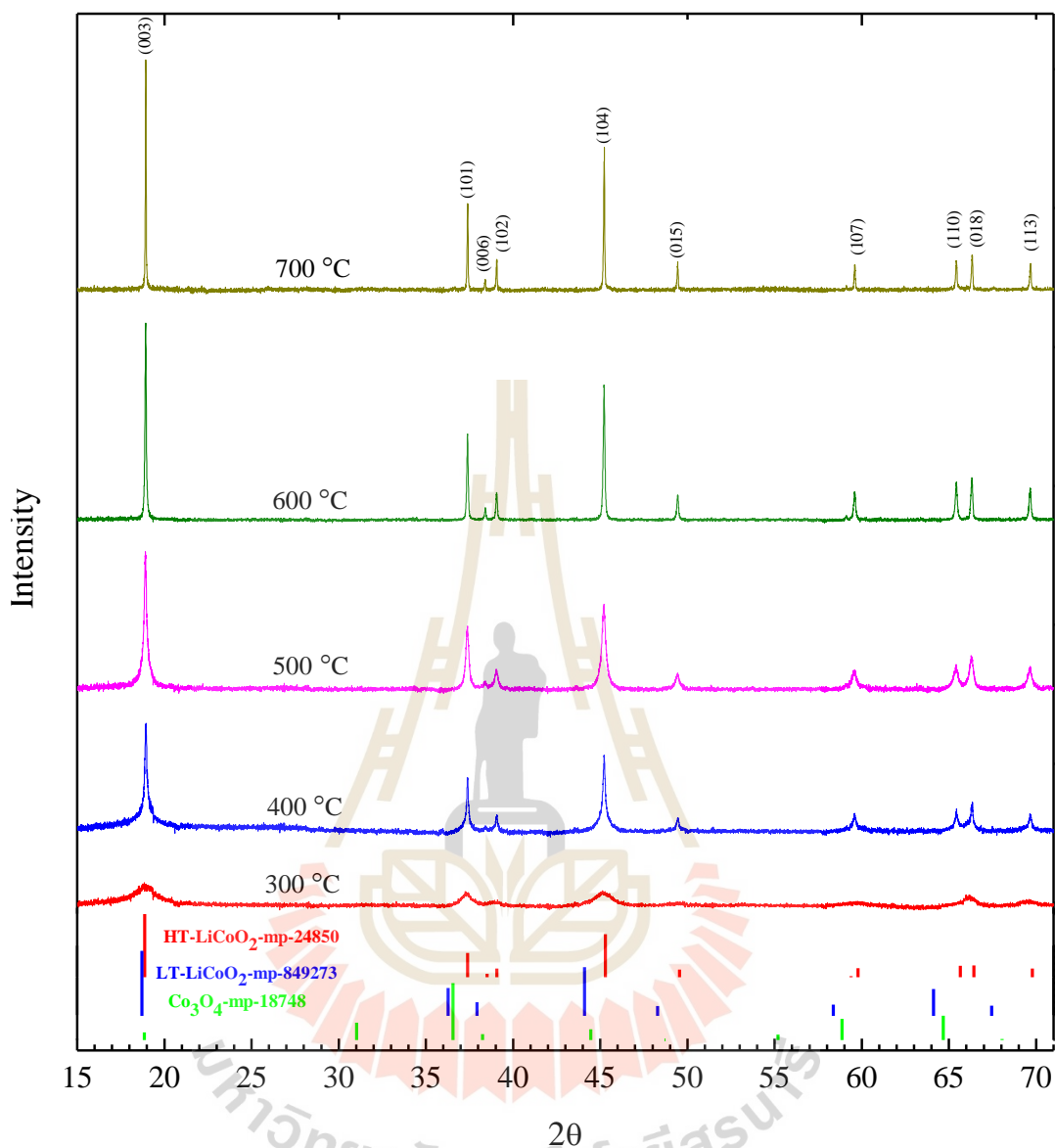


**Figure 4.1** Syn-XRD patterns of the prepared  $\text{LiCoO}_2$  powders annealed at different temperatures for 10 h.

As mentioned above, the Syn-XRD patterns showed HT- $\text{LiCoO}_2$  phase at the annealing temperature range of 400-700 °C. The crystallite size and hexagonal unit cell parameters of those annealed samples were calculated by Rietveld refinement as listed in Table 1. The average crystallite sizes were  $45.9 \pm 2.7$  nm,  $44.3 \pm 2.4$  nm,  $89.98 \pm 3.0$  nm and  $140.2 \pm 5.7$  nm which were obtained from the annealed samples at temperature of 400, 500, 600 and 700 °C, respectively. It was clearly seen that the

crystallite size tended to increase with the increase of the annealing temperature. Moreover, peak broadening is generally related to the crystallite size decrease. Therefore, the broad peaks were usually observed at lower annealing temperature due to the smaller of atomic diffusion. The Syn-XRD pattern of the annealed powder at 300 °C which should possess the smallest crystallite size, hence, revealed the noticeable broad peaks and the miserably observable splitting of the (0 0 6)/(1 0 2) and (1 0 8)/(1 1 0) doublets.

The lattice constant  $a$ ,  $c$  and  $c:a$  ratio of the annealed  $\text{LiCoO}_2$  powders at 400, 500 600 and 700 °C were (2.8185 Å, 14.0419 Å, 4.98204), (2.8171 Å, 14.0558 Å, 4.98946), (2.8168 Å, 14.0542 Å, 4.98942) and (2.8165 Å, 14.0534 Å, 4.98967), respectively, which were not significantly different. These lattice parameters were also close to those obtained in previous reports by Lee et al. (2.8134 Å, 14.050 Å and 4.994), Gummow et al. (2.8179 Å, 14.0597 Å and 4.99) and Sun et al. (2.8134 Å, 14.0411 Å and 4.9908) (Gummow et al., 1992; Lee et al., 2008; Sun, 1999).

As seen from the syn-XRD patterns, the highest intensity was from the (003) reflection followed by the (104) and (101) reflection, as expected from the diffraction data of pure  $\text{LiCoO}_2$  (mp-2485). The strong intensity of the (003) peak suggested that the samples exhibited a well-developed layers structure and preferred c-axis orientation (Weiping et al., 1998). The relative intensity ratio between (0 0 3) and (1 04) peak ( $I_{003}/I_{104}$ ) was used to determine the degree of c-axis orientation (Weiping et al., 1998; Gao et al., 2015). As seen from Table 1, the  $\text{LiCoO}_2$  powders obtained from this work exhibited a significant low  $I_{003}/I_{104}$  value compared to the values of 16.5 and 24 which were obtained from the previous studies by Gao et al. and Weiping et al., respectively (Weiping et al., 1998; Gao et al., 2015). The low c-axis oriented structure has been proposed to exhibit better electrochemical properties due to the consequential shorter diffusion distances for lithium ions (Gao et al., 2015).

**Table 4.1** The lattice parameters of the  $\text{LiCoO}_2$  powders annealed at different temperatures.

| Samples | a (Å)  | c (Å)   | c/a     | Goodness of fit (GOF) | Residual of least-squares refinement (Rp) | Weighted residual (wRp) | $I_{003}/I_{104}$ | crystallite size (nm) |
|---------|--------|---------|---------|-----------------------|---|-------------------------|-------------------|-----------------------|
| 400     | 2.8185 | 14.0419 | 4.98204 | 3.78                  | 14.72                                     | 20.23                   | 1.5009            | 45.9 ± 2.7            |
| 500     | 2.8171 | 14.0558 | 4.98946 | 1.23                  | 5.29                                      | 6.72                    | 1.5778            | 44.3 ± 2.4            |
| 600     | 2.8168 | 14.0542 | 4.98942 | 0.97                  | 5.59                                      | 7.15                    | 1.4318            | 89.98 ± 3.0           |
| 700     | 2.8165 | 14.0534 | 4.98967 | 0.96                  | 4.06                                      | 5.18                    | 1.5479            | 140.2 ± 5.7           |

#### 4.1.2 XAS

The normalized XANES spectra at the Co K-edge of the annealed  $\text{LiCoO}_2$  powders and commercial standard  $\text{LiCoO}_2$  (Com-STD) were shown in Figure 4.2. The absorption edge energies of Co were observed at 7717.7 eV, approximately, from all annealed  $\text{LiCoO}_2$  powders. This suggested the unchanged oxidation state of Co within the annealing temperature range. The increase of the low energy shoulder feature (A), around 7720 eV, and the changes of the shape and height of the whiteline (B), around 7730 eV, with annealing temperature were observed. When the annealing temperature was increased from 300 to 500 °C, the shoulder A increased while the whiteline B changed. When the temperature increased upto 600 °C, the shoulder disappeared with the significant increase of the whiteline. There were not any further observable changes in the XANES spectra between annealed samples at 600 and 700 °C. Moreover, the spectra of these two samples were almost identical as well as the spectrum of the commercial standard  $\text{LiCoO}_2$ .

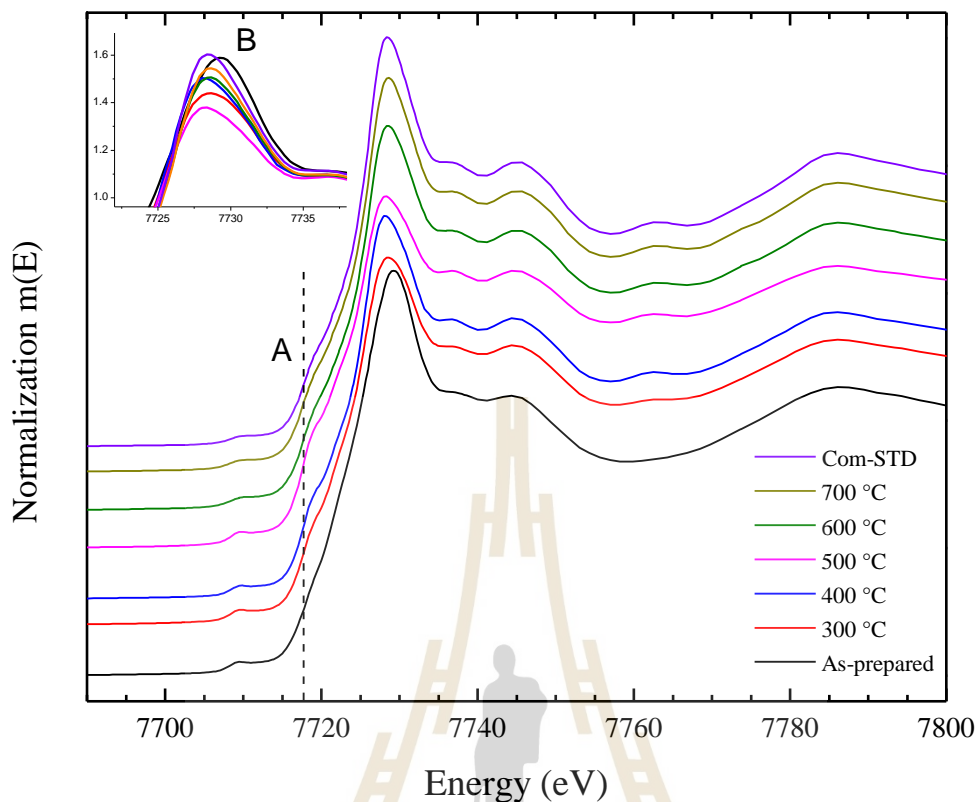


**Figure 4.2** XANES spectra of Co K-edge of the  $\text{LiCoO}_2$  samples annealed at different temperatures for 10 h.

The shoulder and whiteline features corresponded to the  $1s-4p$  transition which the former implicated the ligand to metal charges transfer with the shakedown process and the latter was without the shakedown process. The observed shoulder feature and low intensity whiteline at the low annealed samples could be a result of the overlapped O  $2p$  and the hybridized Co  $3d-4p$  orbitals which caused by tilted arrangement of  $\text{CoO}_6$  octahedra. The arrangement changed at higher annealing temperature such that  $3d-4p$  mixing reduced and caused the disappearance of the shoulder feature and the increase of whiteline intensity (Patridge et al., 2013; Ching-Hsiang Chen et al., 2007). Thereby, although it was suggested by the Syn-XRD results that the formation of HT- $\text{LiCoO}_2$  structure occurred at  $300^\circ\text{C}$ , the structure was incomplete. According to the XANES information, the minimum annealing temperature should be at  $600^\circ\text{C}$  for the complete HT- $\text{LiCoO}_2$  structure.

The  $k^3$ -weighted Fourier transform EXAFS spectra at the Co K-edge of the  $\text{LiCoO}_2$  powders with different annealing temperatures were illustrated in Figure 4.3. The results revealed two main peaks which correspond to Co-O and Co-Co. The amplitude ratio of Co-Co/Co-O grew when the annealing temperature increased suggesting the changes of  $\text{CoO}_6$  arrangement according to the XANES results.

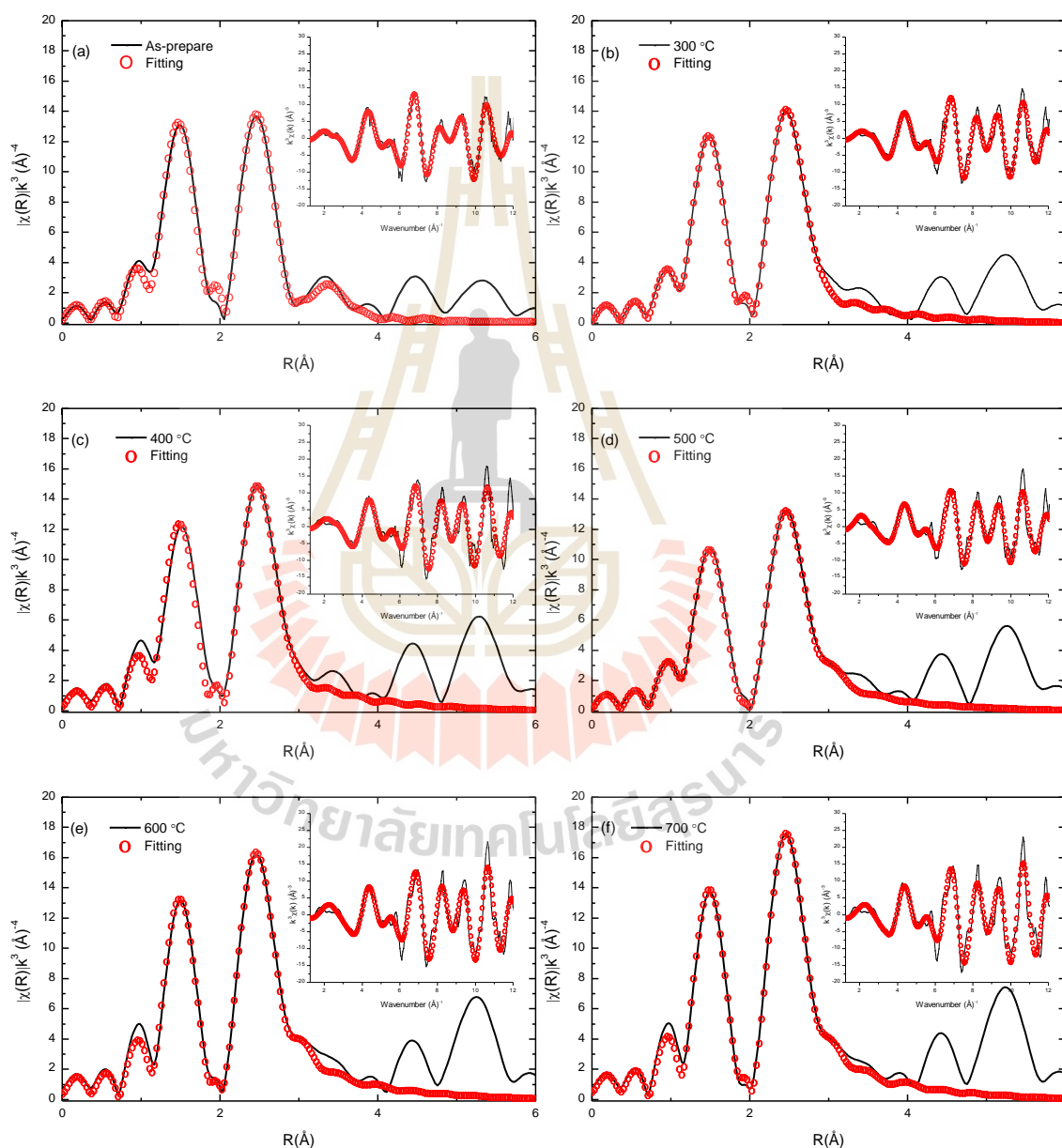


**Figure 4.3** Fourier transform EXAFS spectra at the Co K-edge and k-space(insets) of the  $\text{LiCoO}_2$  powders annealed at different temperatures for 10 h.

This trend was also observed in previous reports (Chen et al., 2007; Rana et al., 2014). The information of structural parameters, namely, number of neighboring atoms (N), interatomic distances (R), and Debye-Waller factors ( $\sigma^2$ ) refined from the EXAFS spectra using Athena and Artemis programs (B. Ravel and M. Newville, 2005), were showed in Table 4.2. The EXAFS refinement revealed that the Co–Co atomic distances of the annealed LiCoO<sub>2</sub> powders were not significantly different, meanwhile the Co–O atomic distances slightly increased when the annealing temperature increased suggesting the slight changes to the CoO<sub>6</sub> octahedra. The Co–O atomic distances of the LiCoO<sub>2</sub> were close to those previously reported (Ekwongsa et al., 2020).

**Table 4.2** Summary of EXAFS fitting parameters including interatomic distances (R), coordination numbers (N) and Debye–Waller factors ( $\sigma^2$ ).

| Sample      | Shell | N | $\sigma^2$ | R(Å)    |
|-------------|-------|---|------------|---------|
| As-prepared | Co-O  | 6 | 0.00125    | 1.89456 |
| 300°C       | Co-O  | 6 | 0.00199    | 1.89587 |
| 400°C       | Co-O  | 6 | 0.00205    | 1.90882 |
| 500°C       | Co-O  | 6 | 0.00318    | 1.90964 |
| 600°C       | Co-O  | 6 | 0.00372    | 1.91098 |
| 700°C       | Co-O  | 6 | 0.00309    | 1.91165 |
| As-prepared | Co-Co | 6 | 0.00371    | 2.83149 |
| 300°C       | Co-Co | 6 | 0.00314    | 2.81754 |
| 400°C       | Co-Co | 6 | 0.00266    | 2.82097 |
| 500°C       | Co-Co | 6 | 0.00324    | 2.82019 |
| 600°C       | Co-Co | 6 | 0.00343    | 2.81385 |
| 700°C       | Co-Co | 6 | 0.00277    | 2.81195 |

### 4.1.3 Raman

The Raman spectra of the  $\text{LiCoO}_2$  powders annealed at different temperatures before washing with deionized water were shown in Figure 4.4 (a). The Raman results also showed a clear phase formation when the annealing temperature increased. Firstly, the  $\text{LiCoO}_2$  precursor presented an amorphous structure. When the  $\text{LiCoO}_2$  powder was annealed at  $300\text{ }^\circ\text{C}$ , the Raman peaks of  $\text{LiCoO}_2$  feature were initially observed. The observed major peaks at  $484$  and  $595\text{ cm}^{-1}$  are attributed to  $E_g$  and  $A_{1g}$  mode, respectively. The  $E_g$  mode corresponds to the O–Co–O bending and the  $A_{1g}$  mode corresponds to the Co–O stretching (Hara et al., 2017; Jo et al., 2009; Matsuda et al., 2019). These Raman characteristics confirmed the HT- $\text{LiCoO}_2$  phase in the samples annealed at  $300\text{ }^\circ\text{C}$  which was also consistent with the XRD results. However, a small peak at  $715\text{ cm}^{-1}$  was observed in every sample which could be represented to the residual phase of  $\text{KNO}_3$  from the synthesis process (Acosta-Maeda et al., 2016). Therefore, we conducted the  $\text{KNO}_3$  elimination by washing with deionized water and the Raman measurement again after washing. The Raman spectra of washed powder were shown in Figure 4.4 (b). The small peak of  $\text{KNO}_3$  could not be detected in all samples. Meanwhile, the two main peaks of HT- $\text{LiCoO}_2$  phase shifted to the lower wavenumber from  $484$  to  $465\text{ cm}^{-1}$  and  $597$  to  $575\text{ cm}^{-1}$  for  $E_g$  and  $A_{1g}$  modes, respectively. Interestingly, the large peaks possessed to  $\text{Co}_3\text{O}_4$  structure at  $506$  and  $663\text{ cm}^{-1}$  were observed. This discovery seemed to be consistent with Le Van-Jodin, et al. (Le Van-Jodin et al., 2019). They studied Raman spectrum of HT- $\text{LiCoO}_2$  during the first charge/discharge cycle and found the HT- $\text{Li}_x\text{CoO}_2$  phase shifting from  $487$  to  $468\text{ cm}^{-1}$  and  $597$  to  $575\text{ cm}^{-1}$  for  $E_g$  and  $A_{1g}$  modes, respectively. They explained the Raman shifts occurrence in term of the de-intercalation of  $\text{Li}^+$  ions and reconstruction of the atoms in the hexagonal structure to the monoclinic and  $\text{Co}_3\text{O}_4$  phase. Even though, the  $\text{Co}_3\text{O}_4$  phase was not detected by the XRD in our study in every sample after washing with deionized water it was clearly seen by the Raman spectra. Meanwhile, the XANES spectra of annealed samples at  $600$  and  $700\text{ }^\circ\text{C}$  were not significantly different, however, these results contradicted with the Raman results, which the differences could be seen between the annealed samples at  $600$  and  $700\text{ }^\circ\text{C}$ . This result disagreement is plausible because Raman spectroscopy possesses higher surface

sensitivity than XRD and XANES techniques. The surface composition changes could be disclosed via Raman spectroscopy. Hence, the de-intercalation of  $\text{Li}^+$  ions, especially, on the surface of  $\text{LiCoO}_2$  particles due to the washing processes could be distinguished by surface investigation technique such as Raman spectroscopy.

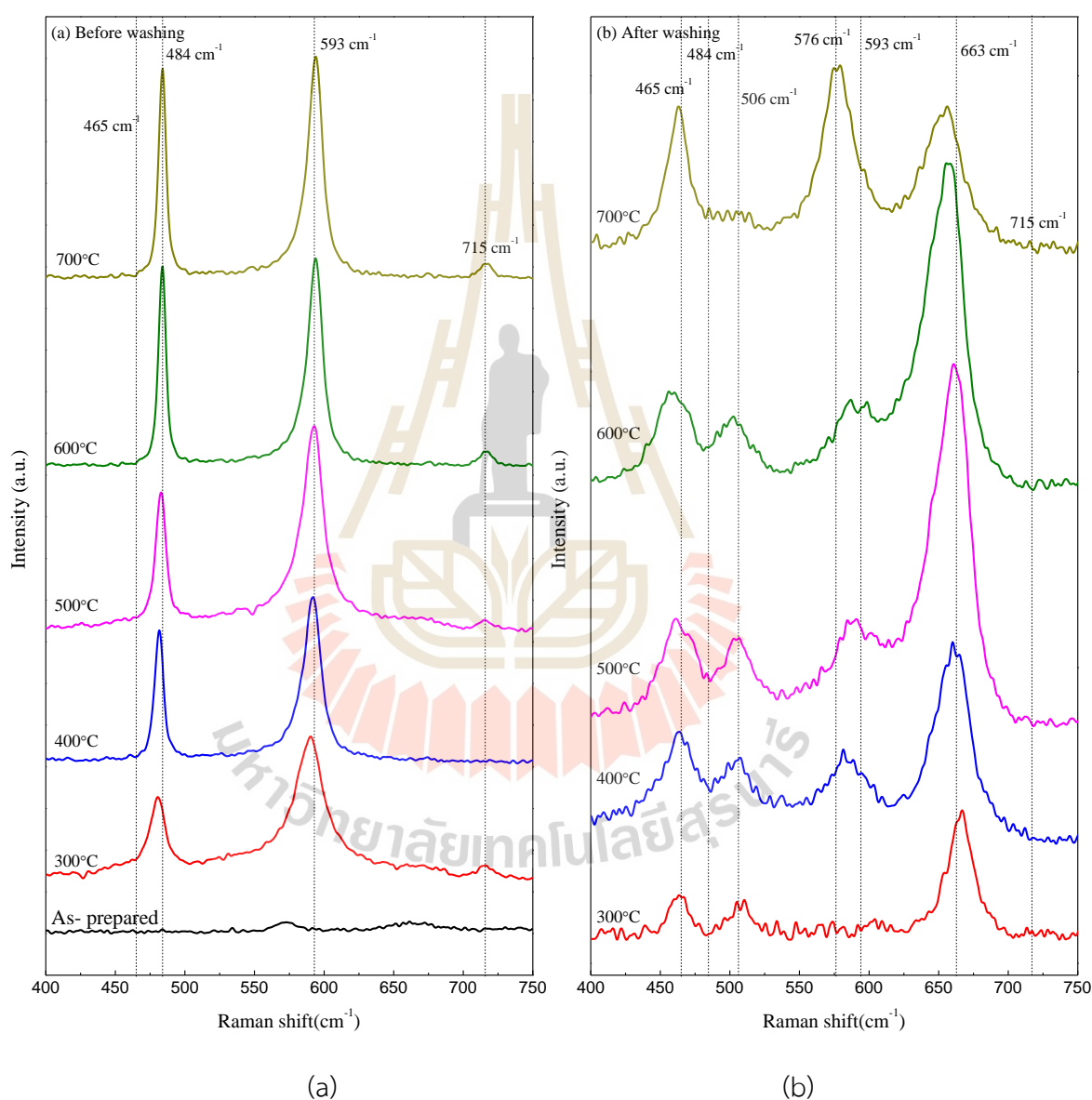


**Figure 4.4** Raman spectra of  $\text{LiCoO}_2$  powders annealed at different temperatures (a) before washing and (b) after washing with deionized water.

#### 4.1.4 XPS

The surface chemical compositions of the prepared  $\text{LiCoO}_2$  powders were also investigated by XPS. Wide scan XPS spectra of the  $\text{LiCoO}_2$  annealed at different temperatures are shown in Figure 4.5. The survey spectra clearly indicate the existence of carbon (C), oxygen (O), cobalt (Co), potassium (K), and nitrogen (N) elements on the sample surface of all  $\text{LiCoO}_2$  powders before washing with DI water. The chemical residues of K and N, which occur from the synthesis process, specifically  $\text{KNO}_3$ , were represented in the samples. However, these residues were eliminated in all  $\text{LiCoO}_2$  samples following the washing process. It is note that the Li peak was not clearly observed in all the wide scan spectra due to its low signal in the low-resolution scan.

The relative atomic concentrations estimated from the XPS spectra are shown in Table 4.3. Before washing, the samples exhibited distinct variations in the atomic concentrations of C, Li, O, Co, K, and N, thereby offering valuable insights into the complex thermodynamic behavior and elemental interactions within the  $\text{LiCoO}_2$ . The washing process, significant changes were observed in the atomic composition, indicating the successful elimination or reduction of impurities, particularly potassium (K) and nitrogen (N), which were introduced during the synthesis process. These findings demonstrate the effectiveness of the washing process in refining the atomic composition of  $\text{LiCoO}_2$  and achieving a higher level of material purity. Due to the contamination of C and O, the effects of temperature and the washing process on the chemical composition of  $\text{LiCoO}_2$  will be discussed later, specifically in relation to the Li/Co ratio.

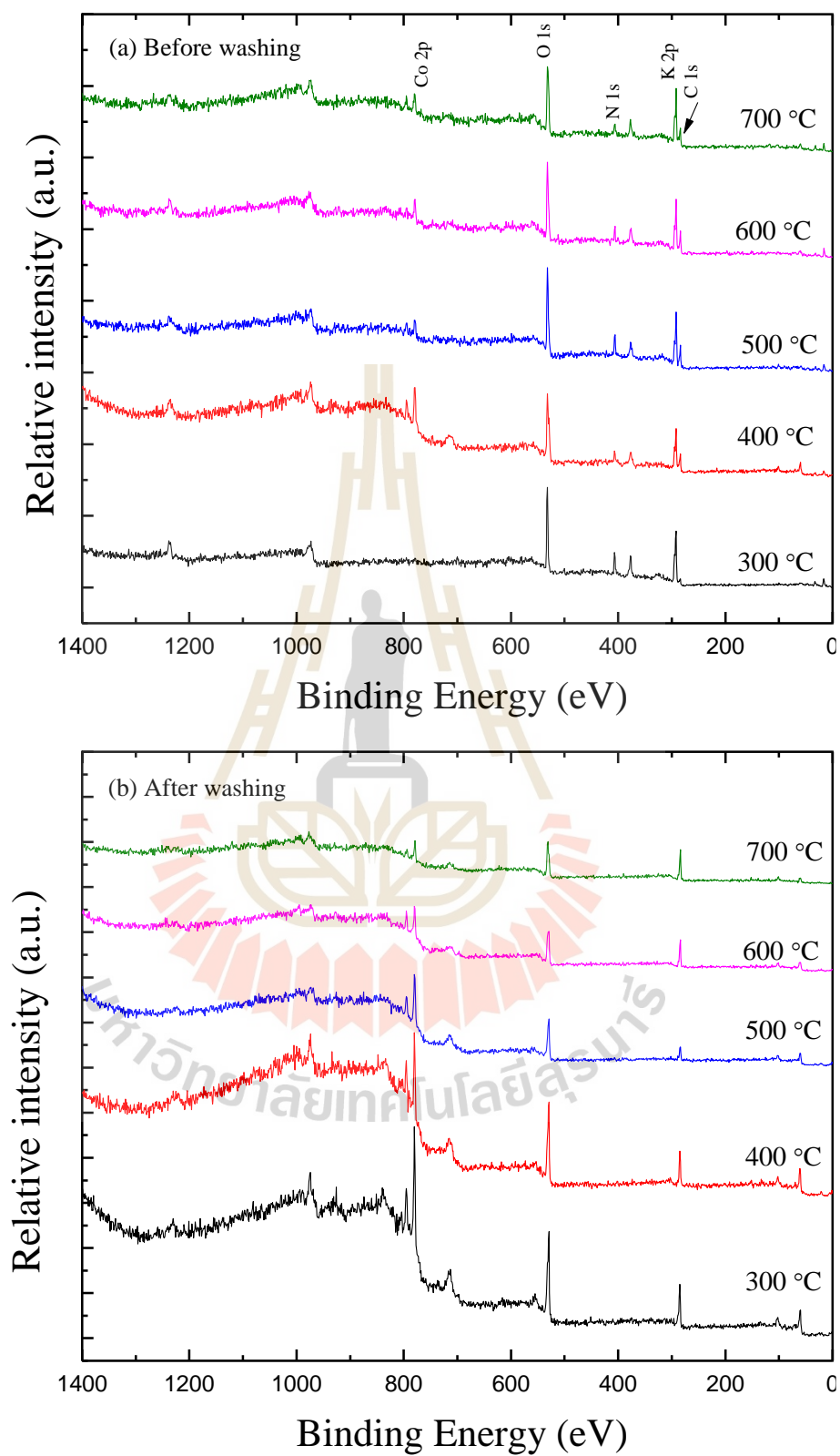
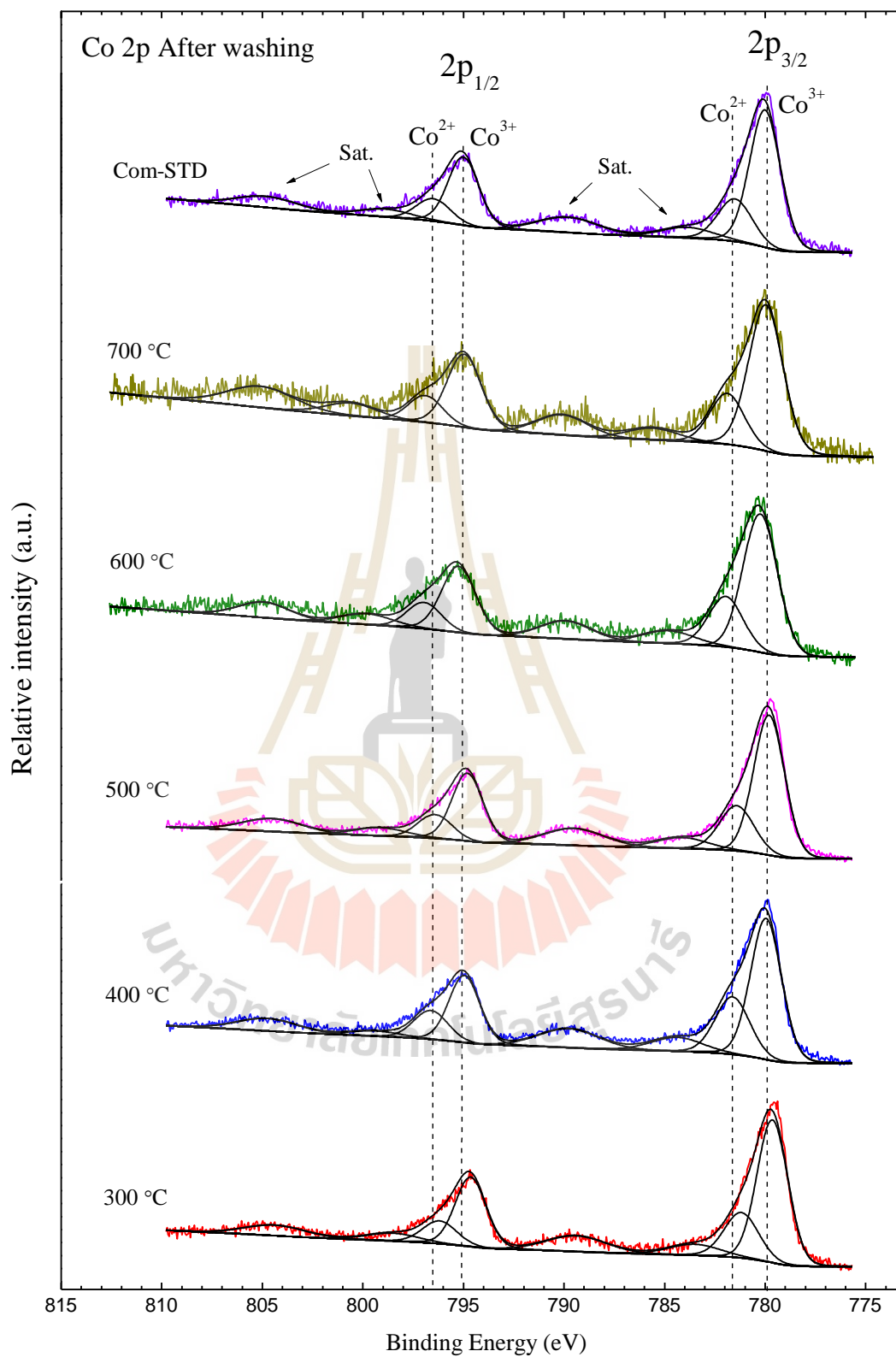


Figure 4.5 Wide scan XPS spectra of the  $\text{LiCoO}_2$  annealed at different temperatures (a) before washing (b) after washing with DI water.

**Table 4.3** The relative atomic concentrations of different elements in LiCoO<sub>2</sub> samples.

|                | Sample | C (%) | Li (%) | O (%) | Co (%) | K (%) | N (%) |
|----------------|--------|-------|--------|-------|--------|-------|-------|
| Before washing | 300 °C | 14.48 | 6.9    | 44.75 | 7.5    | 16.26 | 10.11 |
|                | 400 °C | 18.39 | 7.86   | 48.33 | 8.64   | 10.59 | 6.19  |
|                | 500 °C | 23.14 | 3.34   | 46.28 | 3.44   | 13.71 | 10.09 |
|                | 600 °C | 21.93 | 4.15   | 47.57 | 4.06   | 13.66 | 8.63  |
|                | 700 °C | 26.46 | 3.82   | 47.24 | 3.67   | 12.69 | 6.12  |
| After washing  | 300 °C | 41.63 | 7.22   | 39.69 | 11.46  | 0     | 0     |
|                | 400 °C | 21.49 | 12.63  | 45.51 | 20.37  | 0     | 0     |
|                | 500 °C | 32    | 8.57   | 45.6  | 13.83  | 0     | 0     |
|                | 600 °C | 46.89 | 5.07   | 39.87 | 8.17   | 0     | 0     |
|                | 700 °C | 52.63 | 4.34   | 37.74 | 5.29   | 0     | 0     |

High resolution XPS spectra of Co 2p peaks of the LiCoO<sub>2</sub> annealed at different temperatures after washing with deionized water were shown in Figure 4.6. The Co 2p core level XPS peaks exhibited two main peaks due to spin-orbit coupling (Co 2p<sub>3/2</sub> and Co 2p<sub>1/2</sub>), with the binding energy separation closed to 15 eV. The Co 2p<sub>3/2</sub> peaks of all spectra can be deconvoluted into two peaks at the binding energies of 779.64-780.24 eV and 781.19-781.96 eV which were attributed to Co<sup>3+</sup> and Co<sup>2+</sup>, respectively (Dah'eron et al., 2009). The summary of chemical compositions and peak positions of Co from the prepared LiCoO<sub>2</sub> powders were shown in Table 4.4. The atomic contents of Co<sup>3+</sup> and Co<sup>2+</sup> of the LiCoO<sub>2</sub> powders annealed at different temperatures were not significantly variant.



**Figure 4.6** High resolution XPS spectra of Co 2p of the  $\text{LiCoO}_2$  annealed at different temperatures for 10 h.

**Table 4.4** Summary of chemical compositions and oxidation states of Co from the LiCoO<sub>2</sub> powders annealed at different temperatures as estimated by XPS.

| Parameter                  | Annealed temperature |        |        |        |        |        | Com-<br>STD |      |
|----------------------------|----------------------|--------|--------|--------|--------|--------|-------------|------|
|                            | STD                  | 300 °C | 400 °C | 500 °C | 600 °C | 700 °C |             |      |
| Peak Position (eV)         |                      |        |        |        |        |        |             |      |
| Co <sup>3+</sup>           | 780.12               | 779.64 | 79.96  | 779.8  | 780.24 | 779.97 | 780.01      |      |
|                            | 795.11               | 794.64 | 94.96  | 794.8  | 795.24 | 794.97 | 795.01      |      |
| Co <sup>2+</sup>           | 782.24               | 781.19 | 81.63  | 781.42 | 781.96 | 781.89 | 781.51      |      |
|                            | 797.26               | 796.19 | 96.63  | 796.42 | 796.96 | 796.89 | 796.51      |      |
| Peak Area                  |                      |        |        |        |        |        |             |      |
| Co <sup>3+</sup>           | 2p <sub>3/2</sub>    | 14351  | 10742  | 2862   | 14496  | 2939   | 1734        | 8380 |
|                            | 2p <sub>1/2</sub>    | 7207   | 5371   | 174    | 7248   | 1469   | 867         | 4190 |
| Co <sup>2+</sup>           | 2p <sub>3/2</sub>    | 7176   | 3900   | 884    | 5363   | 1122   | 606         | 2901 |
|                            | 2p <sub>1/2</sub>    | 3604   | 1950   | 824    | 2682   | 561    | 303         | 1450 |
| Relative atomic percentage |                      |        |        |        |        |        |             |      |
| Co <sup>3+</sup> (%)       | 66.67                | 73.36  | 68.61  | 72.99  | 72.37  | 74.10  | 74.28       |      |
| Co <sup>2+</sup> (%)       | 33.33                | 26.64  | 31.39  | 27.01  | 27.63  | 25.90  | 25.72       |      |
| Chi Squared                | 1.83                 | 1.95   | 2.19   | 2.18   | 1.64   | 1.35   | 1.38        |      |

High resolution XPS spectra of Li 1s peaks of the LiCoO<sub>2</sub> powders annealed at different temperatures before washing and after washing with deionized water were shown in Figure 4.7. The Li 1s core level peaks of all spectra were observed at the

binding energy of 54.0 eV, approximately, indicating the presence of  $\text{Li}^{1+}$  (N. Andreu et al.,2015). The atomic ratio of Li and Co (Li/Co) was calculated by the following equation:

$$\text{Li/Co} = \frac{I_{\text{Li}1s}/S_{\text{Li}1s}}{I_{\text{Co}2p_{3/2}}/S_{\text{Co}2p_{3/2}}} \quad (4.1)$$

where,  $I_{\text{Li}1s}$  and  $I_{\text{Co}2p_{3/2}}$  are integrated areas under Li 1s and Co 2p<sub>3/2</sub> peaks, respectively.  $S_{\text{Li}1s}$  and  $S_{\text{Co}2p_{3/2}}$  are sensitivity factors of Li 1s and Co 2p<sub>3/2</sub> peaks, respectively. The results were shown in Table 4.5. Before the washing process the Li/Co ratio increased when the annealing temperature increased. The Li/Co ratio of the  $\text{LiCoO}_2$  powders annealed at 700 °C was 1.02 which was close to the perfect chemical composition of  $\text{LiCoO}_2$ , Li/Co ratio is equal 1. This result was consistent with the results obtained from XRD, XAS and Raman techniques.

After washing with deionized water, the Li/Co ratio significantly decreased to the range of 0.62-0.82. The  $\text{LiCoO}_2$  annealed at 700 °C displayed the highest Li/Co ratio of 0.82. This result indicated the loss of  $\text{Li}^+$  ions during washing with deionized water. The XPS results supported the assumption that the washing process could affect the de-intercalation of  $\text{Li}^+$  ions on the surface of  $\text{LiCoO}_2$  particles.

**Table 4.5** Li/Co ratio of the  $\text{LiCoO}_2$  powders annealed at different temperatures before washing and after washing with deionized water.

| Sample | Li/Co ratio    |               |
|--------|----------------|---------------|
|        | Before washing | After washing |
| 300    | 0.92           | 0.63          |
| 400    | 0.91           | 0.62          |
| 500    | 0.97           | 0.62          |
| 600    | 1.02           | 0.62          |
| 700    | 1.04           | 0.82          |

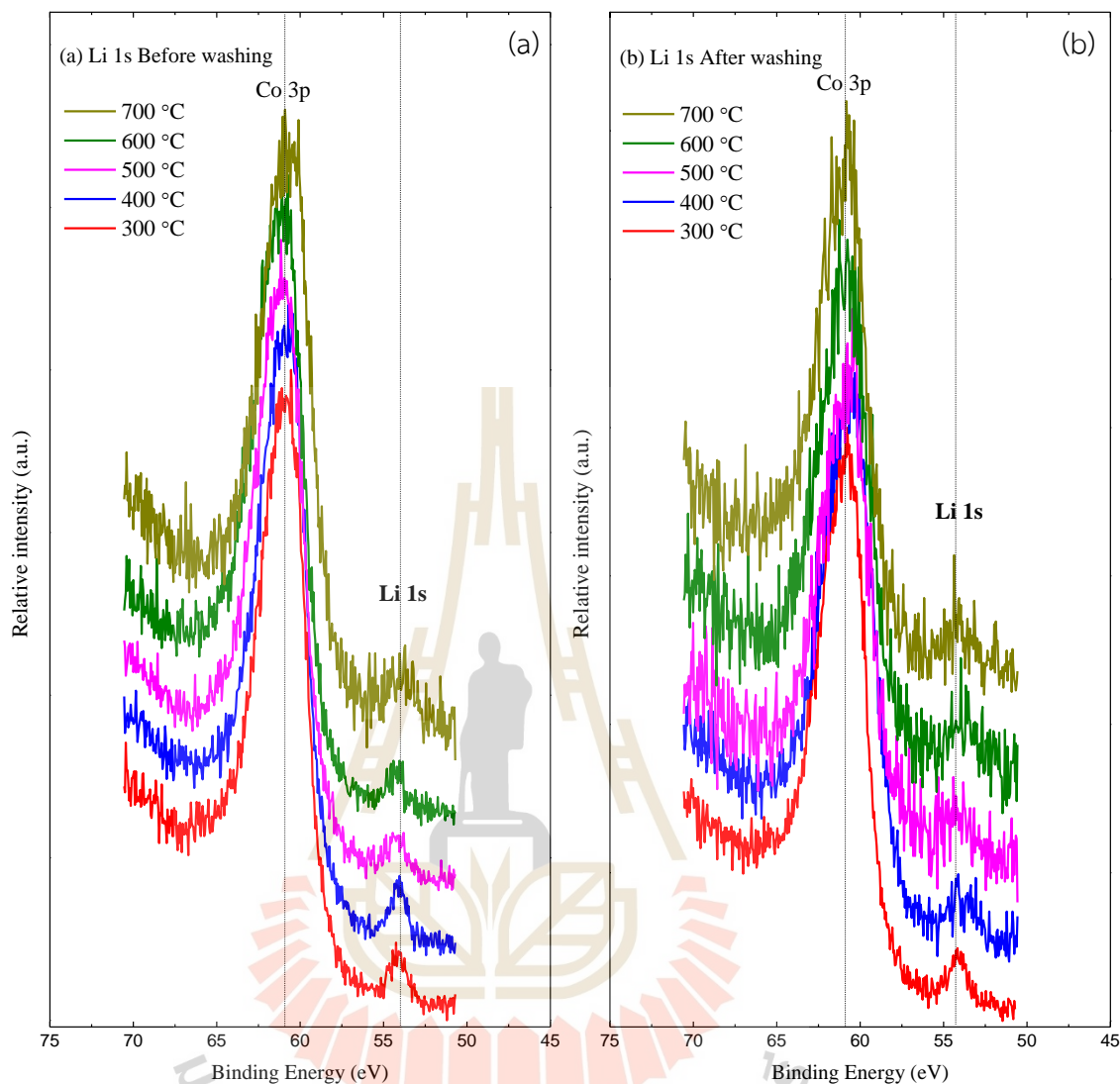


**Figure 4.7** XPS spectra Li 1s of LiCoO<sub>2</sub> samples at different temperatures (a) before washing and (b) after washing with deionized water.

#### 4.1.5 SEM

The morphologies of the LiCoO<sub>2</sub> powders annealed at different temperatures were illustrated in Figure 4.8. The FE-SEM images showed the morphology evolution to the hexagonal shape particles with the increasing annealing temperature. The increase of particle size when the annealing temperature increased were in agreement with the increase of crystallite size obtained from the Syn-XRD results. The hexagonal nanoparticles, with the irregular mixture between hexagonal

structure and hexagonal flakelike structure, were clearly observed in  $\text{LiCoO}_2$  powders annealed at 600 and 700 °C. (Choi et al., 2006; Sheu et al., 1997).

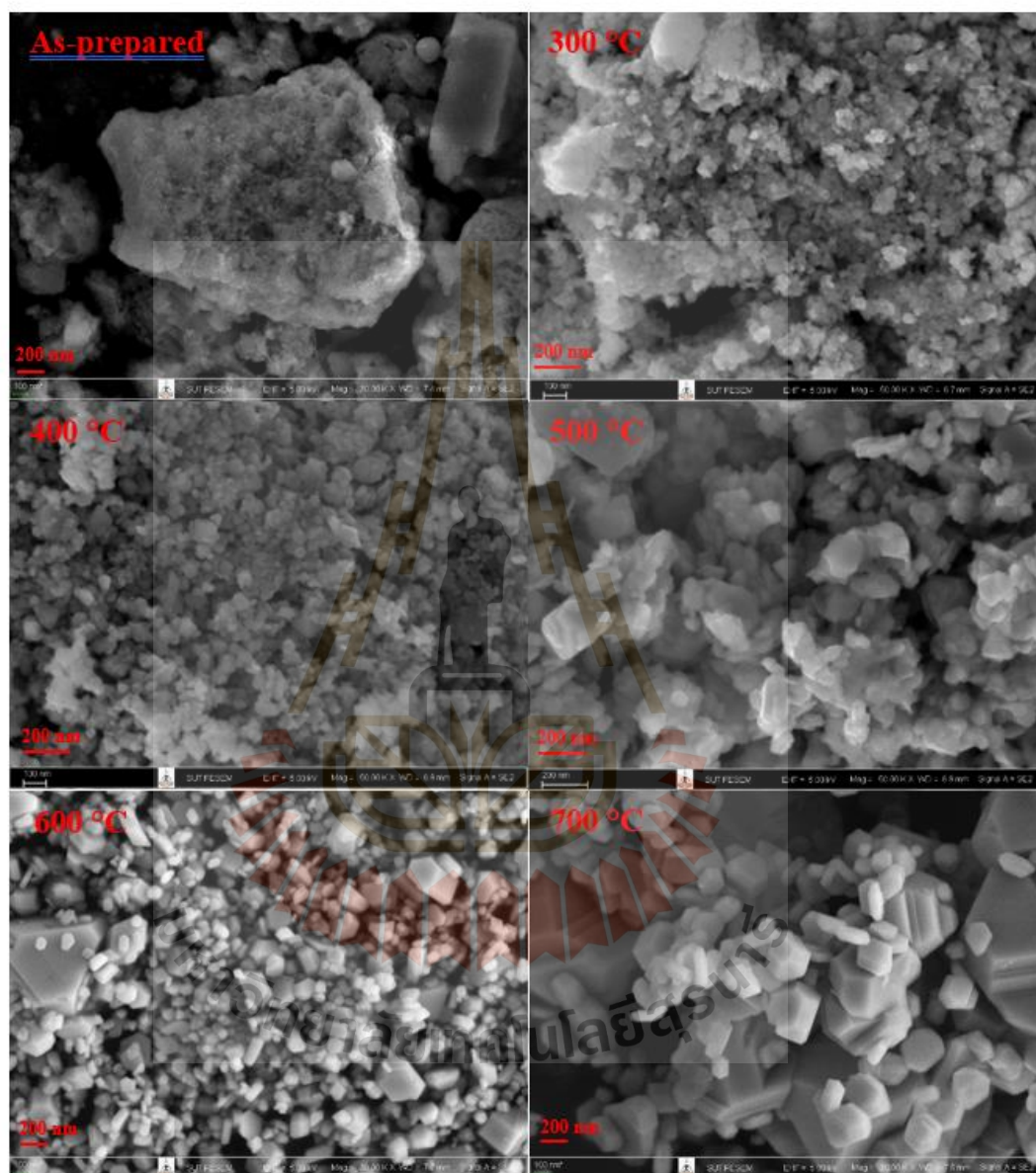


Figure 4.8 FE-SEM images of the  $\text{LiCoO}_2$  powders annealed at different temperatures for 10h.

## 4.2 INFLUENCE OF ANNEALING AMBIENT ON THE STRUCTURE OF LiCoO<sub>2</sub>

In this section, the influence of annealing ambient on the structure of the LiCoO<sub>2</sub> powder was preliminary studied. The LiCoO<sub>2</sub> powder was thermally annealed under the flow of N<sub>2</sub> and the mixture of O<sub>2</sub> and N<sub>2</sub>.

### 4.2.1 XRD

The XRD patterns of the LiCoO<sub>2</sub> powders annealed under the flow of N<sub>2</sub> (100 sccm) and the mixture of O<sub>2</sub> and N<sub>2</sub> (20 and 80 sccm, respectively) at different temperatures are shown in Figure 4.9. All patterns can be indexed to the standard pattern of LiCoO<sub>2</sub> (mp-24850). The second phases of KNO<sub>3</sub> were also detected. The (0 0 6)/(1 0 2) and (1 0 8)/(1 1 0) peaks showed splitting doublets at around 37° and 67°, respectively. These doublets became distinguishable at annealing temperatures of 600 °C, indicating the presence of the HT-LiCoO<sub>2</sub> phase in both the N<sub>2</sub> and O<sub>2</sub>/N<sub>2</sub> mixture samples. This observation is in good agreement with Chen, et al. and Akimoto, et al., (Akimoto et al., 1998; Chen et al., 2002).

All diffraction patterns also exhibited a very strong (003) peak and comparatively weak (104) peak, which indicate a preferred c-axis orientation. The intensity ratios of the (003) peak to the (104) peak ( $I_{003}/I_{104}$ ), which could be used as an indication of c-axis orientation, are shown in Table 4.6.

**Table 4.6** The intensity ratios of the (003) peak to the (104) peak ( $I_{003}/I_{104}$ ).

| Sample | N <sub>2</sub> -80sccm+ | N <sub>2</sub> -100sccm |
|--------|-------------------------|-------------------------|
|        | O <sub>2</sub> -20sccm  |                         |
|        | $I_{003}/I_{104}$       |                         |
| 700 °C | 1.708102                | 2.30544                 |
| 600 °C | 1.898937                | 2.259749                |
| 500 °C | 1.860862                | 2.250141                |
| 400 °C | 1.766519                | 1.995834                |

Table 4.6 shows that  $\text{LiCoO}_2$  prepared under the flow of  $\text{N}_2$  (100 sccm) had higher  $I_{003}/I_{104}$  values than that under the flow of  $\text{O}_2$  (20 sccm) and  $\text{N}_2$  (80 sccm) mixture. It suggests that  $\text{LiCoO}_2$  prepared in pure  $\text{N}_2$  flow exhibited higher degree of the c-axis orientation.

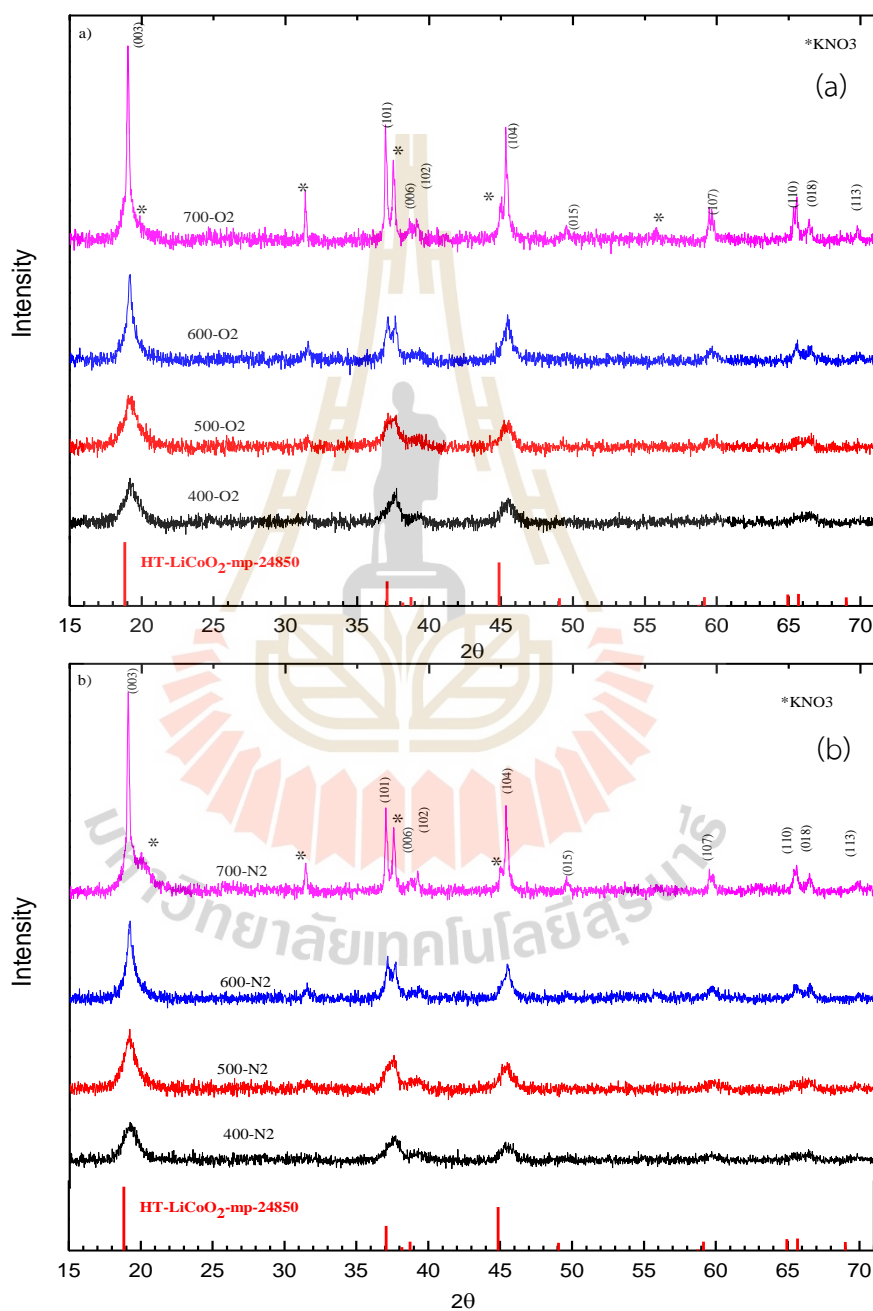


**Figure 4.9** XRD patterns of the prepared  $\text{LiCoO}_2$  powders annealed at different temperatures for 10h (a) under the flow of  $\text{O}_2$  (20 sccm) and  $\text{N}_2$  (80 sccm) mixture and (b)  $\text{N}_2$  (100 sccm).

The observed broadening of diffraction peaks was due to the crystallite size effect. The crystallite size of those annealed samples were calculated using Rietveld refinement, as listed in Table 4.7. The average crystallite sizes obtained from the annealed samples with a flow mixture of O<sub>2</sub> and N<sub>2</sub> at temperatures of 400, 500, 600, and 700 °C were 19.1 ± 2.5 nm, 20.7 ± 3.1 nm, 31.9 ± 0.8 nm, and 85.7 ± 6.3 nm, respectively. It was clearly seen that the crystallite size tended to increase with the increase of the annealing temperature. On the other hand, for samples with a flow of N<sub>2</sub>, there was a slight increase in the crystallite size across the entire temperature range. The crystallite sizes were 19.3 ± 2.6 nm, 21.7 ± 2.4 nm, 33.9 ± 1.5 nm, and 89.9 ± 4.6 nm at temperatures of 400, 500, 600, and 700 °C, respectively.

**Table 4.7** The crystallite sizes of the LiCoO<sub>2</sub> powders annealed at different temperatures for 10 h under the flow of O<sub>2</sub> (20 sccm) and N<sub>2</sub> (80 sccm) mixture and N<sub>2</sub> (100 sccm).

| Sample | N <sub>2</sub> + O <sub>2</sub> | N <sub>2</sub> |
|--------|---------------------------------|----------------|
| 700 °C | 85.7±6.3 nm                     | 89.9±4.6 nm    |
| 600 °C | 31.9±0.8 nm                     | 33.9±1.5 nm    |
| 500 °C | 20.7±3.1 nm                     | 21.7±2.4 nm    |
| 400 °C | 19.1±2.5 nm                     | 19.3±2.6 nm    |

## 4.2.2 SEM

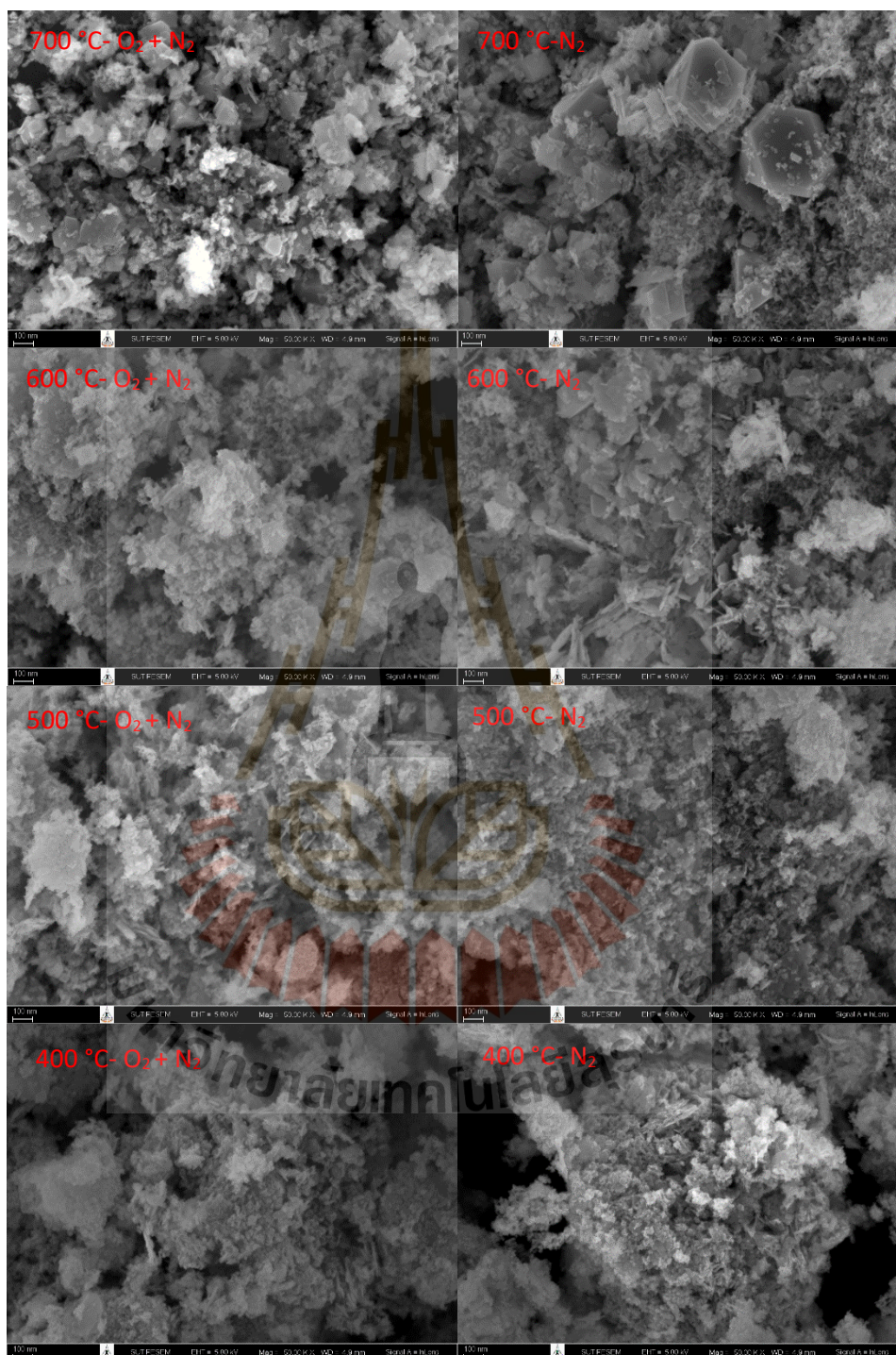
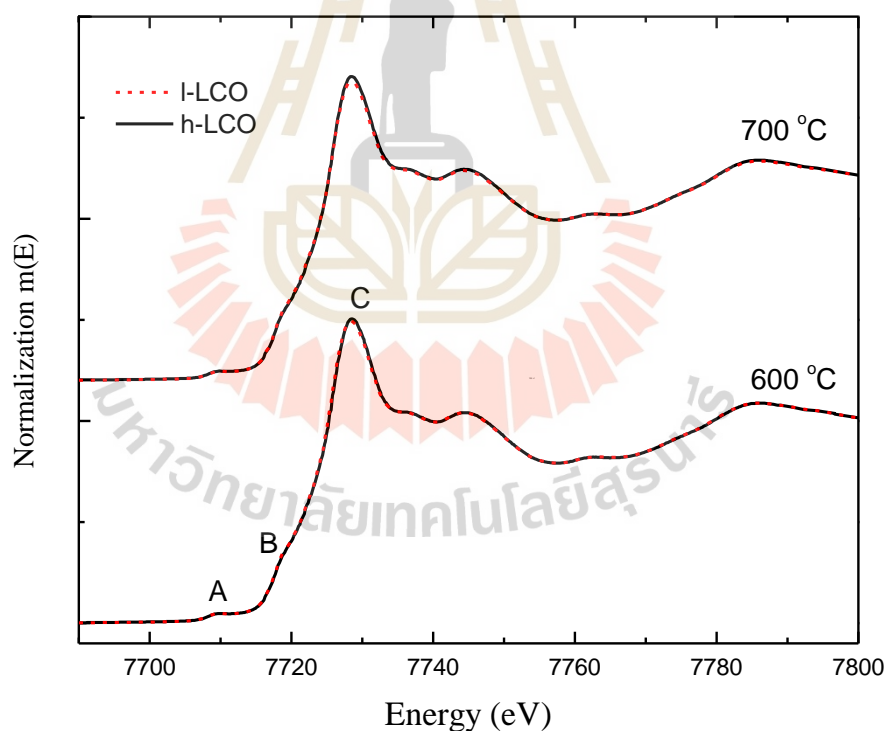


Figure 4.10 FE-SEM images of the  $\text{LiCoO}_2$  powders annealed at different temperatures for 10h under the flow of  $\text{O}_2$  (20 sccm) and  $\text{N}_2$  (80 sccm) mixture and  $\text{N}_2$  (100 sccm).

The FE-SEM images of the  $\text{LiCoO}_2$  powders annealed under the flow of  $\text{N}_2$  and mixture of  $\text{O}_2$  and  $\text{N}_2$  at different temperatures are shown in Figure 4.10. The FE-SEM images showed the morphology evolution to the hexagonal shape as the annealing temperature increased for both the  $\text{LiCoO}_2$  powders annealed under the flow of  $\text{N}_2$  and  $\text{O}_2$  and  $\text{N}_2$  mixture. The hexagonal nanoparticles, with the irregular mixture between hexagonal structure and hexagonal flakelike structure, were clearly observed at high annealing temperatures of 600 °C and 700 °C. The increase of particle size with the increasing annealing temperature was also observed. Moreover, the  $\text{LiCoO}_2$  annealed at 600 °C and 700 °C showed that the  $\text{LiCoO}_2$  powders annealed under the flow of  $\text{N}_2$  had a larger particle size than that annealed under the flow mixture of  $\text{O}_2$  and  $\text{N}_2$ .

#### 4.2.3 XAS



**Figure 4.11** XANES of Co K-edge of the  $\text{LiCoO}_2$  powders annealed under the flow mixture of  $\text{O}_2$  20 sccm and  $\text{N}_2$  80 sccm (l-LCO) and  $\text{N}_2$  100 sccm (h-LCO) at 600 °C and 700 °C.

The XANES spectra of the Co K-edge of  $\text{LiCoO}_2$  samples annealed in flow  $\text{O}_2$  and  $\text{N}_2$  mixture (l-LCO) and  $\text{N}_2$  (h-LCO) at 600 and 700 °C are shown in Figure 4.11. The pre-edge absorption peak A correspond to the transition from the electric dipole-prohibited 1s orbital to the unoccupied 3d orbital in  $\text{Co}^{3+}$ . The peaks B and C show the 1s to 4p transition with and without shakedown, respectively, which is caused by a charge transfer from the ligand to the metal. There is no difference observed in cobalt oxidation state, and cobalt is placed in octahedral sites, as there is no insignificant difference in peak C positions between the  $\text{LiCoO}_2$  powders annealed under the flow of  $\text{O}_2$  and  $\text{N}_2$  mixture, and  $\text{N}_2$  at 600 °C and 700 °C.

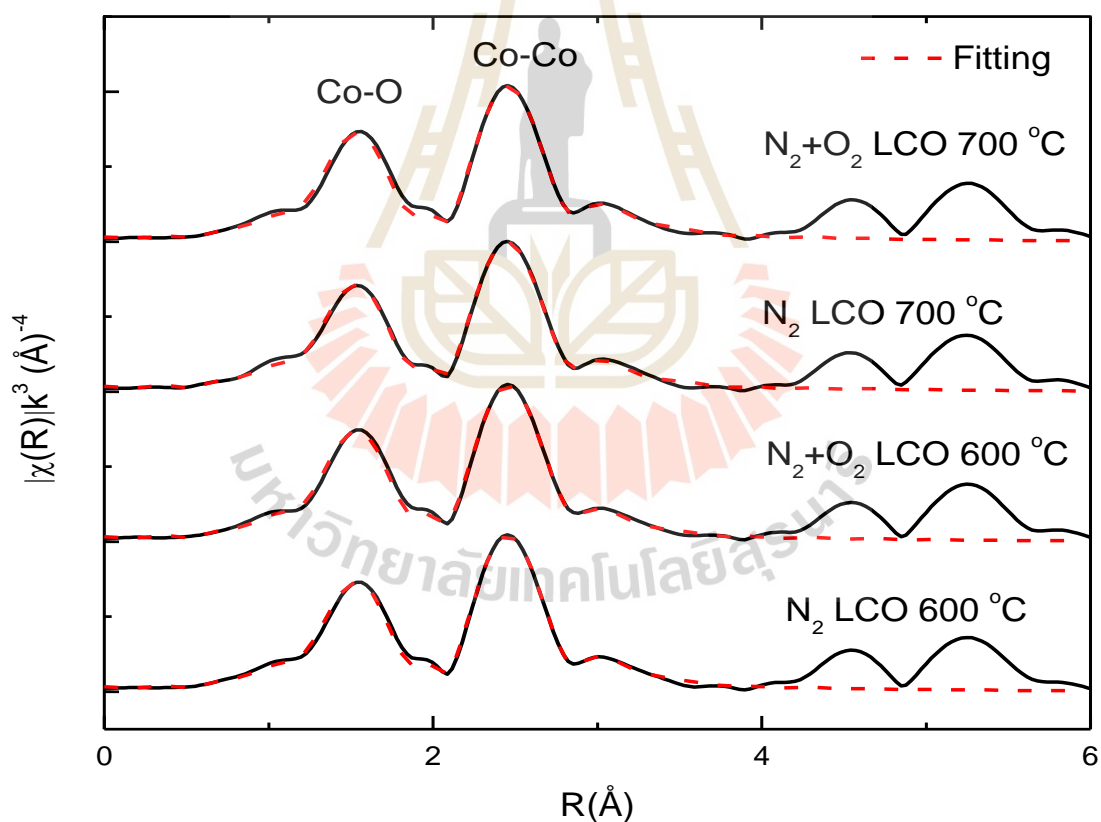


**Figure 4.12** Fourier transform EXAFS spectra of Co K-edge of the  $\text{LiCoO}_2$  powders annealed under the flow mixture of  $\text{O}_2$  20 sccm and  $\text{N}_2$  80 sccm and  $\text{N}_2$  100 sccm at 600 °C and 700 °C.

The Fourier transformations of Co K-edge k<sup>3</sup>-weighted EXAFS spectra of the LiCoO<sub>2</sub> powders annealed under the flow of O<sub>2</sub> and N<sub>2</sub> mixture and N<sub>2</sub> are shown in Figure 4.12. The Fourier transformations peaks at approximately 1.9 and 2.8 correspond to the single scattering contributions from the closest O and Co atoms, respectively. Compared to Cobalt, the contribution of the lithium coordination shell is hardly discernible owing to the Li atom's low scattering factor.

**Table 4.8** Summary of EXAFS fitting parameters including interatomic distances (R), coordination numbers (N) and Debye–Waller factors ( $\sigma^2$ ).

| Sample | Shell                          | N     | R(Å)    | $\sigma^2$ |
|--------|--------------------------------|-------|---------|------------|
| 600    | N <sub>2</sub> +O <sub>2</sub> | Co-O  | 1.90819 | 0.00244    |
|        |                                | Co-Co | 2.82367 | 0.00348    |
|        | N <sub>2</sub>                 | Co-O  | 1.90810 | 0.00217    |
|        |                                | Co-Co | 2.82202 | 0.00278    |
| 700    | N <sub>2</sub> +O <sub>2</sub> | Co-O  | 1.91127 | 0.00234    |
|        |                                | Co-Co | 2.82568 | 0.00394    |
|        | N <sub>2</sub>                 | Co-O  | 1.90805 | 0.00208    |
|        |                                | Co-Co | 2.82222 | 0.00275    |

Nonlinear least squares fitting was used to determine the structural characteristics of the first two coordination shells, including the interatomic distances R and Debye-Waller factors  $\sigma^2$  and the results are shown in Table 4.8. According to local disorder, the Debye-Waller factor  $\sigma^2$  represents the mean square relative atomic displacement of interatomic distance R for each bonding pair. It can be seen from the bondlength R of the Co-O and Co-Co shells in h-LCO are a slightly shorter than that of l-LCO. There might be some structural contraction in short-range order without significant changes in the R-3m structure (Chadwick et al., 2006). The Debye Waller factors of the LiCoO<sub>2</sub> powders annealed under the flow of O<sub>2</sub> and N<sub>2</sub> mixture are larger than that of N<sub>2</sub>. This result is consistent with the XRD results as the larger disorder in

LiCoO<sub>2</sub>, the lower degree of c-axis orientation (Maugeri et al., 2013). The h-LCO are considered to be intact and ordered, while they are distorted and fragmental in l-LCO. These differences in structure would possibly have significant impact on the electrochemical properties of LiCoO<sub>2</sub>, as a cathode material for Li-ion batteries (Gao et al., 2015).

### 4.3 STRUCTURAL STUDY OF LiCoO<sub>2</sub> THIN FILM PREPARED BY RF MAGNETRON SPUTTERING

In this section, the preliminary results on the structural study on the LiCoO<sub>2</sub> thin films prepared by RF magnetron sputtering technique were presented. The effect of the process gas on the structure of the films was investigated.

#### 4.3.1 Preliminary Results

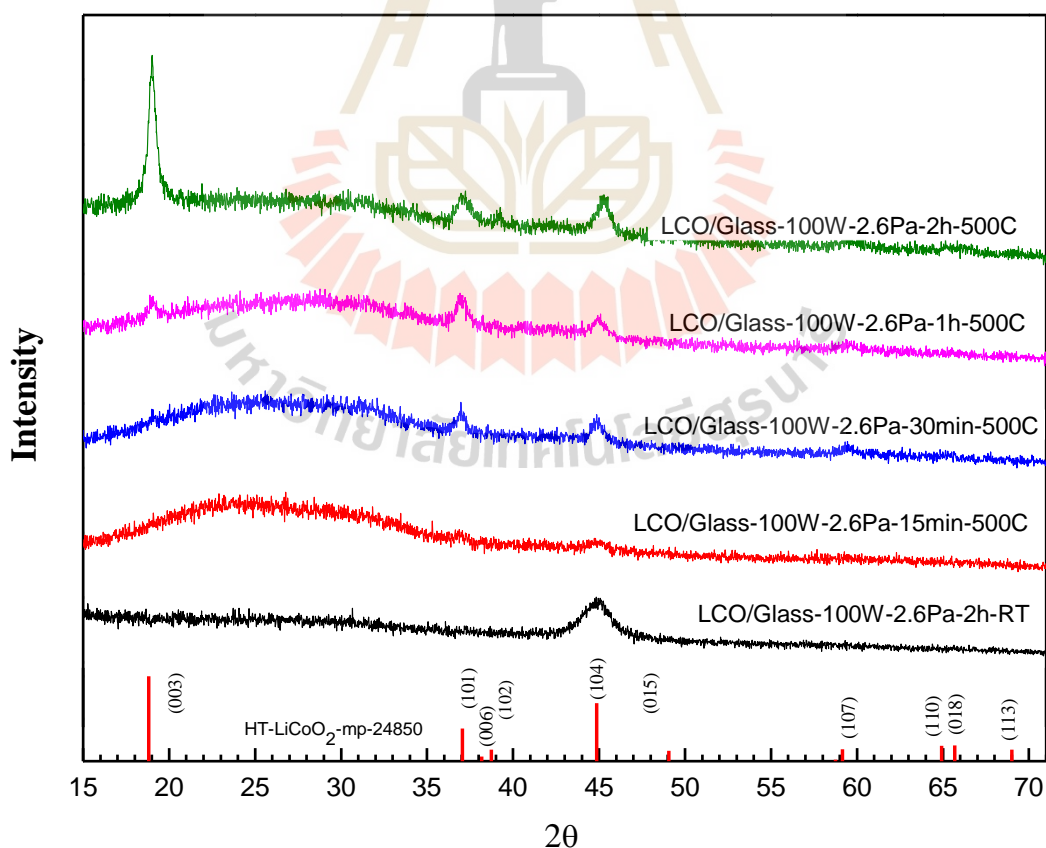
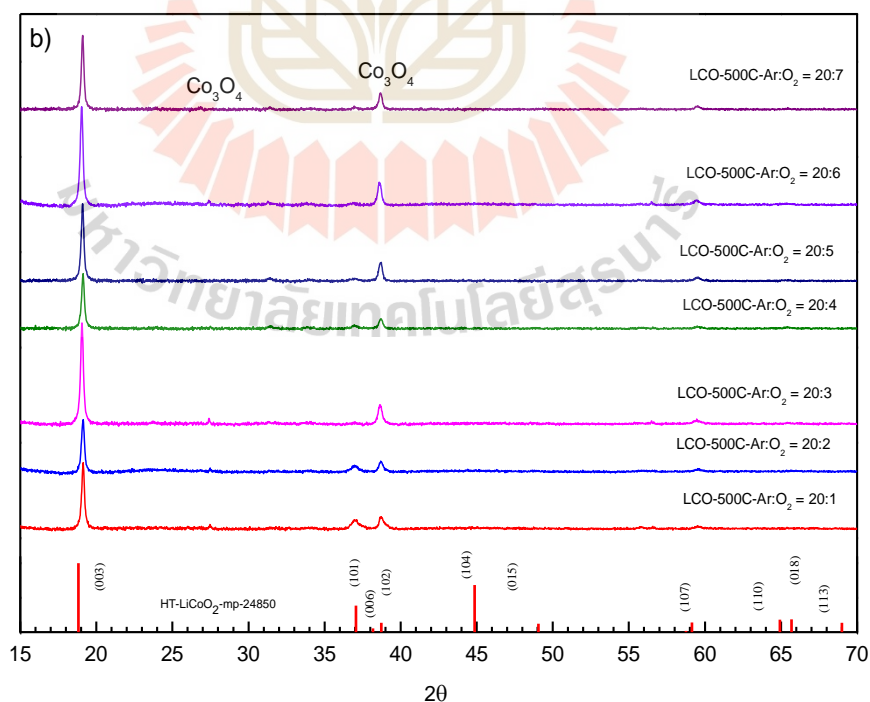


Figure 4.13 XRD patterns of the LiCoO<sub>2</sub> films deposited with different time.

The XRD patterns of the  $\text{LiCoO}_2$  films deposited with different deposition time are shown in Figure 4.13. The  $\text{LiCoO}_2$  films were deposited onto glass slide substrates by in an argon pressure of 2.6 Pa. The distance between the substrate and the target was 5 cm, and an RF power was fixed at 100 W during the deposition process. The XRD spectrum of the as-deposited  $\text{LiCoO}_2$  film with the deposition time of 2 h showed only the broad (104) diffraction peak suggesting that the crystal structure of the as-deposited film is not well-defined and has some disorder or strain. This observation is similar to the previous report by Bouwman et al. However, after annealing at 500 °C for 30 minutes, the (104) peak became sharpening indicating more ordered and crystalline the (003) diffraction peak, which corresponds to a specific crystal plane in  $\text{LiCoO}_2$ , retained the highest intensity even after annealing at 500°C for 2 h. This suggests that the annealing process significantly altered the preferential orientation of the film along the 003 plane. The (101) and (104) diffraction peaks, which are also specific crystal planes, were also observed after annealing. The impurity phase of  $\text{Co}_3\text{O}_4$ , which can be frequently found in  $\text{LiCoO}_2$  films was not present (Bouwman et al., 2001)



**Figure 4.14** XRD patterns of the  $\text{LiCoO}_2$  thin films deposited with different  $\text{O}_2$  flow rates.

The XRD patterns of the  $\text{LiCoO}_2$  films deposited with different  $\text{O}_2$  flow rates are shown in Figure 4.14. The XRD analysis indicates that the (003) plane is clearly preferred in all samples, indicating a tendency for the crystalline structure of  $\text{LiCoO}_2$  films to align with this particular plane. However, the intensity of the (104) plane gradually decreased and disappeared when the Ar:  $\text{O}_2$  ratio reached 20:3.

The normalized XANES spectra at the Co K-edge of the annealed  $\text{LiCoO}_2$  thin film, commercial standard  $\text{LiCoO}_2$  (LCO-STD) and  $\text{Co}_3\text{O}_4$  standard are shown in Figure 4.15. The shoulder feature at around 7720 eV and 7736 eV became disappear as  $\text{O}_2$  flow rate increased similar to  $\text{Co}_3\text{O}_4$  feature as seen the linear combination fitting in Table 4.9. The weight value of  $\text{LiCoO}_2$  thin films slightly increased with increasing  $\text{O}_2$  flow rate and is closest to STD at the  $\text{O}_2$  flow rate of 7 sccm. These confirm the growth of the peak at  $38.5^\circ$  of the XRD result.

**Table 4.9** The linear combination fitting of  $\text{LiCoO}_2$  thin films deposited with various concentration of  $\text{O}_2$  compare with  $\text{LiCoO}_2$  STD and STD.

| Data       | $\text{LiCoO}_2$ STD |          | STD      |          |
|------------|----------------------|----------|----------|----------|
|            | weight               | error    | weight   | error    |
| LCO-O0-N20 | 0.613177             | 0.016402 | 0.386823 | 0.025974 |
| LCO-O1-N20 | 0.41197              | 0.018568 | 0.58803  | 0.027393 |
| LCO-O2-N20 | 0.333788             | 0.018991 | 0.666212 | 0.027681 |
| LCO-O3-N20 | 0.333372             | 0.019722 | 0.666628 | 0.028188 |
| LCO-O4-N20 | 0.22495              | 0.019893 | 0.77505  | 0.028308 |
| LCO-O5-N20 | 0.170627             | 0.018777 | 0.829373 | 0.027535 |
| LCO-O6-N20 | 0.204533             | 0.019506 | 0.795467 | 0.028037 |
| LCO-O7-N20 | 0.158508             | 0.020008 | 0.841492 | 0.028389 |

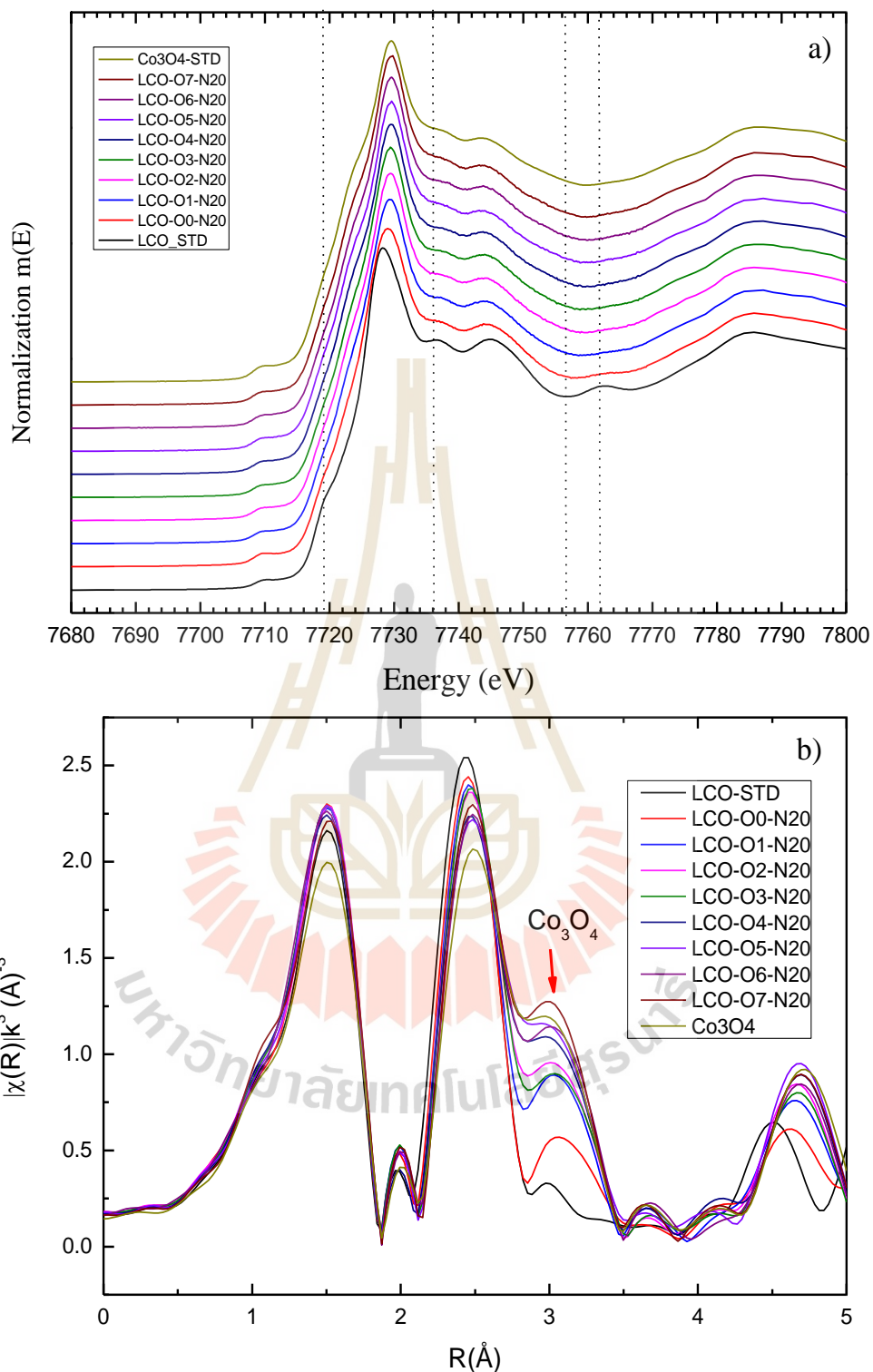
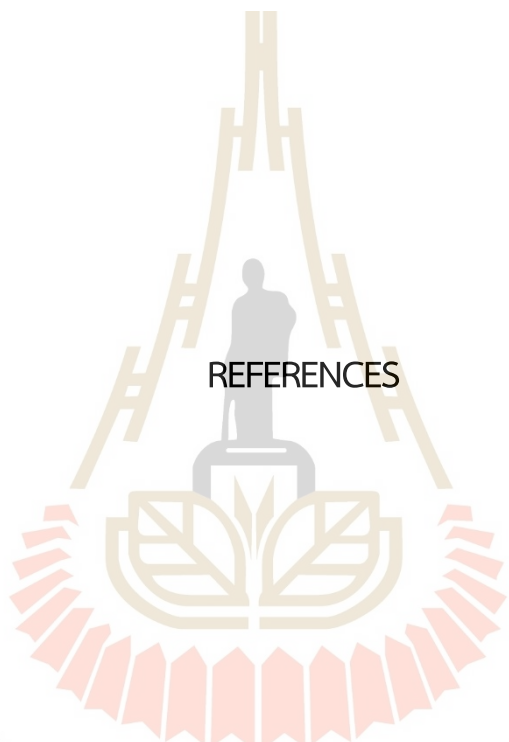


**Figure 4.15** XANES and Fourier transform EXAFS spectra of Co K-edge of the LiCoO<sub>2</sub> thin film was sputtered with 20 sccm of pure Ar and 1 to 7 sccm of different O<sub>2</sub> forms in an Ar/O<sub>2</sub> mixture.

## CHAPTER V

### CONCLUSION

In this study, the  $\text{LiCoO}_2$  powders were prepared by the co-precipitation method. The effect of annealing temperature and washing with deionized water on its properties were carried out by Syn-XRD, XAS, Raman spectroscopy, XPS and FE-SEM techniques. The results demonstrated the gradual phase evolution of  $\text{LiCoO}_2$  powders with the increasing annealing temperature. The formation of HT- $\text{LiCoO}_2$  structure was partly observed at 300 °C and it was complete at the minimum annealing temperature of 600 °C. The Raman spectroscopy and XPS results suggested that the washing process induced the de-intercalation of  $\text{Li}^+$  ions on only the surface of  $\text{LiCoO}_2$  particles. In addition, the influence of annealing ambient on the structure of  $\text{LiCoO}_2$  powders was investigated. It was observed that the  $\text{LiCoO}_2$  powders annealed under the flow of pure  $\text{N}_2$  yielded a higher degree of c-axis orientation in the structure and a larger particle size as compared to that annealed under  $\text{N}_2$  and  $\text{O}_2$ . These structural differences could potentially have a significant impact on the electrochemical properties of  $\text{LiCoO}_2$ , which is commonly used as a cathode material for Li-ion batteries.



REFERENCES

มหาวิทยาลัยเทคโนโลยีสุรนารี

## REFERENCES

- Acosta-Maeda, T. E., Misra, A. K., Muzangwa, L. G., Berlanga, G., Muchow, D., Porter, J., and Sharma, S. K. (2016). Remote Raman measurements of minerals, organics, and inorganics at 430 m range. *Applied Optics*, 55(36), 10283-10289.
- Adhikary, K., Takahashi, M., and Kikkawa, S. (1998). Some new aspects of low-temperature lithium cobalt oxides prepared through citric acid precursor route. *Mater. Res. Bull.*, 33, 1845.
- Akimoto, J., Gotoh, Y., and Oosawa, Y. (1998). Synthesis and structure refinement of LiCoO<sub>2</sub> Single crystals. In: Elsevier.
- Amine, K., Tukamoto, H., Yasuda, H., and Fujita, Y. (1996). A New Three-Volt Spinel Li<sub>1+x</sub>Mn<sub>1.5</sub>Ni<sub>0.5</sub>O<sub>4</sub> for Secondary Lithium Batteries. *Journal of The Electrochemical Society*, 143(5), 1607.
- Andreu, N., Flahaut, D., Dedryvère, R., Minvielle, M., Martinez, H., and Gonbeau, D. (2015). XPS investigation of surface reactivity of electrode materials: effect of the transition metal. *ACS applied materials & interfaces*, 7(12), 6629-6636.
- Ankoudinov, A. L. (1996). Relativistic spin-dependent X-ray absorption theory. PhD Thesis, University of Washington.
- Antolini, E. (2004). LiCoO<sub>2</sub>: formation, structure, lithium and oxygen nonstoichiometry, electrochemical behaviour and transport properties. *Solid state ionics*, 170, 159-171.
- Aravindan, V., Gnanaraj, J., Madhavi, S., and Liu, H. K. (2011). Lithium-ion conducting electrolyte salts for lithium batteries. *Chemistry–A European Journal*, 17(51), 14326-14346.
- Attwood, D., Thompson, A., Gullikson, E., Howells, M., Kim, K. J., Kirz, J., ... and Winick, H. (2001). X-ray data booklet. Lawrence Berkeley National Laboratory. *University of California, Berkeley, CA, 94720*.
- Balkanski, M. (2000). Solid-state microbatteries for electronics in the 21st century. *Sol. Energy Mater. Sol. Cells*, 62, 21.

- Béguin, F., and Frackowiak, E. (Eds.). (2009). *Carbons for electrochemical energy storage and conversion systems*. Crc Press.
- Bouwman, P. J., Boukamp, B. A., Bouwmeester, H. J., Wondergem, H. J., and Notten, P. H. L. (2001). Structural analysis of submicrometer  $\text{LiCoO}_2$  films. *Journal of The Electrochemical Society*, 148(4), A311.
- Bouwman, P. J. (2002). Lithium intercalation in preferentially oriented submicron  $\text{LiCoO}_2$  films. *Netherland: University of Twente*.
- Buchmann, I. (2020.). *Basics about Batteries*. Retrieved from <http://www.cadex.com/en/batteries/basics-about-batteries>.
- Bunker, G. (2010). *Introduction to XAFS: a practical guide to X-ray absorption fine structure spectroscopy*. Cambridge University Press.
- Carlier, D., Saadoun, I., Croguennec, L., Ménétrier, M., Suard, E., and Delmas, C. (2001). On the metastable O2-type  $\text{LiCoO}_2$ . *Solid State Ionics*, 144(3-4), 263-276.
- Chadwick, A. V. (1993). EXAFS studies of dopant sites in metal oxides. *Solid State Ionics*, 63, 721-727
- Chang, Z., Chen, Z., Tang, H., Yuan, X.Z., and Wang, H. (2010). Synthesis and Characterization of Lamellar  $\text{LiCoO}_2$  as Cathode Materials for Lithium-Ion Batteries. *Journal of New Materials for Electrochemical Systems*, 13, 107-111.
- Chen, C.-H., Hwang, B.-J., Chen, C.-Y., Hu, S.-K., Chen, J.-M., Sheu, H.-S., and Lee, J.-F. (2007). Soft X-ray absorption spectroscopy studies on the chemically delithiated commercial  $\text{LiCoO}_2$  cathode material. *Journal of power sources*, 174, 938-943.
- Chen, H., Qiu, X., Zhu, W., and Hagemuller, P. (2002). Synthesis and high-rate properties of nanoparticled lithium cobalt oxides as the cathode material for lithium-ion battery. *Electrochemistry communications*, 4, 488-491.
- Cho, G.-B., Kim, J., and Cho, J. (2014). Electrochemically tunable thermal conductivity of lithium cobalt oxide. *Nature Communications*, 5, 4035.
- Cho, J., Hong, Y.-S., Choo, J., and Cho, J. (2009). Effect of  $\text{LiCoO}_2$  cathode nanoparticle size on high-rate performance for Li-ion batteries. *Journal of The Electrochemical Society*, 156(6), A430.

- Cho, K., Lee, T., Oh, J., and Shin, D. (2008). Electrochemical characteristics of LiCoO<sub>2</sub> nano-powder synthesized via aerosol flame deposition (AFD). *Journal of Physics and Chemistry of Solids*, 69, 1242-1245.
- Choi, S. H., Son, J.-W., Yoon, Y. S., and Kim, J. (2006). Particle size effects on temperature- dependent performance of LiCoO<sub>2</sub> in lithium batteries. *Journal of power sources*, 158, 1419-1424.
- Czyżyk, M., Potze, R., and Sawatzky, G. (1992). Band-theory description of high-energy spectroscopy and the electronic structure of LiCoO<sub>2</sub>. *Physical Review B*, 46, 3729.
- Dahéron, L., Martinez, H., Dedryvère, R., Baraille, I., Ménétrier, M., Denage, C., ... Gonbeau, D. (2009). Surface properties of LiCoO<sub>2</sub> investigated by XPS analyses and theoretical calculations. *The Journal of Physical Chemistry C*, 113(14), 5843-5852.
- Daniel, C., Mohanty, D., Li, J., and Wood, L. D. (2014). Cathode materials review, Aip Conference. *American Institute of Physics*, 1597, 26-43.
- Dong, H., and Koenig, G. M. (2020). A review on synthesis and engineering of crystal precursors produced via coprecipitation for multicomponent lithium-ion battery cathode materials. *CrystEngComm*, 22, 1514-1530.
- Ekwongsa, C., Rujirawat, S., Butnoi, P., Vittayakorn, N., Suttapun, M., Yimnirun, R., and Kidkhunthod, P. (2020). Temperature dependent local structure of LiCoO<sub>2</sub> determined by in-situ Co K-edge X-ray absorption fine structure (EXAFS). *Radiation Physics and Chemistry*, 175, 108545.
- Filez, M. (2015). *Alternative design of Pt-based catalysts: an X-ray spectroscopic view* (Doctoral dissertation, Ghent University).
- Fragnaud, P., Brousse, T., and Schleich, D.M. (1996). Characterization of sprayed and sputter deposited LiCoO<sub>2</sub> thin films for rechargeable microbatteries. *Journal of Power Sources*, 63(2), 187-191.
- Freitas, B. G., Siqueira, J. M., Costa, L. M. D., Ferreira, G. B., and Resende, J. A. (2017). Synthesis and Characterization of LiCoO<sub>2</sub> from Different Precursors by Sol-Gel Method. *Journal of the Brazilian Chemical Society*, 28, 2254-2266.

- Gabrisch, H., Yazami, R., and Fultz, B. (2004). Hexagonal to Cubic Spinel Transformation in Lithiated Cobalt Oxide TEM Investigation. *Journal of The Electrochemical Society*, 151(6), A891-A897.
- Gao, S., Wei, W., Ma, M., Qi, J., Yang, J., Chu, S., ... Guo, L. (2015). Sol-gel synthesis and electrochemical properties of c-axis oriented LiCoO<sub>2</sub> for lithium-ion batteries. *RSC Advances*, 5(64), 51483-51488.
- Gim, J., Zhang, Y., Gao, H., Xu, G. L., Guo, F., Ren, Y., ... Chen, Z. (2020). Probing solid-state reaction through microstrain: A case study on synthesis of LiCoO<sub>2</sub>. *Journal of Power Sources*, 469, 228422.
- De Groot, F. M., Hu, Z. W., López, M. F., Kaindl, G., Guillot, F., and Tronc, M. (1994). Differences between L3 and L2 x-ray absorption spectra of transition metal compounds. *The Journal of chemical physics*, 101(8), 6570-6576.
- Gummow, R., Thackeray, M., David, W., and Hull, S. (1992). Structure and electrochemistry of lithium cobalt oxide synthesised at 400 C. *Materials Research Bulletin*, 27, 327-337.
- Han, C. H., Hong, Y. S., Park, C. M., and Kim, K. (2001). Synthesis and electrochemical properties of lithium cobalt oxides prepared by molten-salt synthesis using the eutectic mixture of LiCl-Li<sub>2</sub>CO<sub>3</sub>. *Journal of power sources*, 92(1-2), 95-101.
- Hara, K., Yano, T.-a., Suzuki, K., Hirayama, M., Hayashi, T., Kanno, R., and Hara, M. (2017). Raman Imaging Analysis of Local Crystal Structures in LiCoO<sub>2</sub> Thin Films Calcined at Different Temperatures. *Analytical Sciences*, 33, 853-858.
- Heike, Y., Pat, S., Özen, S., Mohammadigharehbagh, R., Musaoğlu, C., Korkmaz, Ş., and Pat, Z. (2018). Microstructural, surface and electrochemical properties of the nano layered LiCoO<sub>2</sub> thin film cathode for Li-ion battery. *Vacuum*, 152, 248-251.
- Hench, L. L., and West, J. K. (1990). Principles of electronic ceramics. *Wiley*.
- Hippert, F., Geissler, E., Hodeau, J. L., Lelièvre-Berna, E., and Regnard, J. R. (2006). Neutron and X-ray Spectroscopy. *Netherlands: Springer*.
- Huang, C. C. (2008). *Structure and Piezoelectric Properties of Lead-Free Bismuth-Based Perovskite Solid Solutions*. Oregon State University, Oregon State.

- Oh, I. H., Hong, S. A., and Sun, Y. K. (1997). Low-temperature preparation of ultrafine  $\text{LiCoO}_2$  powders by the sol-gel method. *Journal of materials science*, *32*, 3177-3182.
- Trask, J., Anapolsky, A., Cardozo, B., Januar, E., Kumar, K., Miller, M., ... Bhardwaj, R. (2017). Optimization of 10- $\mu\text{m}$ , sputtered,  $\text{LiCoO}_2$  cathodes to enable higher energy density solid state batteries. *Journal of Power Sources*, *350*, 56-64.
- Jo, M., Hong, Y.-S., Choo, J., and Cho, J. (2009). Effect of  $\text{LiCoO}_2$  Cathode Nanoparticle Size on High Rate Performance for Li-Ion Batteries. *Journal of The Electrochemical Society*, *156*(6), A430-A434.
- Jos, F. M. O., Baggetto, L., and Notten, P. H. L. (2011). All-solid-state lithium-ion microbatteries: A review of various three-dimensional concepts. *Adv. Energy Mater*, *1*, 10-33.
- Julien, C. M., Mauger, A., and Hussain, O. M. (2019). Sputtered  $\text{LiCoO}_2$  Cathode Materials for All-Solid-State Thin-Film Lithium Microbatteries. *Materials*, *12*, 2687.
- Julien, C. M., Camacho-Lopez, M. A., Escobar-Alarcon, L., and Haro-Poniatowski, E. (2001). Fabrication of  $\text{LiCoO}_2$  thin-film cathodes for rechargeable lithium microbatteries. *Materials Chemistry and Physics*, *68*(1-3), 210-216.
- Jung, K. T., Cho, G. B., Kim, K. W., Nam, T. H., Jeong, H. M., Huh, S. C., ... Noh, J. P. (2013). Influence of the substrate texture on the structural and electrochemical properties of sputtered  $\text{LiCoO}_2$  thin films. *Thin solid films*, *546*, 414-417.
- Kang, S. G., Kang, S. Y., Ryu, K. S., and Chang, S. H. (1999). Electrochemical and structural properties of HT- $\text{LiCoO}_2$  and LT- $\text{LiCoO}_2$  prepared by the citrate sol-gel method. *Solid State Ionics*, *120*, 155.
- Klysubun, W. (2006). *X-ray Absorption Spectroscopy Technique*. Nakhon Ratchasima Synchrotron Light Research Institute.
- Kim, J., Fulmer, P., and Manthiram, A. (1999). Synthesis of  $\text{LiCoO}_2$  cathodes by an oxidation reaction in solution and their electrochemical properties. *Materials Research Bulletin*, *34*, 571-579.
- Kim, W.-S. (2004). Characteristics of  $\text{LiCoO}_2$  thin film cathodes according to the annealing ambient for the post-annealing process. *J. Power Sources*, *134*, 103-109.

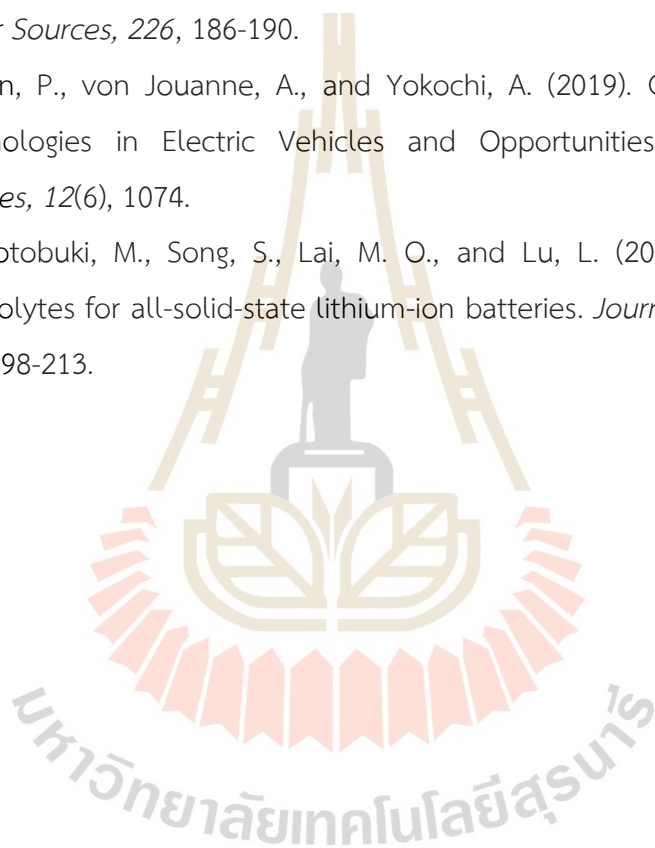
- Kodre, A. (2002). XANES spectroscopy. Retrieved from <http://www.ung.si/~arcon/xas/xanes/xanes-theory.pdf>.
- Kosova, N. V., Anufrienko, V. F., Larina, T. V., Rougier, A., Aymard, L., and Tarascon, J. M. (2002). Disorder and Electronic State of Cobalt Ions in Mechanochemically Synthesized  $\text{LiCoO}_2$ . *Journal of Solid State Chemistry*, 165, 56.
- Lala, S., Montoro, L., and Rosolen, J. (2003).  $\text{LiCoO}_2$  sub-micron particles obtained from micro-precipitation in molten stearic acid. *Journal of Power Sources*, 124, 118-123.
- Natoli, C. R., Misemer, D. K., Doniach, S., and Kutzler, F. W. (1980). First-principles calculation of x-ray absorption-edge structure in molecular clusters. *Physical Review A*, 22(3), 1104.
- Lee, J.-K., Lee, S.-J., Baik, H.-K., Lee, H.-Y., Jang, S.-W., and Lee, S.-M. (1999). Substrate effect on the microstructure and electrochemical properties in the deposition of a thin film  $\text{LiCoO}_2$  electrode. *Electrochemical and Solid-State Letters*, 2, 512-515.
- Le Van-Jodin, L., Rouchon, D., Le, V. H., Chevalier, I., Brun, J., and Secouard, C. (2019). Ex situ and operando study of  $\text{LiCoO}_2$  thin films by Raman spectroscopy: Thermal and electrochemical properties. *Journal of Raman Spectroscopy*, 50, 1594-1601.
- Liao, C.-L., and Fung, K.-L. (2004). Lithium cobalt oxide cathode film prepared by rf sputtering. *J. Power Sources*, 128, 263-269.
- Liao, C.-L., Wu, M.-T., Yen, J.-H., Leu, I.-C., and Fung, K.-Z. (2006). Preparation of RF-sputtered lithium cobalt oxide nanorods by using porous anodic alumina (PAA) template. *Journal of Alloys and Compounds*, 414, 302-309.
- Lin, F., Liu, Y., Yu, X., Cheng, L., Singer, A., Shpyrko, O. G., ... Doeff, M. M. (2017). Synchrotron X-ray analytical techniques for studying materials electrochemistry in rechargeable batteries. *Chemical reviews*, 117(21), 13123-13186.
- Liu, R., Duay, J., and Lee, S. B. (2011). Heterogeneous nanostructured electrode materials for electrochemical energy storage. *Chemical communications*, 47(5), 1384-1404.

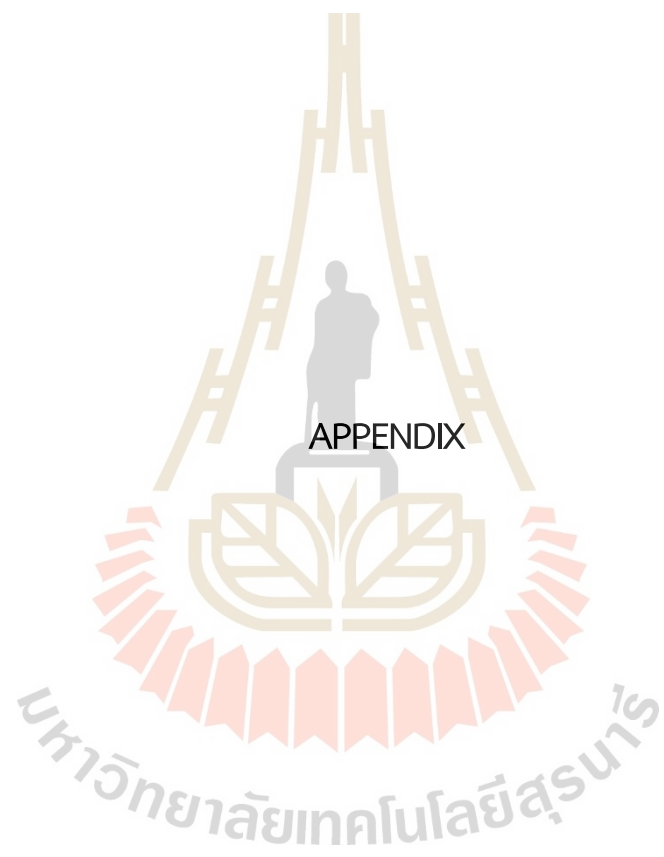
- Lyu, Y., Wu, X., Wang, K., Feng, Z., Cheng, T., Liu, Y., ... Guo, B. (2021). An overview on the advances of  $\text{LiCoO}_2$  cathodes for lithium-ion batteries. *Advanced Energy Materials*, 11(2), 2000982.
- M. S. Whittingham. (2008). Materials Challenges Facing Electrical Energy Storage. *Materials Research Bulletin*, 33, 411.
- Matsuda, Y., Kuwata, N., Okawa, T., Dorai, A., Kamishima, O., and Kawamura, J. (2019). In situ Raman spectroscopy of  $\text{Li}_x\text{CoO}_2$  cathode in  $\text{Li}/\text{Li}_3\text{PO}_4/\text{LiCoO}_2$  all-solid-state thin-film lithium battery. *Solid State Ionics*, 335, 7-14.
- Maurya, D. K., Sardarinejad, A., and Alameh, K. (2014). Recent developments in R.F. magnetron sputtered thin films for pH sensing applications—An overview. *Journal of Coatings*, 4, 756-771.
- Masaki Yoshio, R. J. B., and Akiya Kozawa. (2009). *Lithium-ion batteries: Science and technologies*. Springer.
- Maugeri, L., Simonelli, L., Iadecola, A., Joseph, B., Okubo, M., Honma, I., ... Saini, N. L. (2013). Temperature dependent local structure of  $\text{LiCoO}_2$  nanoparticles determined by Co K-edge X-ray absorption fine structure. *Journal of power sources*, 229, 272-276.
- Mizushima, K., Jones, P., Wiseman, P., and Goodenough, J. B. (1980).  $\text{Li}_x\text{CoO}_2$  ( $0 < x < 1$ ): A new cathode material for batteries of high energy density. *Materials Research Bulletin*, 15, 783-789.
- McCusker, L. B., Von Dreele, R. B., Cox, D. E., Louër, D., and Scardi, P. (1999). Rietveld refinement guidelines. *Journal of Applied Crystallography*, 32(1), 36-50.
- Nishi, Y. (2001). Lithium ion secondary batteries; past 10 years and the future. *Journal of Power Sources*, 100, 101-106.
- Noh, J. P., Cho, G. B., Jung, K. T., Kang, W. G., Ha, C. W., Ahn, H. J., ... Kim, K. W. (2012). Fabrication of  $\text{LiCoO}_2$  thin film cathodes by DC magnetron sputtering method. *Materials Research Bulletin*, 47(10), 2823-2826.
- Orman, H. J., and Wiseman, P. J. (1984). Cobalt(III) lithium oxide,  $\text{CoLiO}_2$ : Structure refinement by powder neutron diffraction. *Acta Crystallographica*, 40, 12.

- Patridge, C. J., Love, C. T., Swider-Lyons, K. E., Twigg, M. E., and Ramaker, D. E. (2013). In-situ X-ray absorption spectroscopy analysis of capacity fade in nanoscale-LiCoO<sub>2</sub>. *Journal of Solid State Chemistry*, 203, 134-144.
- Peled, E., Golodnitsky, D., Ulus, A., and Yufit, V. (2004). Effect of carbon substrate on SEI composition and morphology. *Electrochimica acta*, 50(2-3), 391-395.
- Rana, J., Kloepsch, R., Li, J., Scherb, T., Schumacher, G., Winter, M., and Banhart, J. (2014). On the structural integrity and electrochemical activity of a 0.5Li<sub>2</sub>MnO<sub>3</sub>·0.5LiCoO<sub>2</sub> cathode material for lithium-ion batteries. *Journal of Materials chemistry A*, 2(24), 9099-9110.
- Ravel, B., and Newville, M. A. T. H. E. N. A. (2005). ATHENA, ARTEMIS, HEPHAESTUS: data analysis for X-ray absorption spectroscopy using IFEFFIT. *Journal of synchrotron radiation*, 12(4), 537-541.
- Rehr, J. J., and Albers, R. C. (2000). Theoretical approaches to x-ray absorption fine structure. *Reviews of modern physics*, 72(3), 621.
- Rossen, E., Reimers, J. N., and Dahn, J. R. (1993). Synthesis and electrochemistry of spinel LT-LiCoO<sub>2</sub>. *Solid State Ionics*, 62, 53.
- Sakurai, J. J. (1967). *Advanced quantum mechanics*. Pearson Education India.
- Serebrennikova, I., and Birss, V. I. (1997). Electrochemical behavior of sol-gel produced Ni and Ni-Co oxide films. *Journal of the Electrochemical Society*, 144(2), 566.
- Scrosati, B., and Garche, J. (2010). Lithium batteries: Status, prospects and future. *Journal of Power Sources* 195(9), 2419-2430.
- Sheu, S., Yao, C., Chen, J., and Chiou, Y. (1997). Influence of the LiCoO<sub>2</sub> particle size on the performance of lithium-ion batteries. *Journal of Power Sources*, 68, 533-535.
- Stern, E. A., and Heald, S. M. (1983). Basic principle and applications of EXAFS. *Journal of Synchrotron Radiation*, 10, 995
- Sun, X., Lee, H. S., Yang, X. Q., and McBreen, J. (2002). A new additive for lithium battery electrolytes based on an alkyl borate compound. *Journal of the Electrochemical Society*, 149(3), A355.

- Sun, Y.-K. (1999). Cycling behaviour of  $\text{LiCoO}_2$  cathode materials prepared by PAA-assisted sol-gel method for rechargeable lithium batteries. *Journal of Power Sources*, 83, 223-226.
- Tang, W., Kanoh, H., and Ooi, K. (1998). Preparation of lithium cobalt oxide by  $\text{LiCl}$  flux method for lithium rechargeable batteries. *Electrochemical and Solid State Letters*, 1, 145.
- Tarascon, J.-M., and Armand, M. (2001). Issues and challenges facing rechargeable lithium batteries. *Nature* 414(6861), 359-367.
- Terada, N., Yanagi, T., Arai, S., Yoshikawa, M., Ohta, K., Nakajima, N., ... Arai, N. (2001). Development of lithium batteries for energy storage and EV applications. *Journal of Power Sources*, 100(1-2), 80-92.
- Thompson, A. C., and Vaughan, D. (Eds.). (2001). *X-ray data booklet* (Vol. 8, No. 4). Berkeley, CA: Lawrence Berkeley National Laboratory, University of California.
- Tintignac, S., Baddour-Hadjean, R., Pereira-Ramos, J. P., and Salot, R. (2014). High rate bias sputtered  $\text{LiCoO}_2$  thin films as positive electrode for all-solid-state lithium microbatteries. *Electrochimica Acta*, 146, 472-476.
- Toby, B. H. (2006). R factors in Rietveld analysis: how good is good enough. *Powder Diffraction* 12(1), 67-70.
- Turrell, S. J., Zekoll, S., Liu, J., Grovenor, C. R., and Speller, S. C. (2021). Optimization of a potential manufacturing process for thin-film  $\text{LiCoO}_2$  cathodes. *Thin Solid Films* 735, 138888.
- Wang, B., Bates, J. B., Hart, F. X., Sales, B. C., Zuhr, R. A., and Robertson, J. D. (1996). Characterization of Thin-Film Rechargeable Lithium Batteries with Lithium Cobalt Oxide Cathodes. *Journal of the Electrochemical Society*, 143(10), 3203-3213.
- Wang, Y., Liu, B., Li, Q., Cartmell, S., Ferrara, S., Deng, Z. D., and Xiao, J. (2015). Lithium and lithium-ion batteries for applications in microelectronic devices: A review. *Journal of Power Sources* 286, 330-345.

- Woo-Seong, K. (2004). Characteristics of  $\text{LiCoO}_2$  thin film cathodes according to the annealing ambient for the post-annealing process. *J. Power Sources*, 134, 103–109.
- Xu, K. (2004). Nonaqueous liquid electrolytes for lithium-based rechargeable batteries. *Chemical Reviews*, 104(10), 4303-441.
- Yoon, Y., Park, C., Kim, J., and Shin, D. (2013). Lattice orientation control of lithium cobalt oxide cathode film for all-solid-state thin film batteries. *Journal of Power Sources*, 226, 186-190.
- Yu, M., Hynan, P., von Jouanne, A., and Yokochi, A. (2019). Current Li-Ion Battery Technologies in Electric Vehicles and Opportunities for Advancements. *Energies*, 12(6), 1074.
- Zheng, F., Kotobuki, M., Song, S., Lai, M. O., and Lu, L. (2018). Review on solid electrolytes for all-solid-state lithium-ion batteries. *Journal of Power Sources*, 389, 198-213.







Contents lists available at ScienceDirect

## Radiation Physics and Chemistry

journal homepage: [www.elsevier.com/locate/radphyschem](http://www.elsevier.com/locate/radphyschem)Effect of thermal annealing on the structure of LiCoO<sub>2</sub> powders prepared by co-precipitation method

Awadol Khejonrak<sup>a</sup>, Narong Chanlek<sup>a,b,\*</sup>, Usa Sukkha<sup>c</sup>, Narit Triamnak<sup>e</sup>, Prae Chirawatkul<sup>b</sup>, Pinit Kidkhunthod<sup>a,b</sup>, Manoon Suttapun<sup>d</sup>, Naratip Vittayakorn<sup>d</sup>, Prapan Manyum<sup>a</sup>, Saroj Rujirawat<sup>b</sup>, Prayoon Songsiririthigul<sup>a</sup>, Rattikorn Yimnirun<sup>f</sup>

<sup>a</sup> Research Network NANOTEC-SUT on Advanced Nanomaterials and Characterization, School of Physics, Institute of Science, Suranaree University of Technology, Nakhon Ratchasima, 30000, Thailand

<sup>b</sup> Synchrotron Light Research Institute, Nakhon Ratchasima, 30000 Thailand

<sup>c</sup> Department of General Science and Liberal Arts, King Mongkut's Institute of Technology Ladkrabang, Chumphon Campus, Chumphon, 86160, Thailand

<sup>d</sup> Department of Chemistry, Faculty of Science, King Mongkut's Institute of Technology Ladkrabang, Bangkok, 10520, Thailand

<sup>e</sup> Department of Materials Science and Engineering, Faculty of Engineering and Industrial Technology, Silpakorn University, Nakhon Pathom, 73000, Thailand

<sup>f</sup> School of Energy Science and Engineering, Vidyasirimedhi Institute of Science and Technology (VISTEC), Wangchan, Rayong, 21210, Thailand

## ARTICLE INFO

## Keywords:

Co-precipitation method  
X-ray absorption spectroscopy  
LiCoO<sub>2</sub>  
Synchrotron powder X-ray diffraction

## ABSTRACT

Lithium cobalt oxide (LiCoO<sub>2</sub>) powder was prepared by co-precipitation method and annealed at different temperatures of between 300 and 700 °C. The effect of annealing temperature and effect washing process with deionized water on the crystal structures of the prepared LiCoO<sub>2</sub> powders were thoroughly studied by Synchrotron powder X-Ray Diffraction (Syn-XRD), X-ray Absorption Spectroscopy (XAS), Dispersive Raman Microscopy (Raman) techniques. The change in chemical composition as a function of annealing temperature was also investigated by X-ray Photoelectron Spectroscopy (XPS) technique. The crystal structural results identified the phase evolution of the prepared LiCoO<sub>2</sub> powders upon heat treatment. The formation of HT-LiCoO<sub>2</sub> phase was observed at annealing temperature as low as 300 °C.

## 1. Introduction

Lithium cobalt oxide (LiCoO<sub>2</sub>) is the most widely used material for positive electrode in commercial Li-ion batteries (LIBs). It was first suggested as the intercalation compound for rechargeable LIBs by Goodenough and Mizushima et al., in 1976 resulting in its commercialization by Sony Corporation in the early 1990s (Mizushima et al., 1980; Nishi, 2001). The migration of lithium ion in the layer structure oxide of LiCoO<sub>2</sub> is easier than other lithium metal oxide structures. This advantage significantly affects to LIBs performance excellence in terms of high specific energy density, low self-discharge and excellent cycle life.

Two types of crystallographic structures of LiCoO<sub>2</sub> were reported depending on the synthesis method and temperature. The first structure is the hexagonal-NaFeO<sub>2</sub> structure of LiCoO<sub>2</sub>, space group R-3m, which is usually observed at high temperature of approximately 750 °C (Czyżyk et al., 1992). This phase, also called HT-LiCoO<sub>2</sub>, consists of layers of

lithium ion (Li<sup>+</sup>) between slabs of octahedral formed by cobalt (Co<sup>3+</sup>) and oxygen (O<sup>2-</sup>) ions. The second structure is the cubic spinel structure which is usually stable at low temperatures (LT-LiCoO<sub>2</sub>). The crystal structure of LiCoO<sub>2</sub> strongly influences performances of the LIBs. Previous studies have shown that the HT-LiCoO<sub>2</sub> exhibits better electrochemical performances compared to that with the LT-LiCoO<sub>2</sub> (Wang et al., 2015). Also, the electrochemical property of the LiCoO<sub>2</sub> particles depends upon shape, size, agglomeration and growth orientation.

The HT-LiCoO<sub>2</sub> can be synthesized by a conventional solid-state reaction method with calcination temperature as high as 850–900 °C for several hours. This technique is highly potential for mass production, but, it is difficult to control the impurities and morphology/particle size of the LiCoO<sub>2</sub> powder (Antolini, 2004; Gim et al., 2020). The HT-LiCoO<sub>2</sub> formation is also seen in the lower annealing temperatures when the different synthesis methods, especially wet techniques, are proceeded. Co-precipitation technique, hence, is another attractive technique for LiCoO<sub>2</sub> synthesis. This wet chemical technique has been, generally, used

\* Corresponding author. Research Network NANOTEC-SUT on Advanced Nanomaterials and Characterization, School of Physics, Institute of Science, Suranaree University of Technology, NakhonRatchasima, 30000, Thailand.

E-mail address: [narong@slri.or.th](mailto:narong@slri.or.th) (N. Chanlek).

<https://doi.org/10.1016/j.radphyschem.2021.109766>

Received 31 January 2021; Received in revised form 13 August 2021; Accepted 26 August 2021

Available online 30 August 2021

0969-806X/© 2021 Elsevier Ltd. All rights reserved.

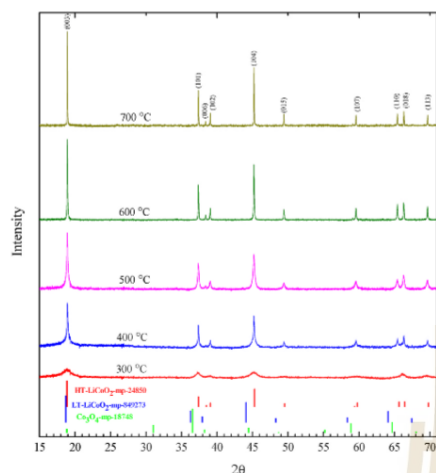


Fig. 1. Syn-XRD patterns of the prepared  $\text{LiCoO}_2$  powders annealed at different temperatures for 10 h.

to prepare nano powder of ceramics under ambient atmosphere and temperature (Chang et al., 2010; Dong and Koenig, 2020; Kim et al., 1999; Lala et al., 2003). It is simple, cost-effective, rapid, scalable and particle morphology controllable. However, the synthesized powder by this method yet needs to be calcined at high temperature after the preparation for the amorphous to crystalline structures transformation. Kim et al. synthesized the  $\text{LiCoO}_2$  by the co-precipitation method based on acetate solutions, lithium hydroxide and lithium peroxide solutions. The HT- $\text{LiCoO}_2$  was observed after annealing at  $900^\circ\text{C}$  for 3 days, yielding the highest capacity of, approximately, 150 mAh/g in the range between 4.3 and 3.3 V (Kim et al., 1999). Chen et al. prepared the  $\text{LiCoO}_2$  nanoparticles by the co-precipitation method in ethanol solution with lithium and cobalt salts. It was reported that the annealed sample at  $600^\circ\text{C}$  for 10 h showed the HT- $\text{LiCoO}_2$  structure with the best electrochemical properties (Chen et al., 2002). In addition, Ekwongsa et al. recently reported the structural investigations of  $\text{LiCoO}_2$  powder which prepared by the co-precipitation method from lithium and cobalt nitrate in ethanol solution (Ekwongsa et al., 2020). They studied the structural transformation of the  $\text{LiCoO}_2$  powder by conventional X-ray Diffraction (XRD) and in-situ X-ray Absorption Spectroscopy (XAS) techniques. The HT- $\text{LiCoO}_2$  structure was observed at  $700^\circ\text{C}$  in their investigations. However, the nitrate by-products were not removed from their powders after preparations and they actually needed to be eliminated by deionized water. The washing process could deviate the investigation results.

In this work, we performed a fundamental study on structural characteristics of  $\text{LiCoO}_2$  powder which prepared by co-precipitation method as well as the effect of washing process with deionized water on its chemical compositions. Since, there were scant reports of the investigations with this preparation method, hence, the  $\text{LiCoO}_2$  properties prepared via co-precipitation method were systematically studied by

using Synchrotron-based X-ray techniques. Effect of thermal annealing on the structure of the  $\text{LiCoO}_2$  was also investigated by the Synchrotron X-ray Diffraction (Syn-XRD), XAS and Dispersive Raman Microscopy (Raman) techniques. Syn-XRD with intense X-ray beam can provide a greater signal to noise ratio than the conventional XRD and it can avoid background fluorescence by wavelength adjustment. Therefore, the structural investigation by using Syn-XRD should reveal more precise and accurate information of  $\text{LiCoO}_2$  structures leading to the better understanding. It should be noted that besides of its advantages, Syn-XRD technique still produces average structural information from the crystalline phases with only long-range order. In addition, the investigations by the Synchrotron X-ray techniques in this study included the X-ray Absorption Near-Edge Structure (XANES) and the Extended X-ray Absorption Fine Structure (EXAFS). While XANES reflected the oxidation state, electronic configuration and site symmetry of the absorbing atom, the EXAFS gave structural quantitative information of short-range-order parameters such as species and numbers of neighboring atoms, the interatomic distances and Debye-Waller factor (Lin et al., 2017). The surface morphologies and chemical compositions of the  $\text{LiCoO}_2$  powders were also characterized by Field Emission Scanning Electron Microscope (FE-SEM) and X-ray Photoelectron Spectroscopy (XPS) techniques.

## 2. Experiments

### 2.1. Synthesis

The  $\text{LiCoO}_2$  powders were prepared by the co-precipitation method in ethanol solution and reacting with KOH solution. Briefly, 1.1M of  $\text{LiNO}_3 \cdot 6\text{H}_2\text{O}$  and 1M of  $\text{Co}(\text{NO}_3)_2 \cdot 6\text{H}_2\text{O}$  were dissolved in 100 mL of ethanol and, subsequently, stirred at room temperature for 1 h. The mixture solution was then precipitated by adding 3 M of KOH (dissolved in 500 mL ethanol) by rate value of 1 drop per second with simultaneously stirring at room temperature for 1 h to promote  $\text{LiCoO}_2$  precursor solution. The precursor solution was separated by centrifugation

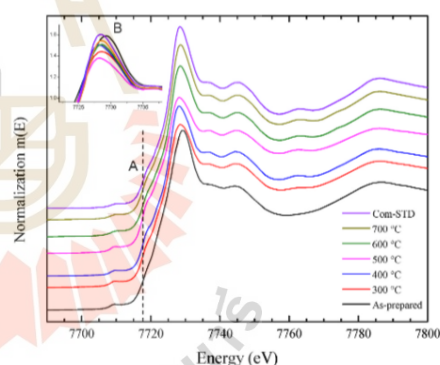


Fig. 2. XANES spectra of Co K-edge of the prepared  $\text{LiCoO}_2$  powders annealed at different temperatures for 10 h.

Table 1

The lattice parameters of the  $\text{LiCoO}_2$  powders annealed at different temperatures.

| Samples | a (Å)  | c (Å)   | c/a     | Goodness of fit (GOF) | Residual of least-squares refinemen (Rp) | Weighted residual (Rwp) | $I_{002}/I_{004}$ | crystallite size (nm) |
|---------|--------|---------|---------|-----------------------|--|-------------------------|-------------------|-----------------------|
| 400     | 2.8185 | 14.0419 | 4.98204 | 3.78                  | 14.72                                    | 20.23                   | 1.5009            | $45.9 \pm 2.7$        |
| 500     | 2.8171 | 14.0558 | 4.98946 | 1.23                  | 5.29                                     | 6.72                    | 1.5778            | $44.3 \pm 2.4$        |
| 600     | 2.8168 | 14.0542 | 4.98942 | 0.97                  | 5.59                                     | 7.15                    | 1.4318            | $89.98 \pm 3.0$       |
| 700     | 2.8165 | 14.0534 | 4.98967 | 0.96                  | 4.06                                     | 5.18                    | 1.5479            | $140.2 \pm 5.7$       |

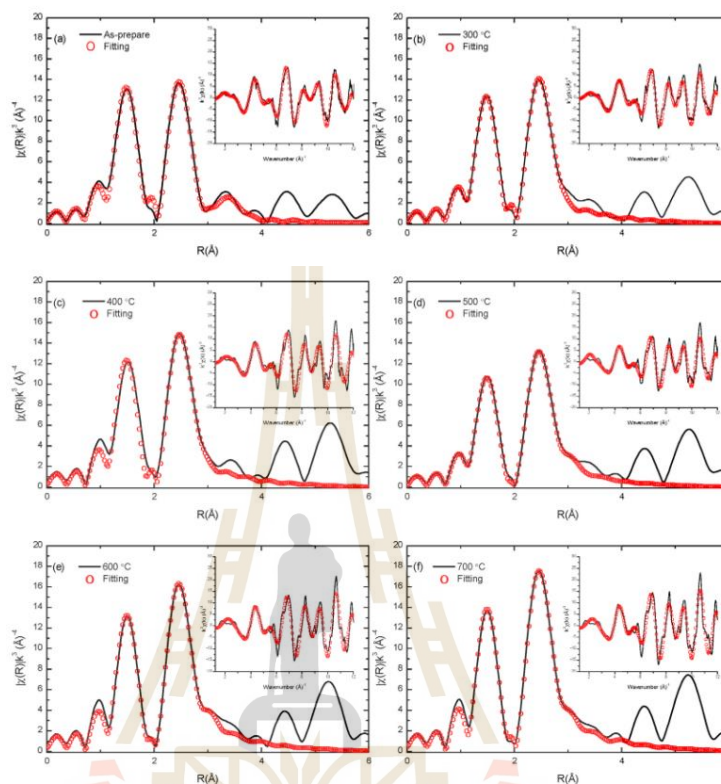


Fig. 3. Fourier transform EXAFS spectra at the Co K-edge and  $k$ -space (insets) of the prepared  $\text{LiCoO}_2$  powders annealed at different temperatures for 10 h.

Table 2

Summary of EXAFS fitting parameters including interatomic distances (R), coordination numbers (N) and Debye-Waller factors ( $\sigma$ ).

| Sample      | Shell | N | $\sigma^2$ | R(Å)    |
|-------------|-------|---|------------|---------|
| As-prepared | Co-O  | 6 | 0.00125    | 1.89456 |
| 300 °C      | Co-O  | 6 | 0.00190    | 1.89587 |
| 400 °C      | Co-O  | 6 | 0.00205    | 1.90882 |
| 500 °C      | Co-O  | 6 | 0.00318    | 1.90964 |
| 600 °C      | Co-O  | 6 | 0.00372    | 1.91098 |
| 700 °C      | Co-O  | 6 | 0.00309    | 1.91165 |
| As-prepared | Co-Co | 6 | 0.00371    | 2.83149 |
| 300 °C      | Co-Co | 6 | 0.00314    | 2.81754 |
| 400 °C      | Co-Co | 6 | 0.00266    | 2.82097 |
| 500 °C      | Co-Co | 6 | 0.00324    | 2.82019 |
| 600 °C      | Co-Co | 6 | 0.00343    | 2.81385 |
| 700 °C      | Co-Co | 6 | 0.00277    | 2.81195 |

at 7000 rpm for 10 min. The powder was washed with ethanol until free from hydroxide ions and subsequently dried at 50 °C. The dried precursor was annealed at 300, 400, 500, 600, and 700 °C for 10 h in air. The final products were washed with deionized water until free from potassium nitrate ( $\text{KNO}_3$ ), and subsequently dried at 50 °C.

## 2.2. Characterization

The Syn-XRD measurements were performed with the monochromatic synchrotron X-ray radiation energy of 12 keV and converted wavelength of 1.5409 Å at BL1.1W: Multiple X-ray techniques at the Synchrotron Light Research Institute (SLRI), Thailand. The prepared  $\text{LiCoO}_2$  powders were packed in Kapton capillary (diameter = 0.3 mm). The Syn-XRD data were collected in the  $2\theta$  scan range of 20–80° at room temperature and the capillaries were spun at 200 rpm during the measurements. The obtained patterns were refined by using the Jana2006 program.

The XAS experiments, including XANES and EXAFS, were performed at BL5.2: SUT-NANOTEC-SLRI XAS, SLRI, Thailand. The measurements at the Co K-edge were made in transmission mode using the monochromator employing Ge(220) crystal pairs at room temperature. The Raman spectral imaging was performed using an area-scan dispersive Raman microscope (SENTERRA, Bruker). The Raman scattering was captured from 25 points on a sample, with an excitation wavelength of 532 nm, power of 25 mW, and 25  $\mu\text{m} \times 1000 \mu\text{m}$  slit. The spectra were collected in a range of 50–1520  $\text{cm}^{-1}$  with Raman shift resolution of 0.5  $\text{cm}^{-1}$ .

The XPS measurements were performed on a PHI5000 Versa probe II XPS system (ULVAC-PHI, Japan) at the SUT-NANOTEC-SLRI joint

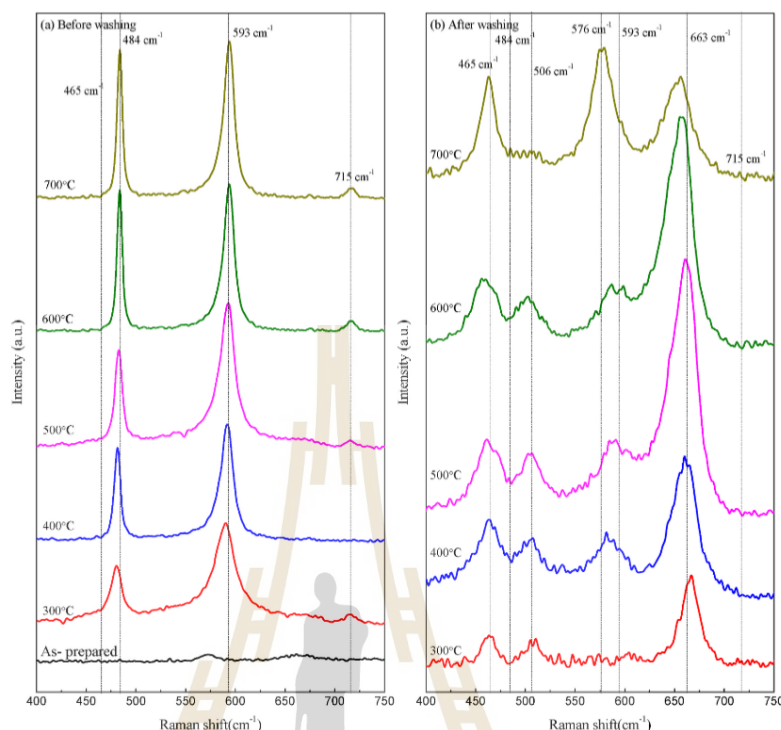


Fig. 4. Raman spectra of the prepared  $\text{LiCoO}_2$  powders annealed at different temperatures (a) before washing and (b) after washing with deionized water.

research facility, SLRI, Thailand. A monochromatic Al K $\alpha$  X-ray with an energy of 1486.6 eV was used as the excitation source. The XPS spectra were deconvoluted by using the MultiPak software. All binding energies were calibrated by referencing the C1s peak at 284.8 eV. The SEM images of the prepared  $\text{LiCoO}_2$  powders were taken by using field emission scanning electron microscope (FE-SEM, Carl Zeiss-AURIGA).

### 2.3. Results and discussion

The Syn-XRD patterns of the prepared  $\text{LiCoO}_2$  powders after washing with deionized water were shown in Fig. 1. The patterns of the prepared  $\text{LiCoO}_2$  powders matched well with the hexagonal- $\text{NaFeO}_2$  structure, COD-1550397 (space group R-3m). The second phases of  $\text{Co}_3\text{O}_4$  and chemical residuals, such as  $\text{KNO}_3$ , were not detected in the patterns. Hence, the HT- $\text{LiCoO}_2$  phase acquisition was affirmed throughout the annealing temperature range. However, the splitting doublets of the (0 0 6)/(1 0 2) and (1 0 8)/(1 1 0) peaks which were at around  $37^\circ$  and  $67^\circ$ , respectively, were hardly observed at  $300^\circ\text{C}$ . Those doublets were used to identify the HT- $\text{LiCoO}_2$  structure. The broadening of diffraction peaks was due to the crystallite size effect which will be discussed later. The two doublets started to be distinguishable with the annealing temperatures of  $400^\circ\text{C}$  which clearly indicated the existence of HT- $\text{LiCoO}_2$  phase at the annealing temperature as such. The observation of HT- $\text{LiCoO}_2$  phase with this annealing temperature was in good agreement with Chen et al. and Akimoto et al., (Akimoto et al., 1998; Chen et al., 2002). The observation was also lower than the reports by Kim et al. ( $900^\circ\text{C}$ ),

Chen et al. ( $600^\circ\text{C}$ ) and Ekwongsa et al. ( $700^\circ\text{C}$ ) (Kim et al., 1999; Chen et al., 2007; Ekwongsa et al., 2020).

As mentioned above, the Syn-XRD patterns showed HT- $\text{LiCoO}_2$  phase at the annealing temperature range of  $400\text{--}700^\circ\text{C}$ . The crystallite size and hexagonal unit cell parameters of those annealed samples were calculated by Rietveld refinement as listed in Table 1. The average crystallite sizes were  $45.9 \pm 2.7$  nm,  $44.3 \pm 2.4$  nm,  $89.98 \pm 3.0$  nm and  $140.2 \pm 5.7$  nm which obtained from the annealed samples at temperature of  $400$ ,  $500$ ,  $600$  and  $700^\circ\text{C}$ , respectively. It was clearly seen that the crystallite size tended to increase with the increase of the annealing temperature. Moreover, peak broadening generally related to the crystallite size decrease. Therefore, the broad peaks were usually observed at lower annealing temperature due to the smaller of atomic diffusion. The Syn-XRD pattern of the annealed powder at  $300^\circ\text{C}$  which should possess the smallest crystallite size, hence, revealed the noticeable broad peaks and the miserably observable splitting of the (0 0 6)/(1 0 2) and (1 0 8)/(1 1 0) doublets.

The lattice constant  $a$ ,  $c$  and  $c/a$  ratio of the annealed  $\text{LiCoO}_2$  powders at  $400$ ,  $500$ ,  $600$  and  $700^\circ\text{C}$  were (2.8185 Å, 14.0419 Å, 4.98204), (2.8171 Å, 14.0558 Å, 4.98946), (2.8168 Å, 14.0542 Å, 4.98942) and (2.8165 Å, 14.0534 Å, 4.98967), respectively, which were not significantly different. These lattice parameters were also close to those obtained in the previous reports by Lee et al. (2.8134 Å, 14.050 Å and 4.994), Gummow et al. (2.8179 Å, 14.0597 Å and 4.99) and Sun et al. (2.8134 Å, 14.0411 Å and 4.9908) (Gummow et al., 1992; Lee et al., 2008; Sun, 1999).

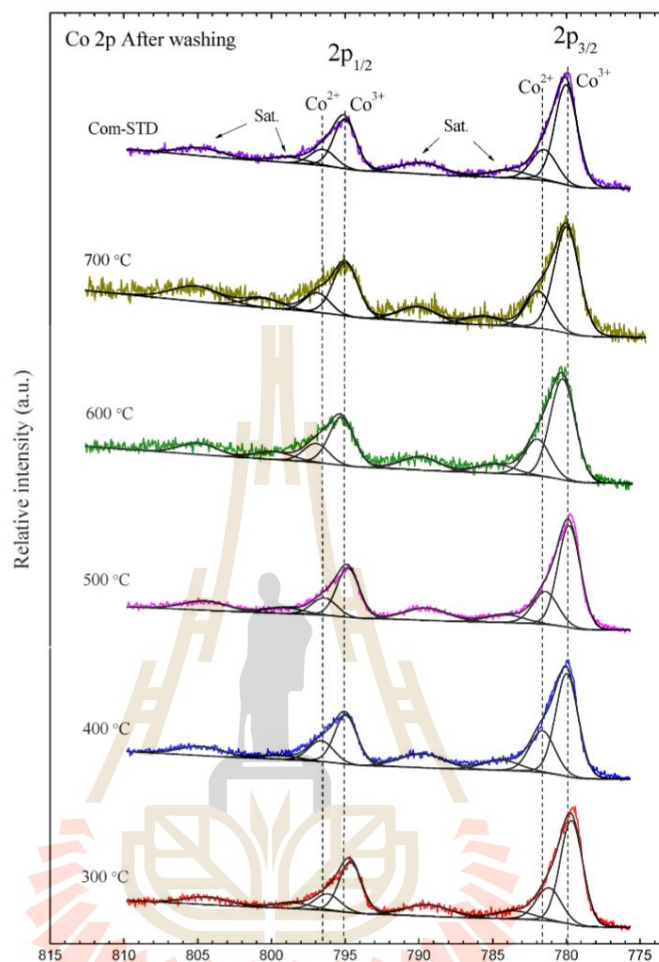


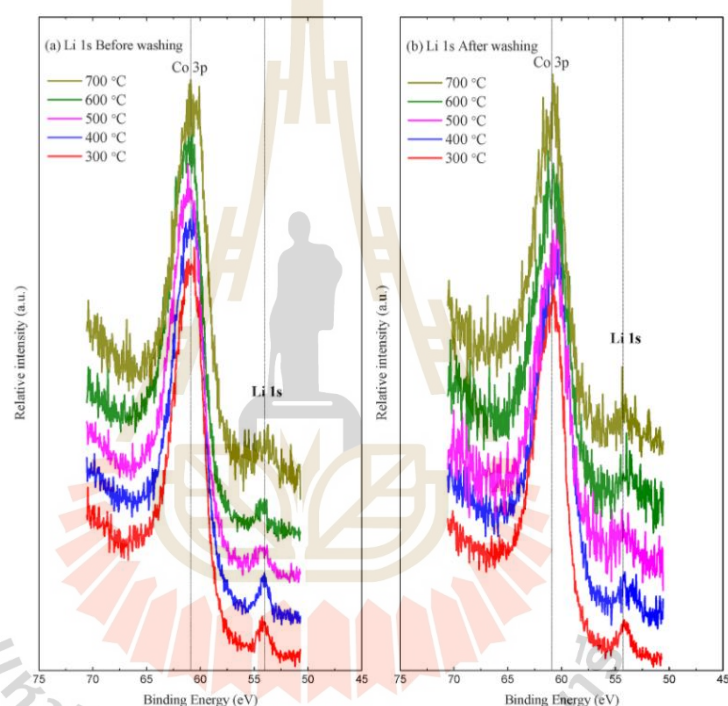
Fig. 5. High resolution XPS spectra of Co 2p of the LiCoO<sub>2</sub> annealed at different temperatures for 10 h.

As seen from the syn-XRD patterns, the highest intensity was from the (003) reflection followed by the (104) and (101) reflection, as expected from the diffraction data of pure LiCoO<sub>2</sub> (mp-2485). The strong intensity of the (003) peak suggested that the samples exhibited a well-developed layers structure and preferred c-axis orientation Tang et al., 1998. The relative intensity ratio between (0 0 3) and (1 0 4) peak ( $I_{003}/I_{104}$ ) was used to determine the degree of c-axis orientation (Tang et al., 1998; Gao et al., 2015). As seen from Table 1, the LiCoO<sub>2</sub> powders obtained from this work exhibited a low  $I_{003}/I_{104}$  value compared to the values of 16.5 and 24 which were obtained from the previous studies by Gao et al. and Weiping et al., respectively (Tang et al., 1998; Gao et al., 2015). The low c-axis oriented structure has been proposed to exhibit better electrochemical properties due to the consequential shorter diffusion distances for lithium ions (Gao et al., 2015).

The normalized XANES spectra at the Co K-edge of the annealed LiCoO<sub>2</sub> powders and commercial standard LiCoO<sub>2</sub> (Com-STD) were shown in Fig. 2. The absorption edge energies of Co were observed at 7717.7 eV, approximately, from all annealed LiCoO<sub>2</sub> powders. This suggested the unchanged oxidation state of Co within the annealing temperature range. The increase of the low energy shoulder feature (A), around 7720 eV, and the changes of the shape and height of the whiteline (B), around 7730 eV, with annealing temperature were observed. When the annealing temperature was increased from 300 to 500 °C, the shoulder A increased while the whiteline B changed. When the temperature was increased upto 600 °C, the shoulder disappeared with the significant increase of the whiteline. There were not any further observable changes in the XANES spectra between annealed samples at 600 and 700 °C. Moreover, the spectra of these two samples were almost

**Table 3**Summary of chemical compositions and oxidation states of Co from the LiCoO<sub>2</sub> powders annealed at different temperatures as estimated by XPS.

| Parameter                  | Annealed temperature               |        |        |        |        |        | Com-STD |        |
|----------------------------|------------------------------------|--------|--------|--------|--------|--------|---------|--------|
|                            | Co <sub>3</sub> O <sub>4</sub> STD | 300 °C | 400 °C | 500 °C | 600 °C | 700 °C |         |        |
| Peak Position (eV)         | Co <sup>3+</sup>                   | 780.12 | 779.64 | 779.96 | 779.8  | 780.24 | 779.97  | 780.01 |
|                            |                                    | 795.11 | 794.64 | 794.96 | 794.8  | 795.24 | 794.97  | 795.01 |
| Co <sup>2+</sup>           |                                    | 782.24 | 781.19 | 781.63 | 781.42 | 781.96 | 781.89  | 781.51 |
|                            |                                    | 797.26 | 796.19 | 796.63 | 796.42 | 796.96 | 796.89  | 796.51 |
| Peak Area                  | Co <sup>3+</sup>                   |        |        |        |        |        |         |        |
|                            | 2p <sub>3/2</sub>                  | 14351  | 10742  | 12862  | 14496  | 2939   | 1734    | 8380   |
| Co <sup>2+</sup>           | 2p <sub>1/2</sub>                  | 7207   | 5371   | 6174   | 7248   | 1469   | 867     | 4190   |
|                            | 2p <sub>3/2</sub>                  | 7176   | 3900   | 5884   | 5363   | 1122   | 606     | 2901   |
| Relative atomic percentage | 2p <sub>1/2</sub>                  | 3604   | 1950   | 2824   | 2682   | 561    | 303     | 1450   |
|                            | Co <sup>3+</sup> (%)               | 66.67  | 73.36  | 68.61  | 72.99  | 72.37  | 74.10   | 74.28  |
| Co <sup>2+</sup> (%)       | 33.33                              | 26.64  | 31.39  | 27.01  | 27.63  | 25.90  | 25.72   |        |
| Chi Squared                | 1.83                               | 1.95   | 2.19   | 2.18   | 1.64   | 1.35   | 1.38    |        |

**Fig. 6.** XPS spectra Li 1s of the prepared LiCoO<sub>2</sub> powders annealed at different temperatures (a) before washing and (b) after washing with deionized water.

identical as well as the spectrum of the commercial standard LiCoO<sub>2</sub>.

The shoulder and whiteline features corresponded to the 1s-4p transition which the former implicated the ligand to metal charges transfer with the shutdown process and the latter was without the shutdown process. The observed shoulder feature and low intensity whiteline at the low annealed samples could be a result of the overlapped O 2p and the hybridized Co 3d-4p orbitals which caused by tilted arrangement of CoO<sub>6</sub> octahedra. The arrangement changed at higher annealing temperature such that 3d-4p mixing reduced and caused the

disappearance of the shoulder feature and the increase of whiteline intensity (Patridge et al., 2013; Ching-Hsiang Chen et al., 2007). Thereby, although it was suggested by the Syn-XRD results that the formation of HT-LiCoO<sub>2</sub> structure occurred at 300 °C, the structure was incomplete. According to the XANES information, the minimum annealing temperature should be at 600 °C for the complete HT-LiCoO<sub>2</sub> structure.

The k<sup>3</sup>-weighted Fourier transform EXAFS spectra at the Co K-edge of the LiCoO<sub>2</sub> powders with different annealing temperatures were illustrated in Fig. 3. The results revealed two main peaks which are

**Table 4**  
Li/Co ratio of the LiCoO<sub>2</sub> powders annealed at different temperatures before washing and after washing with deionized water.

| Sample | Li/Co ratio    |               |
|--------|----------------|---------------|
|        | Before washing | After washing |
| 300    | 0.92           | 0.63          |
| 400    | 0.91           | 0.62          |
| 500    | 0.97           | 0.62          |
| 600    | 1.02           | 0.62          |
| 700    | 1.04           | 0.82          |

corresponded to Co-O and Co-Co. The amplitude ratio of Co-Co/Co-O grew when the annealing temperature increased suggesting the changes of CoO<sub>6</sub> arrangement according to the XANES results. This trend was also observed in previous reports (Chen et al., 2007; Rana et al., 2014). The information of structural parameters, namely, number of neighboring atoms (N), interatomic distances (R), and Debye-Waller factors ( $\sigma^2$ ) refined from the EXAFS spectra using Athena and Artemis programs (B. Ravel and M. Newville, 2005), were showed in Table 2. The EXAFS refinement revealed that the Co-Co atomic distances of the annealed LiCoO<sub>2</sub> powders were not significantly different, meanwhile the Co-O atomic distances slightly increased when the annealing temperature

increased suggesting the slight changes to the CoO<sub>6</sub> octahedra. The Co-O atomic distances of the LiCoO<sub>2</sub> were close to those previously reported (Ekwongsa et al., 2020).

The Raman spectra of the LiCoO<sub>2</sub> powders annealed at different temperatures before washing with deionized water were shown in Fig. 4 (a). The Raman results also showed a clear phase formation when the annealing temperature increased. Firstly, the LiCoO<sub>2</sub> precursor presented an amorphous structure. When the LiCoO<sub>2</sub> powder was annealed at 300 °C, the Raman peaks of LiCoO<sub>2</sub> feature were initially observed. The observed major peaks at 484 and 595 cm<sup>-1</sup> are attributed to E<sub>g</sub> and A<sub>1g</sub> mode, respectively. The E<sub>g</sub> mode corresponds to the O-Co-O bending and the A<sub>1g</sub> mode corresponds to the Co-O stretching (Hara et al., 2017; Jo et al., 2009; Matsuda et al., 2019). These Raman characteristics confirmed the HT-LiCoO<sub>2</sub> phase in the samples annealed at 300 °C which was also consistent with the XRD results. However, a small peak at 715 cm<sup>-1</sup> was observed in every samples which could represented to the residual phase of KNO<sub>3</sub> from the synthesis process (Acosta-Maeda et al., 2016). Therefore, we conducted the KNO<sub>3</sub> elimination by washing with deionized water and the Raman measurement again after washing. The Raman spectra of washed powder were shown in Fig. 4 (b). The small peak of KNO<sub>3</sub> could not be detected in all samples. Meanwhile, the two main peaks of HT-LiCoO<sub>2</sub> phase shifted to the lower wavenumber from 484 to 465 cm<sup>-1</sup> and 597 to 575 cm<sup>-1</sup> for E<sub>g</sub> and A<sub>1g</sub>

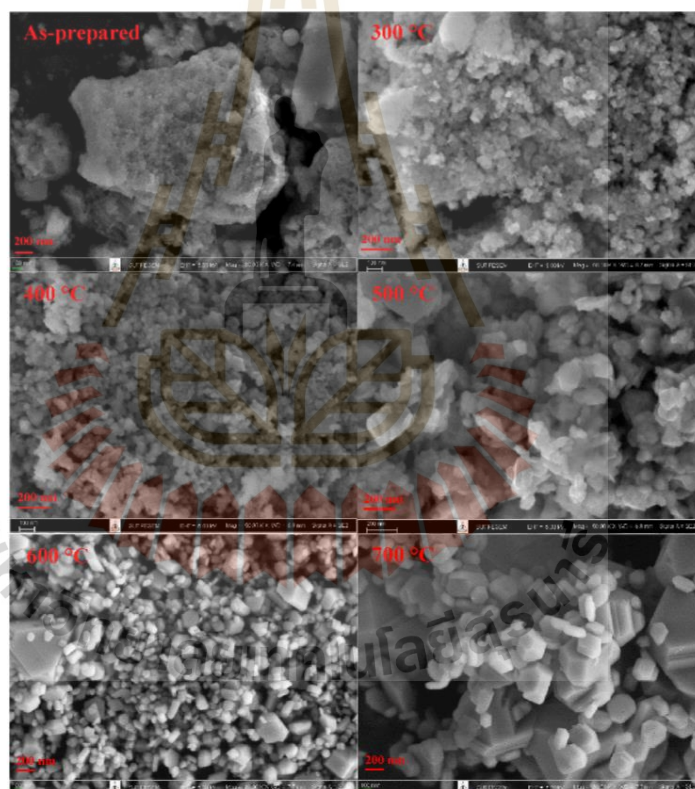


**Fig. 7.** FE-SEM images of the LiCoO<sub>2</sub> powders annealed at different temperatures for 10h.

modes, respectively. Interestingly, the large peaks possessed to  $\text{Co}_2\text{O}_4$  structure at 506 and 663  $\text{cm}^{-1}$  were observed. This discovery seemed to be consistent with Le Van-Jodin et al. (Le Van-Jodin et al., 2019). They studied Raman spectrum of HT-LiCoO<sub>2</sub> during the first charge/discharge cycle and found the HT-Li<sub>x</sub>CoO<sub>2</sub> phase shifting from 487 to 468  $\text{cm}^{-1}$  and 597 to 575  $\text{cm}^{-1}$  for  $E_g$  and  $A_{1g}$  modes, respectively. They explained the Raman shifts occurrence in term of the de-intercalation of  $\text{Li}^+$  ions and reconstruction of the atoms in the hexagonal structure to the monoclinic and  $\text{Co}_2\text{O}_4$  phase. Even though, the  $\text{Co}_2\text{O}_4$  phase was not detected by the XRD in our study in every samples after washing with deionized water, it was clearly seen by the Raman spectra. Meanwhile, the XANES spectra of annealed samples at 600 and 700 °C were not significantly different, however, these results contradicted with the Raman results, which the differences could be seen between the annealed samples at 600 and 700 °C. This result disagreement is plausible because Raman spectroscopy possesses higher surface sensitivity than XRD and XANES techniques. The surface composition changes could be disclosed via Raman spectroscopy. Hence, the de-intercalation of  $\text{Li}^+$  ions, especially, on the surface of LiCoO<sub>2</sub> particles due to the washing processes could be distinguished by surface investigation technique such as Raman spectroscopy.

The surface chemical compositions of the prepared LiCoO<sub>2</sub> powders were also investigated by XPS. High resolution XPS spectra of Co 2p peaks of the LiCoO<sub>2</sub> annealed at different temperatures after washing with deionized water were shown in Fig. 5. The Co 2p core level XPS peaks exhibited two main peaks due to spin-orbit coupling (Co 2p<sub>3/2</sub> and Co 2p<sub>1/2</sub>), with the binding energy separation closed to 15 eV. The Co 2p<sub>3/2</sub> peaks of all spectra can be deconvoluted into two peaks at the binding energies of 779.64–780.24 eV and 781.19–781.96 eV which were attributed to  $\text{Co}^{3+}$  and  $\text{Co}^{2+}$ , respectively (Daheron et al., 2009). The summary of chemical compositions and peak positions of Co from the prepared LiCoO<sub>2</sub> powders were shown in Table 3. The atomic contents of  $\text{Co}^{3+}$  and  $\text{Co}^{2+}$  of the LiCoO<sub>2</sub> powders annealed at different temperatures were not significantly variant.

High resolution XPS spectra of Li 1s peaks of the LiCoO<sub>2</sub> powders annealed at different temperatures before washing and after washing with deionized water were shown in Fig. 6. The Li 1s core level peaks of all spectra were observed at the binding energy of 54.0 eV, approximately, indicating the presence of  $\text{Li}^+$  (N. Andreu et al., 2015). The atomic ratio of Li and Co (Li/Co) was calculated by the following equation:

$$\text{Li} / \text{Co} = \frac{I_{\text{Li}1s} / S_{\text{Li}1s}}{I_{\text{Co}2p3/2} / S_{\text{Co}2p3/2}}$$

where,  $I_{\text{Li}1s}$  and  $I_{\text{Co}2p3/2}$  are integrated areas under Li 1s and Co 2p<sub>3/2</sub> peaks, respectively.  $S_{\text{Li}1s}$  and  $S_{\text{Co}2p3/2}$  are the sensitivity factors of Li 1s and Co 2p<sub>3/2</sub> peaks, respectively. The results were shown in Table 4. Before the washing process the Li/Co ratio increased when the annealing temperature increased. The Li/Co ratio of the LiCoO<sub>2</sub> powders annealed at 700 °C was 1.02 which was close to the perfect chemical composition of LiCoO<sub>2</sub>, Li/Co ratio is equal 1. This result was consistent with the results obtained from XRD, XAS and Raman techniques.

After washing with deionized water, the Li/Co ratio significantly decreased to the range of 0.62–0.82. The LiCoO<sub>2</sub> annealed at 700 °C displayed the highest Li/Co ratio of 0.82. This result indicated the loss of  $\text{Li}^+$  ions during washing with deionized water. The XPS results supported the assumption that the washing process could affect the de-intercalation of  $\text{Li}^+$  ions on the surface of LiCoO<sub>2</sub> particles.

#### 2.4. SEM

The morphologies of the LiCoO<sub>2</sub> powders annealed at different temperatures were illustrated in Fig. 7. The FE-SEM images showed the morphology evolution to the hexagonal shape particles with the increasing annealing temperature. The increase of particle size when the

annealing temperature increased were in agreement with the increase of crystallite size obtained from the Syn-XRD results. The hexagonal nanoparticles, with the irregular mixture between hexagonal structure and hexagonal flakelike structure, were clearly observed in LiCoO<sub>2</sub> powders annealed at 600 and 700 °C. (Choi et al., 2006; Sheu et al., 1997).

### 3. Conclusions

In this study, the LiCoO<sub>2</sub> powders were prepared by the coprecipitation method. The effect of annealing temperature and washing with deionized water on its properties were carried out by Syn-XRD, XAS, Raman spectroscopy, XPS and FE-SEM techniques. The results demonstrated the gradual phase evolution of LiCoO<sub>2</sub> powders with the increasing annealing temperature. The formation of HT-LiCoO<sub>2</sub> structure was partly observed at 300 °C and it was complete at the minimum annealing temperature of 600 °C. The Raman spectroscopy and XPS results suggested that the washing process induced the de-intercalation of  $\text{Li}^+$  ions on only the surface of LiCoO<sub>2</sub> particles.

#### Declaration of competing interest

The authors declare that they have no known competing financial interests or personal relationships that could have appeared to influence the work reported in this paper.

#### Acknowledgment

The authors would like to thank a partial financial support by the NANOTEC, NSTDA, Ministry of Science and Technology, Thailand, through its program of Research Network NANOTEC and School of Physics, Institute of Science, Suranaree University of Technology and the Synchrotron Light Research Institute (Public Organization), Thailand for XRD XAS XPS and Raman experiments.

#### References

- Acosta-Maeda, T.E., Misra, A.K., Muzangwa, L.G., Berlanga, G., Muchow, D., Porter, J., Sharma, S.K., 2016. Remote Raman measurements of minerals, organics, and inorganics at 430 m range. *Appl. Opt.* 55, 10283–10289. <https://doi.org/10.1364/ao.55.10283>.
- Akimoto, J., Gotoh, Y., Oosawa, Y., 1998. *Synthesis and Structure Refinement of LiCoO<sub>2</sub> Single Crystals*. Elsevier. <https://doi.org/10.1006/jssc.1998.7966>.
- Andreu, N., Flahaut, D., Dedryvere, R., Minvielle, M., Martinez, H., Gonbeau, D., 2015. XPS investigation of surface reactivity of electrode materials: effect of the transition metal. *ACS Appl. Mater. Interfaces* 7, 6629–6636. <https://doi.org/10.1021/am5089764>.
- Antolini, F., 2004. LiCoO<sub>2</sub>: formation, structure, lithium and oxygen nonstoichiometry, electrochemical behaviour and transport properties. *Solid State Ionics* 170, 159–171. <https://doi.org/10.1016/j.ssi.2004.04.003>.
- Chang, Z., Chen, Z., Tang, H., Yuan, X.Z., Wang, H., 2010. Synthesis and characterization of lamellar LiCoO<sub>2</sub> as cathode materials for lithium-ion batteries. *J. N. Mater. Electrochem. Syst.* 13, 107–111. <https://doi.org/10.14447/jnmes.v13i2.177>.
- Chen, C.-H., Hwang, B.-J., Chen, C.-Y., Hu, S.-K., Chen, J.-M., Sheu, H.-S., Lee, J.-F., 2007. Soft X-ray absorption spectroscopy studies on the chemically delithiated commercial LiCoO<sub>2</sub> cathode material. *J. Power Sources* 174, 938–943. <https://doi.org/10.1016/j.jpowsour.2007.06.083>.
- Chen, H., Qiu, X., Zhu, W., Hagenmüller, P., 2002. Synthesis and high rate properties of nanoparticled lithium cobalt oxides as the cathode material for lithium-ion battery. *Electrochem. Commun.* 4, 488–491. [https://doi.org/10.1016/S1388-2481\(02\)00357-0](https://doi.org/10.1016/S1388-2481(02)00357-0).
- Ghoi, S.H., Son, J.W., Yoon, Y.S., Kim, J., 2006. Particle size effects on temperature-dependent performance of LiCoO<sub>2</sub> in lithium batteries. *J. Power Sources* 158, 1419–1424. <https://doi.org/10.1016/j.jpowsour.2005.10.076>.
- Czyżyk, M., Potze, R., Sawatzky, G., 1992. Band-theory description of high-energy spectroscopy and the electronic structure of LiCoO<sub>2</sub>. *Phys. Rev. B* 46, 3729. <https://doi.org/10.1103/PhysRevB.46.3729>.
- Dahéron, I., Martinez, H., Dedryvere, R., Baraille, I., Ménétrier, M., Denage, C., Delmas, C., Gonbeau, D., 2009. Surface properties of LiCoO<sub>2</sub> investigated by XPS analyses and theoretical calculations. *J. Phys. Chem. C* 113, 5843–5852. <https://doi.org/10.1021/jp803265w>.
- Dong, H., Koenig, G.M., 2020. A review on synthesis and engineering of crystal precursors produced via coprecipitation for multicomponent lithium-ion battery cathode materials. *CrystEngComm* 22, 1514–1530. <https://doi.org/10.1039/C9CE00679F>.

- Ekongwa, C., Rujirawat, S., Butnoi, P., Vittayakorn, N., Sattapun, M., Yimnirun, R., Kidkhunthod, P., 2020. Temperature dependent local structure of LiCoO<sub>2</sub> determined by in-situ Co K-edge X-ray absorption fine structure (EXAFS). *Radiat. Phys. Chem.* 175, 108545. <https://doi.org/10.1016/j.radphyschem.2019.108545>.
- Gao, S., Wei, W., Ma, M., Qi, J., Yang, J., Chu, S., Zhang, J., Guo, L., 2015. Sol-gel synthesis and electrochemical properties of c-axis oriented LiCoO<sub>2</sub> for lithium-ion batteries. *RSC Adv.* 5, 51483–51488. <https://doi.org/10.1039/C5RA06571B>.
- Gim, J., Zhang, Y., Gao, H., Xu, G.-L., Guo, F., Ren, Y., Amine, K., Chen, Z., 2020. Probing solid-state reaction through microstrain: a case study on synthesis of LiCoO<sub>2</sub>. *J. Power Sources* 469, 228422. <https://doi.org/10.1016/j.jpowsour.2020.228422>.
- Gumnow, R., Thackeray, M., David, W., Hull, S., 1992. Structure and electrochemistry of lithium cobalt oxide synthesized at 400 °C. *Mater. Res. Bull.* 27, 327–337. [https://doi.org/10.1016/0025-5408\(92\)90062-5](https://doi.org/10.1016/0025-5408(92)90062-5).
- Hara, K., Yano, T.-a., Suzuki, K., Hirayama, M., Hayashi, T., Kanno, R., Hara, M., 2017. Raman imaging analysis of local crystal structures in LiCoO<sub>2</sub> thin films calcined at different temperatures. *Anal. Sci.* 33, 853–858. <https://doi.org/10.2116/analsci.33.853>.
- Jo, M., Hong, Y.-S., Choo, J., Cho, J., 2009. Effect of LiCoO<sub>2</sub> cathode nanoparticle size on high rate performance for Li-ion batteries. *J. Electrochem. Soc.* 156, A430. <https://doi.org/10.1149/1.3111031>.
- Kim, J., Fulmer, P., Manthiram, A., 1999. Synthesis of LiCoO<sub>2</sub> cathodes by an oxidation reaction in solution and their electrochemical properties. *Mater. Res. Bull.* 34, 571–579. [https://doi.org/10.1016/S0025-5408\(99\)00049-5](https://doi.org/10.1016/S0025-5408(99)00049-5).
- Lala, S., Montoro, L., Rosolen, J., 2003. LiCoO<sub>2</sub> sub-microns particles obtained from micro-precipitation in molten stearic acid. *J. Power Sources* 124, 118–123. [https://doi.org/10.1016/S0378-7733\(03\)00615-3](https://doi.org/10.1016/S0378-7733(03)00615-3).
- Le Van-Jodin, L., Rouchon, D., Le, V.H., Chevalier, L., Brun, J., Secouard, C., 2019. Ex situ and operando study of LiCoO<sub>2</sub> thin films by Raman spectroscopy: thermal and electrochemical properties. *J. Raman Spectrosc.* 50, 1594–1601. <https://doi.org/10.1002/jrs.5669>.
- Lee, T., Cho, K., Oh, J., Shin, D., 2008. Electrochemical characteristics of LiCoO<sub>2</sub> nanopowder synthesized via aerosol flame deposition (AFD). *J. Phys. Chem. Solid.* 69, 1242–1245. <https://doi.org/10.1016/j.jpcs.2007.10.086>.
- Lin, F., Liu, Y., Yu, X., Cheng, L., Singer, A., Shpyrko, O.G., Xin, H.L., Tamura, N., Tian, C., Weng, T.-C., 2017. Synchrotron X-ray analytical techniques for studying materials electrochemistry in rechargeable batteries. *Chem. Rev.* 117, 13123–13186. <https://doi.org/10.1021/acs.chemrev.7b00007>.
- Matsuda, Y., Kuwata, N., Okawa, T., Dorai, A., Kamishima, O., Kawamura, J., 2019. In situ Raman spectroscopy of LiCoO<sub>2</sub> cathode in Li/Li<sub>3</sub>PO<sub>4</sub>/LiCoO<sub>2</sub> all-solid-state thin-film lithium battery. *Solid State Ionics* 335, 7–14. <https://doi.org/10.1016/j.ssi.2019.02.010>.
- Mizushima, K., Jones, P., Wiseman, P., Goodenough, J.B., 1980. Li<sub>x</sub>CoO<sub>2</sub> (0 < x < 1): a new cathode material for batteries of high energy density. *Mater. Res. Bull.* 15, 783–789. [https://doi.org/10.1016/0025-5408\(80\)90012-4](https://doi.org/10.1016/0025-5408(80)90012-4).
- Nishi, Y., 2001. Lithium ion secondary batteries; past 10 years and the future. *J. Power Sources* 100, 101–106. [https://doi.org/10.1016/S0378-7733\(01\)00887-4](https://doi.org/10.1016/S0378-7733(01)00887-4).
- Patridge, C.J., Love, C.T., Swider-Lyons, K.E., Twigg, M.E., Ramaker, D.E., 2013. In-situ X-ray absorption spectroscopy analysis of capacity fade in nanoscale-LiCoO<sub>2</sub>. *J. Solid State Chem.* 203, 134–144. <https://doi.org/10.1016/j.jssc.2013.04.008>.
- Rana, J., Kloepsch, R., Li, J., Scherb, T., Schumacher, G., Winter, M., Banhart, J., 2014. On the structural integrity and electrochemical activity of a 0.5 Li<sub>2</sub> MnO<sub>3</sub> 0.5 LiCoO<sub>2</sub> cathode material for lithium-ion batteries. *J. Mater. Chem.* 2, 9099–9110. <https://doi.org/10.1039/C4TA01161A>.
- Ravel, B., Newville, M., 2005. ATHENA, artemis, hephaestus: data analysis for X-ray absorption spectroscopy using IFEFFIT. *J. Synchrotron Radiat.* 12, 537–541. <https://doi.org/10.1107/S0909049505012719>.
- Shen, S., Yao, C., Chen, J., Chiou, Y., 1997. Influence of the LiCoO<sub>2</sub> particle size on the performance of lithium-ion batteries. *J. Power Sources* 68, 533–535. [https://doi.org/10.1016/S0378-7733\(97\)02623-2](https://doi.org/10.1016/S0378-7733(97)02623-2).
- Sun, Y.-K., 1999. Cycling behaviour of LiCoO<sub>2</sub> cathode materials prepared by PAA-assisted sol-gel method for rechargeable lithium batteries. *J. Power Sources* 83, 223–226. [https://doi.org/10.1016/S0378-7733\(99\)00289-3](https://doi.org/10.1016/S0378-7733(99)00289-3).
- Tang, W., Kanoh, H., Ooi, K., 1998. Preparation of lithium cobalt oxide by LiCl flux method for lithium rechargeable batteries. *Electrochem. Solid State Lett.* 1, 145. <https://doi.org/10.1149/1.1390665>.
- Wang, Y., Liu, B., Li, Q., Cartmell, S., Ferrara, S., Deng, Z.D., Xiao, J., 2015. Lithium and lithium ion batteries for applications in microelectronic devices: a review. *J. Power Sources* 286, 330–345. <https://doi.org/10.1016/j.jpowsour.2015.03.164>.



## CURRICULUM VITAE

**Name:** Awadol Khejonrak

**Gender:** Male

**Nationality:** Thai

**Date of Birth:** 4 July 1993

**Email:** awadol.sut@gmail.com

### **Educations:**

- 2006-2012: Princess Chulabhorn's college Mukdahan school, Mukdahan, Thailand (Science High school)
- 2012-2016: Department of Physics, Science, KhonKaen University, KhonKaen, Thailand (Bachelor of Science)
- 2016-2021: School of Physics, Science, Suranaree University of technology, Nakhon Ratchasima, Thailand (Doctor of philosophy in Physics)



มหาวิทยาลัยเทคโนโลยีสุรนารี